UNLV | **University Libraries**
University of Nevada, Las Vegas

UNLV Theses, Dissertations, Professional Papers, and Capstones

May 2018

Detector Arrays for Nuclear Security and Safeguards Applications

Jessica Hartman
Hartman1Jess@gmail.com

DETECTOR ARRAYS FOR NUCLEAR SECURITY AND SAFEGUARDS APPLICATIONS

By

Jessica Hartman

Bachelor of Science – Mechanical Engineering
University of Nevada, Las Vegas
2012

Master of Science – Materials and Nuclear Engineering
University of Nevada, Las Vegas
2014

A dissertation submitted in partial fulfillment
of the requirements for the

Doctor of Philosophy – Mechanical Engineering

Department of Mechanical Engineering
Howard R. Hughes College of Engineering
The Graduate College

University of Nevada, Las Vegas
May 2018

Dissertation Approval

The Graduate College
The University of Nevada, Las Vegas

May 1, 2018

This dissertation prepared by

Jessica Hartman

entitled

Detector Arrays for Nuclear Security and Safeguards Applications

is approved in partial fulfillment of the requirements for the degree of

Doctor of Philosophy – Mechanical Engineering
Department of Mechanical Engineering

Alexander Barzilov, Ph.D.   Kathryn Hausbeck Korgan, Ph.D.
Examination Committee Chair   *Graduate College Interim Dean*

William Culbreth, Ph.D.
Examination Committee Member

Yitung Chen, Ph.D.
Examination Committee Member

Thomas Hartmann, Ph.D.
Examination Committee Member

Steen Madsen, Ph.D.
Graduate College Faculty Representative

ABSTRACT

DETECTOR ARRAYS FOR NUCLEAR SECURITY AND SAFEGUARDS APPLICATIONS

By

Jessica Hartman

Dr. Alexander Barzilov, Examination Committee Chair

Associate Professor of Mechanical Engineering

University of Nevada, Las Vegas

Over the last two decades it has become increasingly apparent that there is a need for new technologies capable of reliable and efficient fast neutron detection. As national and international stockpiles of ^{3}He continue to dwindle, the need to find a new gold standard of neutron detection becomes more critical. Moreover, neutrons are generated typically in the MeV energy range. The use of ^{3}He detectors for fast neutron measurements requires the use of moderators. Detector arrays capable of fast neutron detection are one solution to this problem. To this end, the focus of this work was the study of detector arrays for fast neutron detection applications, particularly as they relate to nuclear security and safeguards.

The detector array study was carried out in three stages. The first stage focused on the identification and comparison of potential scintillator mediums for use in fast neutron detection. EJ-299-33A, CLLB, and CLYC were selected for initial modelling. Each material was identified through exhaustive literature surveys to be capable neutron/photon pulse shape discrimination and selected primarily for this feature. Single cell models of homogeneous compositions were developed using each of these materials. Simulations were done using the MCNP6 code. Additional simulations were performed for heterogeneous models consisting of a cell of the plastic scintillator EJ-299-33A filled with several layers of crystalline scintillator material. The efficiency of these heterogeneous samples was considered in relation to the size of the crystal components used.

The second stage focused on simulation and investigation of detector arrays, their susceptibility to cross-talk between detector pixels and their potential in radiation imaging applications. The occurrence of cross-talk was studied for three cases 1) each pixel was unshielded and in direct contact with its neighbors, 2) lead shielding was placed between the pixels of the detector array, 3) pixels were staggered across two rows to avoid direct contact between neighbors. Imaging simulations were carried out to study the feasibility of using 2.5-MeV and 14-MeV neutron sources to identify targets or hidden materials without physically inspecting the contents of a container or object under scrutiny.

The final phase of this work focused on experimental testing of the pulse shape discrimination capabilities of an EJ-299-33A plastic scintillator sample. Emphasis was placed on the material's suitability for fast neutron detection particularly when employed in mixed neutron/photon fluxes. Measurements were done with photon sources and a PuBe source. Measurement data was analyzed to determine the figure of merit for the scintillator and identify its suitability for pulse shape discrimination applications.

ACKNOWLEDGEMENTS

This dissertation would have been impossible without the support and advice of my advisor and committee chair, Dr. Alexander Barzilov. I would also like to thank my committee members, Dr. William Culbreth, Dr. Yitung Chen, Dr. Thomas Hartmann, and Dr. Steen Madsen for taking the time to review my documents, and offer their suggestions and critiques. Your knowledge and experience made each of you invaluable both as instructors and committee members during my PhD program.

Julie Longo and Joan Conway also deserve a shout out for their willingness to provide advice and help. Julie, you are a strong-willed force to be reckoned with. Your experience and expertise in technical writing and editing has been invaluable even if I still occasionally cringe at the sound of your voice while working on my documents. I'm grateful for all the advice and little tips you've shared while at UNLV. Joan, you may be the administrative assistant for the Mechanical Engineering Department, but we all know who really runs the show! Without you I would probably still be missing more paperwork than I even knew I needed. You've always been able to keep me straight on paperwork, deadlines, and requirements.

I also need to thank my lab mates for reminding me that it is ok to take a break and celebrate the little accomplishments. Finally, a huge thank-you to Dale Karas for his invaluable help with Matlab!

<u>DEDICATION</u>

For my parents, sister, and brother.

You remind me to find the light.

TABLE OF CONTENTS

LIST OF TABLES

LIST OF FIGURES

LIST OF ACRONYMS

ASIC   Application-Specific Integrated Circuit

Ce-STE   Cerium Self-Trapped Excitation

CLLB $Cs_2LiLaBr_6$:Ce

CLYC Cs_2LiYCl_6:Ce

DD   Deuterium-Deuterium

DT   Deuterium-Tritium

FNA   Fast Neutron Analysis

FOM   Figure of Merit

FWHM   Full Width Half Maximum

IT   Total Integration Time

MCP   Micro Channel Plate

PFNA   Pulsed Fast Neutron Analysis

PIT   Partial Integration Time

PMT   Photomultiplier Tube

PSD   Pulse Shape Discrimination

TNA   Thermal Neutron Analysis

TR   Transmission Ratio

CHAPTER 1 – INTRODUCTION

Statement of Need for Fast Neutron Arrays for Imaging

The 9/11 attacks forced a re-evaluation of the national security measures employed against potential terrorist activities. Renewed efforts were made to develop detection technologies capable of locating and identifying nuclear material being moved outside of regulatory control. In 2004, the U.S. government commissioned a study of the potential impact of a nuclear terrorist attack on a continental shipping port. The result was a study focused on the detonation of a 10-kiloton nuclear bomb at the Port of Long Beach in California. The result was the complete destruction of both the Port of Long Beach and the Port of Los Angeles, including the ships docked in both ports. Projections estimated initial losses of 60,000 lives and more than $1 trillion dollars between economic and property losses, due to the initial blast. An additional 150,000 people were expected to suffer exposure to harmful radiation levels as a result of the subsequent fallout [1].

In 2007, the United States passed Public Law No 110-53 to combat the potential risk of an event like the one detailed in the RAND report. It mandated that by 2012, 100% of all aviation and maritime cargo be scanned prior to its departure from foreign ports [2]. Despite the implementation of cargo scanning systems at shipping ports along the Pacific, Atlantic, and Gulf Coasts, the deadline has been extended three times, most recently until 2018 [3]. Between 5% [3] and 6% [4] of all incoming maritime containers are flagged as "high-risk" and subjected to additional scanning [3] and possible physical inspection by security personnel [4]. Most containers are pre-screened and flagged using the country of origin, shipper's history, and cargo manifest details rather than imaging data.

General purpose containers have a range of options available [5], but the average maritime shipping container is a standard 40' length with doors at one or both ends [6]. Additional doors can be added on one or both sides for ease of loading/unloading the cargo. Built from steel with interior dimensions of 12 m, 2.35 m, and 2.37 m and a volume of 67 m3 [7], a single container provides ample space for

transporting anything from agriculture products to vehicles and even chemical or nuclear materials. As of June, 2016, U.S. Customs and Border Protection (CBP) reported that only 29 of the 74 maritime ports accepting foreign cargo already had imaging equipment in use [3]. Additional data indicated that CBP processed an average of 80,000 standard shipping containers per day in 2016 [8] and roughly 29 million containers over the course of the year. Of these, roughly 12 million entered the U.S. via maritime ports, and fewer than 1 million were flagged and subjected to additional imaging processes or physical inspection. Similar problems exist for cargo shipped via road or rail.

Part of the problem in establishing a 100% scan rate stems from the imaging systems themselves [6]. Designed for the purpose of identifying nuclear material being transported outside of regulatory control, current detection systems are expensive. When China purchased radiation detectors for the Beijing Olympics in 2008, the average cost per detector was $27,000 [9]. Other companies like Ludlum Measurements, Inc. offer personnel portal monitors such as the Model 52 [10] for $12,543 [11] and the Model 53 [12] for $52,995 [11]. The most concerning flaw though is their high rate of false-positives which result in wasted resources for security personnel and costly time delays for shippers.

The development of a reliable imaging system is critical to the continued security of the U.S. and one viable solution is the use of detector arrays capable of fast neutron measurements. Fast neutrons represent a radiation which can deeply penetrate materials found in cargo shipments. Neutrons interact differently with nuclei than photons providing additional data for better identification of materials. Moreover, neutrons can initiate fission reactions in nuclear materials thus enabling their identification through detection of photons and neutrons emitted in fission events. If implemented fast neutron array based systems would offer an improvement on current dual-energy photon systems, and could be used with novel detector materials making them quicker and easier to mass produce while reducing the cost and fragility of the overall system.

Detector Arrays

Developed in the 1980's, radiation detector arrays are a standard feature of modern imaging systems. Although the composition and design of the array can differ between products, the basic concept is the same. Detector arrays have two key components [13], multiple detector elements which comprise the array and an attached electric circuit which processes data from the detector elements.

In scintillation detectors, radiation enters the detector as a particle or electromagnetic wave and interacts with the detector's medium. The interaction between the radiation and atoms can result in the loss of some or all of an incident particle's or wave's energy. This energy loss produces a flash of scintillation light which is registered using the attached optical readout and electronic components, and translated into an electronic signal waveform that can be recorded and analyzed.

Detector arrays are currently employed for a variety of applications across several fields such as medicine, industry, and security. The nuclear security and safeguards applications are of particular interest, and there is room for improvement of the systems already deployed. Current technology makes use of detector arrays in x-ray, dual-energy photon radiography, neutron imaging, and neutron/photon radiography techniques. While accelerator research and development has made it easier to produce safe and reliable radiation sources, the detector arrays could be improved by using materials which are inherently capable of discriminating between different radiation types.

Radiography Methods

Radiography methods are based on radiation attenuation. As radiation travels through a given material there is a chance that it will do one of three things. It could pass straight through the material without interacting with it. It could enter the material and suffer one or more collisions with it before passing out of the material. It could enter the material and after suffering one or more collisions with the material present it could lose enough energy that it is absorbed by the material and doesn't exit.

The chance that radiation will follow one of these paths is affected by several factors including the type of incident radiation (neutron, photon, alpha, etc.), the energy of the radiation as it enters the medium, and the material composition of the medium (its density, thickness, nuclear cross-section, etc.). Standard attenuation equations are used to determine the specific radiation transmitted through a specified material of a given thickness.

Dual-energy photon radiography methods are commercially available, and employed at various ports and border crossings within the United States. This technology functions by placing the target object between a radiation source, such as an accelerator, and a detector array or screen. When the accelerator is turned on, radiation of a given type and energy is emitted from the source and passes through the target volume, either being "trapped" in the material or passing through it and into the detector medium. Collisions in the detector medium are "seen" when particles or radiation interact and cause a detectable flash of light which is converted into a signal for online or post-processing analysis.

The purpose of this research is to study the potential of fast neutron detectors for security and safeguards applications. By employing scintillator materials in the detector array it is possible to produce a detection system capable of working only with a neutron source. Many modern scintillators are manufactured with inherent pulse shape discrimination (PSD) capabilities and data can be post-processed to store only those measurements resulting from incident neutrons, while discarding photon-related measurements. Alternatively, PSD-capable fast neutron detector arrays can also be used in dual photon and fast neutron imaging systems to provide more accurate information about the targets being imaged.

The inherent difference between neutron and photon interactions is reflected in the equations used to determine their transmission through materials. As electromagnetic waves, photons are more likely to interact with high-Z materials due to the greater number of electrons in their atomic shells. As a result, the attenuation equation for photons (Eqn. 1) is dependent on the linear attenuation coefficient (μ) and the thickness (t) of the medium:

$$\frac{I}{I_0} = e^{-(\mu t)} \qquad \text{(Equation 1)}$$

As uncharged particles, neutrons largely ignore the electron cloud, making them more likely to interact with elements and atoms that have a volume filled primarily by the nucleus rather than the electron cloud. Due to this, they are more sensitive to low-Z materials and materials with a large macroscopic cross-section. This is reflected in the neutron attenuation equation (Eqn. 2), which uses the total macroscopic cross-section (Σ_{tot}) of the atoms in the medium in place of the linear attenuation coefficient and the medium thickness (t).

$$\frac{I}{I_0} = e^{-(\Sigma_{tot} t)} \qquad \text{(Equation 2)}$$

Using these differences in transmission for neutrons and photons, it is possible to calculate a set of transmission ratios (TRs) for specific materials. Fig. 1, shows the comparison of TRs for selected low-Z (polyethylene, water, aluminum), and high-Z (iron, lead) materials. These values were determined for three source configurations: 1) 0.2-MeV photons and 0.1-MeV neutrons, 2) 0.2-MeV photons and 2.5-MeV neutrons, and 3) 3-MeV photons and 6-MeV photons. Comparison of the results showed a considerable benefit to using neutrons for this application. Standard radiography imaging systems use 3-MeV and 6-MeV photon sources, but these energies and radiation offer only a limited range of TR values even when considering materials with vastly different nuclear and material properties such as lead and polyethylene. Using the 3-MeV/6-MeV system, the TR values for lead and polyethylene were 0.964 and 1.466 respectively. In contrast, using a photon/neutron system with low energies (0.2-MeV/0.1-MeV) showed considerably more variation the TR values for these materials. The TR value was 7.273 for lead and 0.109 for polyethylene. Similarly, using a 0.2-MeV/2.5-MeV photon/neutron system produced TR values of 9.538 and 0.487 for lead and polyethylene respectively.
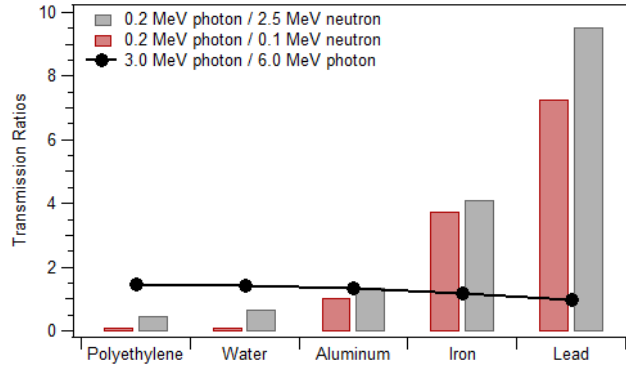
Fig. 1. Transmission ratio comparison for different dual-radiation imaging

CHAPTER 2 – LITERATURE REVIEW

The need for fast neutron detection is not novel. With the discovery of the neutron in 1932 [14], the question of how to achieve neutron detection has fascinated researchers. The realization of an organic scintillation detector in 1947 [15] encouraged further research as scientists began looking for a reliable, and efficient way to detect these uncharged particles [16]. The first fast neutron detector, a ZnS Lucite sandwich, was reported only 2 years later in 1949 [17], while the second was a mixture of ZnS and Lucite powders published in 1952 [18]. Fast neutron detection has remained a topic of interest, but it wasn't until the 1990s and early 2000s that fast neutron detector research again took center stage due to dwindling ^{3}He supplies and increased terrorist activities [19, 21].

Several neutron detection based techniques have been developed and demonstrated to be particularly effective for national security applications like explosive detection and identification [22]. There are two key issues which make fast neutron detection a challenge. First, neutrons lack a charge which makes direct detection of these particles difficult [16]. Second, the isolation of neutron response from measurements due to background or secondary particle creation requires additional data treatments.

Neutron Detection Methods

The first challenge to fast neutron detection is that these particles are not directly ionizing particles. Historically this has made the development of fast neutron detectors methods more difficult than charged particle detectors [23]. Instead of focusing on detecting the neutrons themselves, early detectors were designed to detect the charged products resulting from neutron interactions with detection mediums [23-24]. Depending on the energy of the incident neutron (thermal or fast), there are a variety of techniques which can be used in analysis of neutron detection. Over the last 20 years, there have been several reviews and summaries published neutron-based detection techniques [19-22, 25-30].

Neutron detection technologies are used in active and passive assays techniques. Neutron-based interrogation techniques are broken into two groups depending on the system being used [30]. Passive

interrogation techniques are non-invasive, using devices or system components that never directly interact with the subject [30]. The concept is similar to passing a Geiger counter near an object, without directly touching or further examination, in order to determine if radiation is present. In general these systems are limited in their reliability and can be slow to produce results. Active interrogation systems do not suffer these limitations and are considered the better and more dependable of the two [27, 29]. Neutron-based systems in this category generally work by aiming neutrons at an object, where they interact directly with it in order to quickly produce more information than passive techniques or systems can [30].

The technology already exists for a wide range of neutron-based active interrogation techniques as reviewed by Gozani [21, 29], Whetstone [30], and Hussein [27]. Among these, thermal neutron analysis (TNA), fast neutron analysis (FNA), and pulsed fast neutron analysis (PFNA) are frequently employed for security and imaging applications. TNA is one of the oldest techniques, first commercially deployed at the John F. Kennedy International Airport in 1990 [31]. This technique relies on the use of radioactive sources like ^{252}Cf or accelerators to produce fast neutrons which must then be moderated to reach thermal energies (0.025 eV) [27-28, 30]. The moderated neutrons are aimed at a target object, and TNA has proven particularly effective in identifying nitrogen and hydrogen both of which are present in explosive materials [28, 30]. TNA suffers two significant drawbacks though as fails to properly detect carbon and oxygen which are equally important in accurately identifying explosives [30]. Due to the use of accelerator sources, this technique can also suffer from neutron leakage during moderation making it less than ideal [27]. FNA techniques improve upon TNA techniques though their ability to detect nitrogen, carbon, and oxygen by using un-moderated fast neutron sources [28, 30]. FNA systems are also ideally suited to portable device applications since the moderator component required by standard TNA systems is removed [27, 30]. By relying on fast neutron interactions via inelastic scattering with the target object, FNA becomes particularly susceptible to high background readings as scattered neutrons and their products affect detector readings [30]. It has also been reported to have poor imaging capabilities when tested with larger objects [28]. PFNA corrects the drawbacks of both the TNA and FNA systems by employing a pulsed source [27-30] which delivers bursts of neutrons from the accelerator source to a

target. This modification allows for the detection and identification of more elements (H, C, N, O, Cl, Si, and K) while reducing the neutron background below the levels present in TNA and FNA systems [30].

Current Neutron Detectors

With national and worldwide stockpiles of ^{3}He continuing to dwindle, the need for a fast neutron detector capable of replacing current proportional counter systems without sacrificing their reliability or efficiency becomes critical [16]. There are a wide range of detectors capable of fast neutron detection, but this review focuses on Microchannel Plate Detectors (MCPs) and scintillator detectors, the latter of which can be further separated into homogeneous, heterogeneous, composite, phoswich, and gel categories. These detectors have gained popularity within the last decade, and continue to offer promising solutions to the ^{3}He supply problem. Other detector types have been proposed and developed, but most of these lack the capability for fast neutron detection, opting instead to focus on photon or thermal neutron detection.

Detectors

Over the last two decades, significant research has been focused on the potential of MCPs in radiation detection. Claims have been made that MCPs were first conceived in the 1950s [32-33], but the earliest publication available on the topic came from Bendix Research Laboratories in 1962 [34-35]. MCP research focused primarily on development of these systems for electron and photon measurements [36], but in the last two decades, interest has grown in developing MCP systems capable of UV, alpha, cold neutron, and thermal neutron measurements [32, 37]. As the threat of dwindling ^{3}He supplies continues to rise, there have also been several recent attempts at using MCPs for fast neutron detection [38]. By exploiting doping techniques, using ^{10}B or Gd, it is possible to manufacture MCPs with a sensitivity levels and detection efficiencies similar to standard ^{3}He tubes and proportional counters [39].

Timepix detectors are an adaptation of the MCP family, which apply an application-specific integrated circuit called an (ASIC) to the MCP for signal processing. Details about these detectors were first published in 2007 [40-41], and in the last 10 years they have been the subject of much interest, and have

been shown to have acceptable background rates, imaging and timing properties when developed for Cherenkov light detection [42]. Improvements to the centroiding algorithms employed by these detectors have also been documented, allowing for improved spatial resolution when subjected to high count rates [43]. These detectors have also proven useful for neutron detection applications [32, 39, 44-47].

Scintillator detectors are typically defined as a photomultiplier tube (PMT) coupled with a scintillator cell [48]. When scintillation events occur as the result of nuclear reactions and interactions taking place in the scintillator cells, the PMT amplifies these signals produced by the events and passes the data to other attached electronics. Scintillation counting was used as early as 1908 [49], but the first publication wasn't until 1929, when Chariton and Lea performed their alpha-counting experiments in environments with significant β and photon radiation background [49-51]. Scintillator materials have since been the center of considerable research efforts, especially with the advent of the PMT which was a catalyst for numerous scintillator related innovations in the 1950's [52]. More recently, research and development has focused on liquid, plastic, and crystalline materials [53], with considerable attention paid to their application in source detection and identification tasks [54-57].

Scintillator materials can be defined either as organic or inorganic depending on the presence of carbon in their chemical structure [48]. Inorganics lack carbon atoms, and are typically manufactured as solid crystals. These scintillators tend to suffer reduced response times, while boasting greater light output making them an ideal choice for photon applications [48, 55, 58]. Only a dozen inorganic scintillators were commercially available in 1992 [59], but a 1997 publication discussed the scintillation capabilities over 400 inorganic scintillator materials [59-60]. Inorganic scintillators are still a source of interest as evidenced a 2012 report released by Sandia National Lab which identified and studied 640 different elpasolite scintillator materials [61]. Two inorganic crystal scintillators, CLLB ($Cs_2LiLaBr_6$:Ce) and CLYC (Cs_2LiYCl_6:Ce), have seen renewed interest from researchers. Both have been the subject of studies focusing on their spectroscopy and PSD capabilities which proved their effectiveness in differentiating between incident photon and neutron signals [62-63]. Unfortunately production of both

crystals remains an expensive, lengthy, and difficult process, especially when large crystals or multiple crystals with uniform properties are required.

Organic scintillators have a chemical structure that includes carbon, and are available in a wide range of materials, including crystals, liquids, plastics, and even gels. They also tend to possess a higher hydrogen content than their inorganic counterparts, making them particularly suitable for fast neutron detection [48, 58]. Although the majority of crystal scintillators are considered inorganic, stilbene ($C_{14}H_{12}$) and anthracene ($C_{14}H_{10}$) are the textbook examples of organic crystals, and were frequently used in the early 1950s and 1960s. Their high resolution and sensitivity made them an ideal choice for neutron detection, but their fragility and high cost of production encourage the development of alternatives. Anthracene offered unparalleled scintillation efficiency, but the lack of reliable PSD properties made this material unfit for neutron measurements [48, 58]. Stilbene possessed a lower scintillation efficiency than anthracene, but it's inherent PSD properties made it possible to use in mixed radiation measurements, where signal separation was preferred or required [48, 58]. This crystal has remained a source of interest to researchers [16, 64], and boasts better scintillation properties when compared with current plastic (EJ-276) and liquid (EJ-309) options [65]. Despite recent advances in crystal growth [66], the monetary and time costs of crystal production, as well as their fragile nature are prohibitive to widespread use.

Liquid scintillators have been the standard in neutron detector systems and applications for many years. They require less time to produce, but remain fragile and costly due to the construction process [67]. Typical liquid scintillator designs make use of a metal cap filled with liquid scintillator and an inert gas bubble that acts as an expansion void. The metal cap is then sealed with a transparent glass plate which is fragile and subject to damage if dropped or roughly handled. Manufacturing processes and solvent impurities have also been shown to negatively affect detector consistency, with significant pulse height differences reported between liquid samples from the same batch [52]. These scintillators are also known to suffer extremely low flash points, below 26°C, although recent developments by ELJEN Technologies have produced scintillators with a significantly higher flash point of 144°C (Appendix A) [16]. The inherent PSD capabilities of liquid scintillator materials also make them ideal for neutron detection.

BC501A in particular has been employed in the EUROBALL scintillator array developed for neutron detection [68-69].

Unlike crystalline and liquid scintillators, plastics have the advantage of being robust, easier to machine into an infinite selection of shapes and sizes, and more cost effective to manufacture in large quantities [65, 70-71]. In 2014, nearly all commercially available plastic scintillators were based on formulas developed in the 1950's and 1960's and lacked PSD capabilities [71-72]. This changed with reports of the first PSD capable plastic scintillator in 2012 [73], EJ-299-33A soon became the first commercially available plastic scintillator known to have inherent PSD properties [65, 71, 74]. This material was capable of reasonable neutron/photon PSD, but only above a 0.5 MeV threshold, below this neutron and photon signatures became indiscernible [54]. Recent developments in plastic scintillator production and manufacturing have resulted in EJ-276 and EJ-276G replacing the original EJ-299-33A material as reported by the manufacturer on their specification sheet (Appendix A). This material shows improved PSD capabilities, particularly in lower energy ranges where EJ-299-33A had struggled. A survey of scintillator materials (Stilbene, EJ-309, and EJ-276) revealed that with the new EJ-276 version plastic scintillators had finally reached a point where their scintillation and PSD capabilities made them a viable replacement for current liquid scintillators [65]. Plastic scintillators continue to fascinate and offer limitless possibilities for detection applications, including use in fiber optic arrays [71, 75-77]. Although this technology is not yet commercially available, the design has been patented for x-ray imaging [75] and has potential in neutron measurements due to the PSD capabilities of the material.

Heterogeneous scintillator detectors offer a unique solution to the size and growth limitations of crystal scintillator detectors. Proposed in 1998, the idea to create a heterogeneous scintillator using ground up organic scintillator crystals or crystal grains was a novel one [71, 78-79]. These scintillators can be broken into two categories depending on the manufacturing process. Polycrystalline scintillators are created when the crystal grains are sintered together using a method called hot pressing [80]. Composite scintillators are created by inserting the crystal grains into an inert medium, usually a glue or polymer base [16, 24, 53, 71, 79-84].

By opting to use these heterogeneous scintillators instead of single crystals, the cost and difficulty of manufacturing can be reduced either by eliminating the growing phase or by using the crystal waste material frequently produced while treating fully grown crystals [80]. Another benefit of composite scintillators is their potential use in developing large-area detectors for array or imaging applications [80, 85]. In addition to nearly infinite size options, variation of the crystal grain sizes used allow for direct manipulation of the material properties and sensitivity to unique radiation signatures such as photon, alpha-particle, and neutron [80-81, 86-87].

Significant research has also been carried out on composite scintillators in the last decade, particularly those employing stilbene and p-terphenyl crystals, for the purpose of adapting and applying these detectors in fast neutron detection [24, 53, 79-82, 84]. Composite scintillators have also been successfully applied for simultaneous thermal and fast neutron measurements, showing discrimination between the two energy ranges even when measured against background photon radiation [71, 83]. The dimensions of these scintillators are driven by the efficiency required for neutron detection. Although they can be designed with a nearly infinite surface area, the scintillator thickness should be as small as possible to ensure high enough efficiency for use in neutron detection applications [16, 71].

The concept of a phosphor sandwich or "phoswich" detector was first published by D.H. Wilkinson in 1952 [88]. The design works by optically coupling different detector mediums, each with inherently unique time decay properties to a single PMT [48, 88-89]. By doing so, it is possible to take advantage of the unique scintillator properties to simplify PSD processing and separation of measurement data recorded with the detector. Wilkinson was primarily focused on applying this technology to photon spectroscopy with potential neutron detection applications [88].

Phoswich development has focused primarily on designs incorporating 2 or 3 selected scintillators or other detection mediums. Significant research has been done on the phoswich applications for identifying β-particles, alpha-particles, and photons using 2-scintillator [89-93], and 3-scintillator models [94-100], with radioxenon applications in particular benefiting from development of a phoswich well detector [101-108]. Additional work has been done to identify phoswich combinations capable of neutron detection,

with successes being reported for various combinations of plastic, liquid, and crystal scintillators. Combinations of NE213 and NE211 [109], and EJ-299-13 and EJ-399-06 [110-112] have all proven effective for high-altitude and extraterrestrial measurements of high energy neutrons (>100MeV), while NaI(Tl) and NE102A have been successfully tested in neutron fluxes between 100-MeV and 350-MeV [113]. Additional work has been published on the use of EJ-299-33A and a ^{6}Li-loaded glass cell for differentiation between photons, thermal neutrons, and fast neutrons [114].

The measurement and study of the neutron dose equivalents suffered by astronauts has been a focus of international study and co-operation, with Russia and USA carrying out joint experiments on Space Shuttle flights STS-57 [115], STS-60 [116], and STS-89 [117]. Data from STS-57 indicated that roughly half of the neutron dose equivalent suffered by astronauts is due to fast neutrons between 1-MeV and 15-MeV [115, 118]. Later experiments from flight STS-89 indicated that nearly 30% of total dose equivalent was due to fast neutrons in the range of 1-MeV to 10-MeV [117-118].

The greater risk of radiation exposure, and the need to accurately determine the neutron dose suffered by astronauts was the driving force behind the development of a new generation bubble detectors [118]. Bubble Technology Industries Inc. developed a visco-elastic scintillator material for neutron detection for use in the Canadian space program [119]. This gel scintillator holds great potential, with similar performance characteristics being reported when compared to commercially available liquid scintillators such as BC501A and NE213 [119-120]. Gels also have the added benefit of not being highly flammable unlike their liquid counterparts which have been labeled as fire hazards [120].

These scintillators have been incorporated into a hybrid superheated drop and bubble detector design, where droplets of superheated liquid are seeded in a visco-elastic material [118]. As the gel is exposed to incident neutrons, the particles strike the superheated droplets initiating bubble nucleation through the recoil particles. The affected gas bubble will grow, allowing for visual detection of irradiation. Since the gel captures the bubbles as they are formed, these detectors can be used multiple times as long as they are re-pressurized to force the bubbles back into the gel matrix [118, 121].

The Canadian High-Energy Neutron Spectrometry System (CHENSS) combines this gel scintillator with the phoswich concept to reduce measurement interference from the proton background generated by galactic cosmic rays [122]. In this system, the gel scintillator is surrounded completely by a shell of plastic scintillators which prevent the proton background from reaching the gel scintillator and registering incorrectly as neutron signatures [122].

Pulse Shape Discrimination (PSD)

Although the ability to isolate measured neutron responses from background photon responses can be complicated due their similar penetration ranges [18, 71], scintillator materials offer an inherent solution to this problem. Exploiting this property in the processing of measurement data allows signatures or spectra from specific particles/radiations to be isolated. As early as 1956, alpha-particles and photons were being distinguished using PSD [123]. Also referred to as pulse shape selection by F.D. Brooks, the unique PSD attribute of scintillator materials was being explored in 1958 for the purpose of isolating measured neutron and photon responses[124]. PSD techniques rely on an inherent property, whereby incident particles or radiation exhibit unique decay times determined by the incident particle as it interacts with a given scintillator material [15, 71, 123-125]. As incident particles interact with the atoms of a scintillator material, they produce flashes of light which can be measured and recorded by an attached PMT [59, 126]. The intensity and duration of each flash is translated into a waveform with characteristics dependent on the incident particle/radiation that created it.

Fig. 2 shows a comparison of neutron and photon waveforms recorded using the Igor Pro software with the Emorpho digitizer for data collection. Comparing the basic shape, it is obvious that photon induced signals exhibit sharper peaks with almost no tail. In contrast, neutron induced signals possess a wider peak and significantly longer tail. PSD techniques apply two variables to these waveforms for analysis and separation of measured data. The first is the Integration Time (IT), also referred to as the total integration time. This value represents the integral of the wave form, spanning the recorded time of the full signal from its initial occurrence (~0.025 µs in Fig. 2) until the cut-off (~0.475 µs in Fig. 2). The

second variable is the Partial Integration Time (PIT) which identifies a cut-off point dividing signals into "head" and "tail" portions (~0.125 µs in Fig. 2).
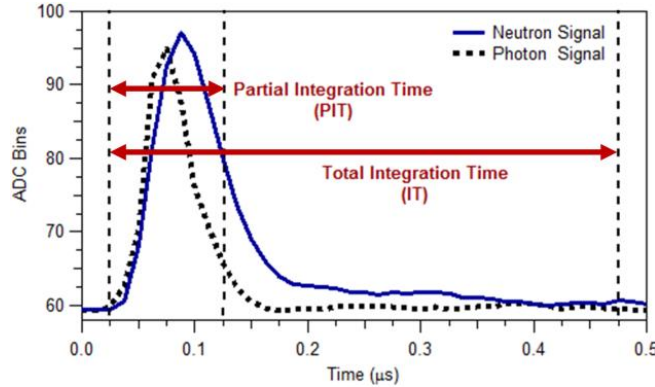
Fig. 2. Comparison of neutron and photon pulses for PSD technique

Both the PIT and IT values are user-defined and can be adjusted in the eMorpho digitizer to adjust the PSD process and optimize the separation of incident radiation measurements. Using both values, each signal can be identified as a neutron, photon, or other particle using the PID value. This value is calculated using the integral of each signal between its initialization (1.2 µs) and its PIT and IT values as shown in Eqn. 3, making the PID value the ratio of the signal's "tail" to its "head". When comparing photon and neutron responses, smaller PID values identify the signals caused by photons, while larger PID values identify those resulting from neutron interactions.

$$PID = \frac{\int_{IT} - \int_{PIT}}{\int_{PIT}} \qquad \text{(Equation 3)}$$

Passive and active assay techniques have been developed for nuclear security and safeguard applications. These techniques require development of advanced neutron detection technology. Significant research and development has also been done on the capability of MCPs and scintillator detectors for fast neutron detection. MCPs show great promise but can be complicated and costly to produce for detector array applications, especially when ASICs are integrated into the system. Scintillator detectors are simple in

comparison, available as plastics, crystals, liquids, and gels. Plastic scintillators enable design of detectors of various shapes and sizes, including multi-pixel arrays.

Neutron/photon PSD is a critical aspect of fast neutron detection due to the presence of photon signatures in measurements. Employing PSD techniques makes it possible to separate the signatures and focus on the neutron component of measurements for detection and identification tasks.

CHAPTER 3 – SCINTILLATOR FEASIBILITY STUDY

Homogeneous Scintillators

Although there are several ways to categorize neutrons based on their energies, fast neutrons are defined in this document as any neutron with energy of 0.5-MeV or more. The first objective in this work was to determine the feasibility of scintillator materials for use specifically in fast neutron detection. To achieve this, simulations were performed using version 6.1 of the Monte Carlo N-Particle Transport (MCNP6.1) code produced and maintained by Los Alamos National Laboratory [127-128]. This code provides an extensive set of particle tracking and tallying features based on the Monte Carlo technique. By applying user defined inputs, it can trace a wide range of nuclear particles (neutrons, electrons, alpha-particles, etc.) and electromagnetic waves (photons) as they are transported through a model, interacting with materials, depositing/gaining energy, and potentially escaping the geometrical boundary of the model.

MCNP6.1 was used to model the geometry in Fig. 3 and calculate the efficiencies for different scintillator configurations. It consisted of a 5.08 cm by 5.08 cm cube of scintillator material placed 1 cm from a mono-energetic, neutron beam. The scintillator cell and the beam were aligned so that the beam was focused on the center of the square face of the scintillator
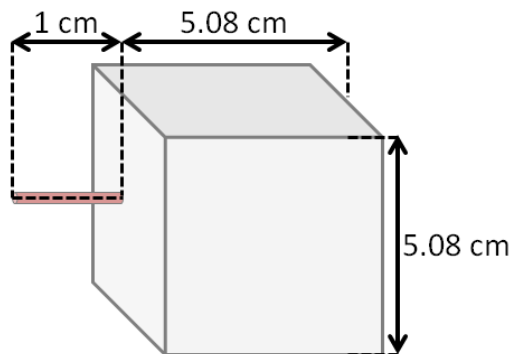
Fig. 3. Simulation geometry for scintillator efficiency modeling

Several versions of this model were examined with consideration given to varying the scintillator material and the neutron energies for each simulation. Neutron energies were used between 1-MeV and 14-MeV using 0.5-MeV increments. The F8 tally was employed to track particle interactions within the scintillator material resulting from incident neutrons. Several F8 tallies were included in each simulation to identify the measurement contributions resulting from unique radiations and particles including photons, protons, deuterons, tritons, and alpha-particles. F4 tallies were employed to identify the average surface flux of detector cells as well as their reaction rates and efficiencies.

The plastic scintillator, EJ-299-33A, is a transparent material produced by ELJEN Technologies. Composed of hydrogen and carbon with a proprietary blend of additives and wavelength shifters, this material offers a durable, lightweight alternative to standard detectors. Since its commercial release in 2012, it has been the subject of considerable research and development, leading to the creation of EJ-276 and EJ-276G. Reported by ELJEN as replacements for EJ-299-33A, the basic material properties of these two materials are similar to those of the EJ-299-33A. These properties are collected in Table 1 for comparison, and are taken from the material data sheets provided by ELJEN Technologies (copies of the material sheets are included in Appendix A). Due to this similarity, and the availability of EJ-299-33A for experimental verification, the material card was built using the specified hydrogen and carbon contents for EJ-299-33A.

Table 1 – Plastic Scintillator Properties from ELJEN Technologies (Appendix A)

	EJ-299-33A	EJ-276	EJ-276G
Max Emission Wavelength	420 nm	425 nm	490 nm
Light Output	56%	56%	52%
Material Density	1.08 g/cc	1.096 g/cc	1.096 g/cc
No. H atoms per cc	5.13×10^{22}	4.53×10^{22}	4.53×10^{22}
No. C atoms per cc	4.86×10^{22}	4.89×10^{22}	4.89×10^{22}
Scintillation Efficiency	8,600 γ /1 MeV e$^-$	8,600 γ /1 MeV e$^-$	8,000 γ /1 MeV e$^-$

Several combinations of cell dimensions were studied by varying the width, height, and depth. Cell width and height were defined as the horizontal and vertical dimensions of the surface perpendicular to the neutron beam; depth was defined as how far the scintillator cell extended from this surface (Fig. 4).
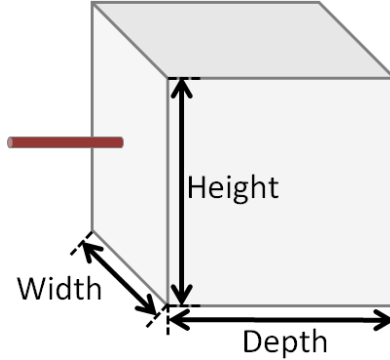
Fig. 4. Scintillator cell dimensions

Table 2 shows the breakdown of simulation versions according to the scintillator cell dimensions which were used. It was decided to maintain the square shape of the scintillator surface facing the source, so the length and width remained equal to each other in each simulation. Surface areas of 1 cm by 1 cm, 2.54 cm by 2.54 cm, and 5.08 cm by 5.08 cm were selected, while cell depth was varied between 1.50 cm, 2.54 cm, 5.08 cm, and 10 cm. The incident energy of source neutrons was also varied between simulations; each combination of cell dimensions was processed for 1-MeV, 2.5-MeV, 6-MeV, and 14-MeV.

Table 2 – Scintillator Cell Dimensions

Cell Width	Cell Height	Cell Depth
		1.50 cm
		2.54 cm
1 cm	1 cm	5.08 cm
		10.00 cm
		1.50 cm
		2.54 cm
2.54 cm	2.54 cm	5.08 cm
		10.00 cm
		1.50 cm
		2.54 cm
5.08 cm	5.08 cm	5.08 cm
		10.00 cm

Efficiency of the plastic scintillator EJ-299-33A was determined for each of the geometry combinations listed in Table 2 using MCNP6. F4 tally cards were modified to track the potential occurrence of (n,γ), (n,p), (n,d), (n,t), and (n,α) reactions by including SD and FM cards which changed the tally from an

average flux tally to a reaction rate tally. Figs. 5a and 5b show the results of these simulations for neutron source energies of 2.5-MeV and 14-MeV respectively. Comparison of the reaction rates for the different surface area and depth combinations indicated that while a 10-cm depth would show some improvement in reaction rates and subsequently the detector efficiency, it was not sufficient enough to warrant the increased cost and volume of the detector. The exception to this was the data set for the 2.5-MeV neutron source, where reaction rates for the 5.08 cm by 5.08 cm size scintillator were several times larger than the values for the same scintillator sample with smaller surface areas and cell depths of 5.08 cm and 10 cm.
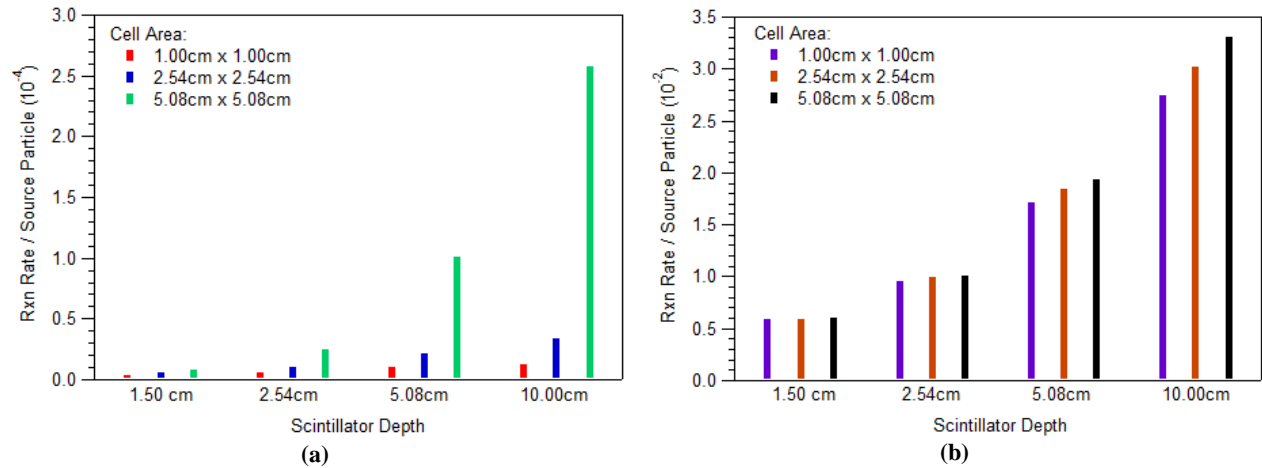
Fig. 5. Reaction rates of EJ-299-33A to incident neutrons of (a) 2.5-MeV and (b) 14-MeV

This study focused on comparison of the efficiency of three scintillator materials. Selection of the EJ-299-33A, CLYC-6, CLYC-7, and CLLB scintillators was based on commercial availability of the scintillators and data of their inherent PSD capabilities [54, 62-63]. Studies of homogenous samples of these plastic and crystalline scintillators were completed, although only the results for plastic are presented here. EJ-299-33A was found to be ideal for fast neutron detection measurement due to its short decay time (~50 ns), inherent PSD capabilities and durability. In comparison, crystal scintillators exhibit slower response times, increased fragility, and can be extremely costly to produce. A brief comparison of selected properties for CLLB, CLYC-6, and CLYC-7 scintillators is provided in Table 3. Decay times are shown for a neutron component, such as a slow cerium self-trapped excitation (Ce-STE) in CLYC-6 and CLYC-

7. It is worth noting that these crystal scintillators are capable of photon spectroscopy and exhibit significantly higher scintillation efficiencies when compared to EJ-299-33A (Table 2).

Table 3 – Crystal Scintillator Properties

	CLYC-6	CLYC-7	CLLB
Neutron Detection	Thermal	Fast	Thermal
PSD Capable	Yes	Yes	Yes
Photon Spectroscopy Capable	Yes	Yes	Yes
Decay Time (neutron component)	1,000 ns	1,000 ns	$\geq$ 270 ns
Scintillation Efficiency (γ/1 MeV)	20,000	20,000	60,000
Energy Resolution (@ 662 keV)	4.8%	4.5%	2.9%-3.0%

Although photon spectroscopy is not critical to fast neutron detector array development, it does have applications in dual radiation radiography where detection of both fast neutrons and photons is needed. Plastic scintillators are not capable of photon spectroscopy, and by incorporating both plastic and crystal materials into a single scintillator cell (heterogeneous scintillators) it is possible to exploit the different scintillation properties in order to analyze gamma-ray spectrum for a given measurement in addition to fast neutron detection.

Heterogeneous Scintillators

The potential of heterogeneous scintillator combinations was studied for simulations which mixed crystal scintillator shards into a plastic scintillator matrix. Fig. 6 shows an example of the model for one of these simulations. In this case, an isotropic point neutron source was positioned 20 cm from the circular face of a cylindrical scintillator cell. Instead of making this cell a solid body like the homogenous model, it was broken into an encompassing body of one scintillator (shown in grey), and several layers of spheres defined as a different scintillator material (shown in purple). For this set of simulations, the cylinder was defined as the plastic scintillator EJ-299-33A, and the purple spheres were modeled through several iterations as the crystal scintillators CLLB, CLYC-6, and CLYC-7. Incident particle counts and response functions were tallied within the plastic scintillator and each of the crystalline beads for comparison.
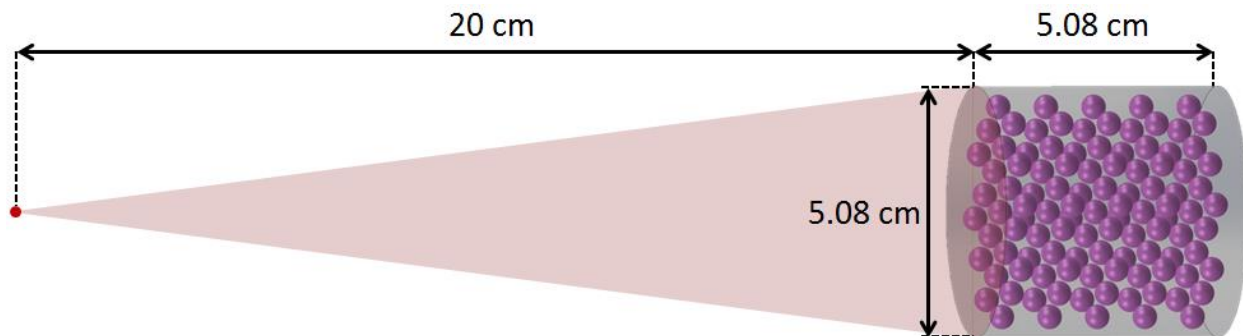
Fig. 6. MCNP model of a heterogeneous scintillator using EJ-299-33A and crystal spheres.

Fig. 7 shows a more detailed view of the crystal layer arrangement inside the plastic cylinder. Spheres were placed in a linear pattern, with a vertical and horizontal distance between each sphere equal to the diameter of the sphere. Three different iterations were tested for each plastic/crystal combination assuming crystal diameters of 2 mm, 3 mm, and 5 mm.
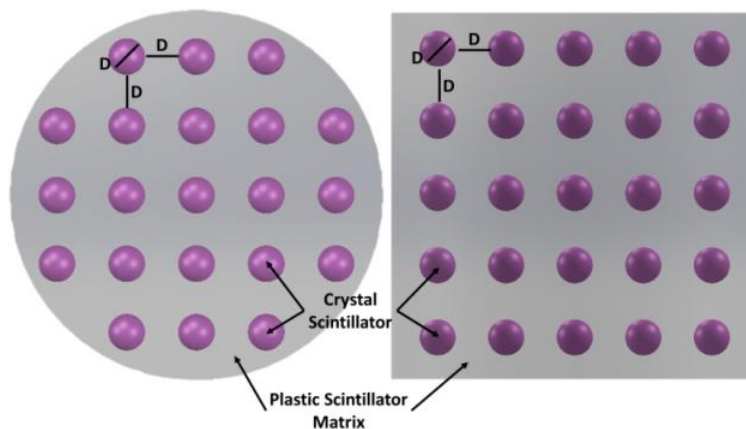
Fig. 7. Internal arrangement of modeled scintillator material.

Table 4 provides a quick break down of the simulation iterations with the list of the scintillator and diameter combinations which were computed with MCNP. The CLYC-6 was modeled with a ^{6}Li enrichment of 99.99% (0.01% ^{7}Li), while the CLYC-7 crystals assumed a ^{7}Li enrichment of 99.99% (0.01% ^{6}Li).

23

Table 4 – Scintillator Composition Details

Plastic Scintillator	Crystal Scintillator	Crystal Diameter
EJ-299-33A	CLYC-6	2-mm
		3-mm
		5-mm
	CLYC-7	2-mm
		3-mm
		5-mm
	CLLB	2-mm
		3-mm
		5-mm

Isotropic neutron point sources were defined with one of three initial energies (2.5-MeV, 4-MeV, 6-MeV) depending on the entry of the sdef card. Using the F8 tally option available in MCNP, the spectral distributions of the heterogeneous scintillator models were identified. Multiple F8 tally cards were added to each simulation file in order to collect the spectral distributions for photons, protons and alpha-particles as seen by the plastic and crystalline scintillator components. The results of these spectral distribution simulations are collected in Figs. 8-16.

Figs. 8-10 show the spectral distribution data for an EJ-299-33A plastic scintillator matrix containing several layers of CLYC-6 crystals with 2 mm diameters. Figs. 8a, b, and c offer a comparison of the spectral distributions due to incident neutrons from a 2.5-MeV source. Spectra were broken down into their component parts as alpha-particles (Fig. 8a), protons (Fig. 8b), and photons (Fig. 8c). Similar results are summarized in Figs 9a-c for a neutron source energy of 4-MeV, and in Figs 10a-c for a neutron source energy of 6-MeV. The CLYC-6 components easily picked up the spectral distributions of each particle of interest. Unlike the CLYC-6 scintillator which produced noticeable spikes in the alpha-particle spectrum for source energies of 2.5-MeV, 4-MeV, and 6-MeV, the plastic scintillator did not exhibit any peaks, or non-zero values for this spectral distribution (Figs. 8a, 9a, 10a). The proton spectra showed better results from the plastic component, but the magnitude of the spectral distribution values were far more noticeable for the CLYC-6 component as evidenced in Figs. 8b, 9b, 10b. The photon spectra results for the plastic and CLYC-6 components showed the greatest similarity (Figs. 8c, 9c, 10c), with CLYC-6 showing higher

counts below the energy threshold of 0.5 MeV, above this limit the spectral distribution of the EJ-299-33A exhibited higher counts per energy bin.

Fig. 8. (a) Alpha, (b) proton, and (c) photon responses of EJ-299-33A & CLYC-6 to 2.5 MeV source.

Fig. 9. (a) Alpha, (b) proton, and (c) photon responses of EJ-299-33A & CLYC-6 to 4 MeV source.
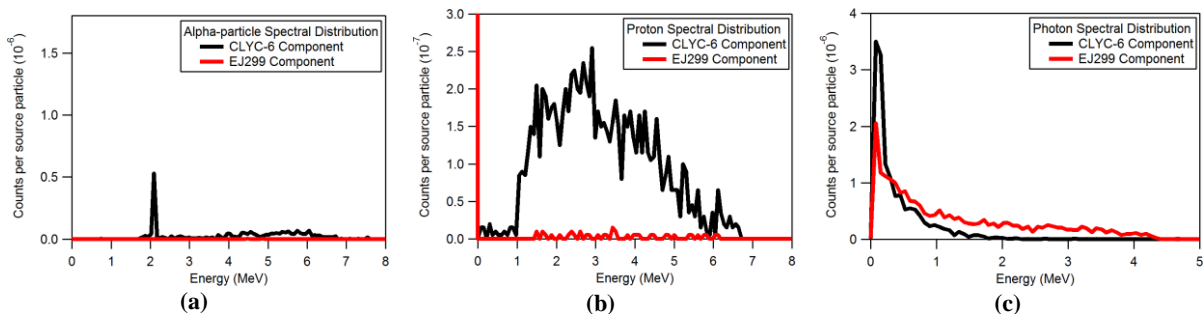
Fig. 10. (a) Alpha, (b) proton, and (c) photon responses of EJ-299-33A & CLYC-6 to 6 MeV source.

Figs. 11-13 show the spectral distribution data for an EJ-299-33A plastic scintillator matrix containing several layers of CLYC-7 crystals with 2 mm diameters. CLYC-7 components reported the spectral distributions of alpha-particles, protons, and photons for neutron source energies of 2.5-MeV (Figs. 11a-c), 4-MeV (Figs. 12a-c), and 6-MeV (Fig. 13a-c). The EJ-299-33A component did not exhibit any counts for the alpha-particle spectra (Figs. 11a, 12a, 13a), but it did record counts a magnitude lower than those

of the CLYC-7 component for the proton spectra (Figs. 11b, 12b, 13b). Photon spectra results showed the greatest similarity between the scintillators (Figs. 11c, 12c, 13c), with CLYC-7 showing higher counts below 0.5-MeV, and EJ-299-33A exhibiting higher counts above this energy bin.
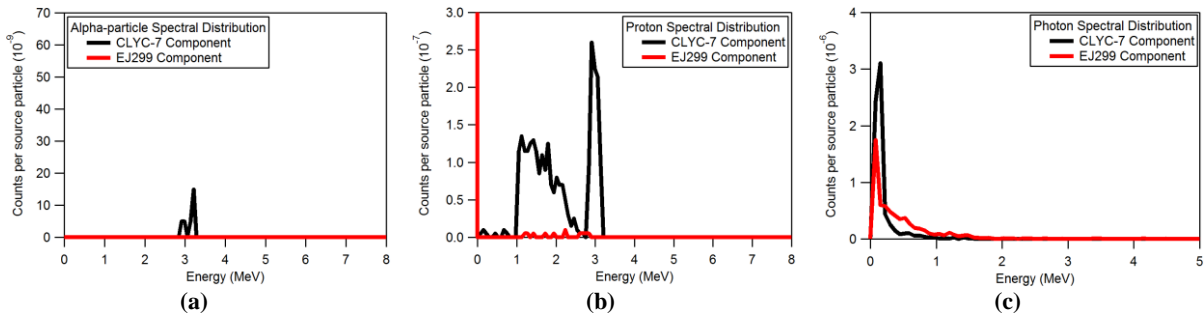
Fig. 11. (a) Alpha, (b) proton, and (c) photon responses of EJ-299-33A & CLYC-7 to 2.5 MeV source.
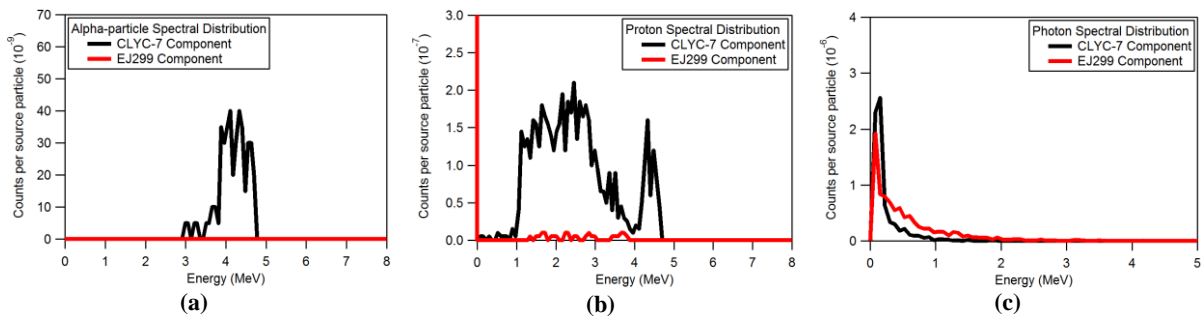
Fig. 12. (a) Alpha, (b) proton, and (c) photon responses of EJ-299-33A & CLYC-7 to 4 MeV source.
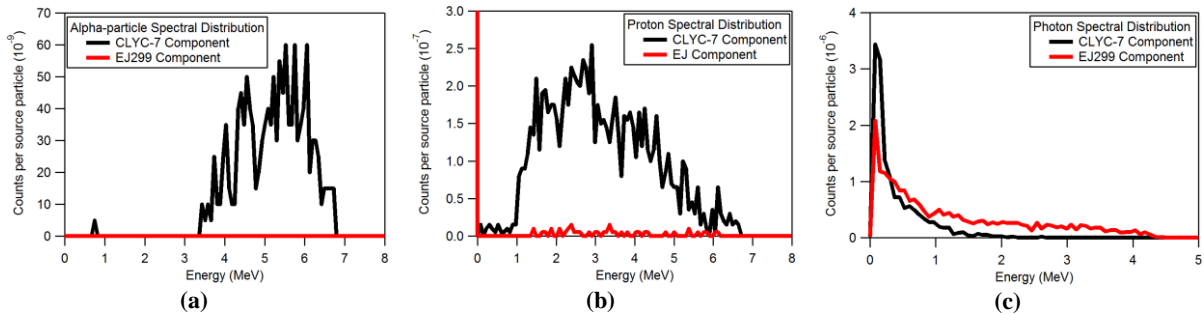
Fig. 13. (a) Alpha, (b) proton, and (c) photon responses of EJ-299-33A & CLYC-7 to 6 MeV source.

Figs. 14-16 show the spectral distribution data for an EJ-299-33A plastic scintillator matrix containing several layers of CLLB crystals with 2-mm diameters. CLLB components reported the spectral distributions of alpha-particles, protons, and photons for neutron source energies of 2.5-MeV (Figs. 14a-c), 4-MeV (Figs. 15a-c), and 6-MeV (Fig. 16a-c). The EJ-299-33A component did not exhibit any counts

for the alpha-particle spectra (Figs. 14a, 15a, 16a), but it did record counts a magnitude lower than those of the CLLB component for the proton spectra (Figs. 14b, 15b, 16b). Photon results for the plastic and CLLB components showed the greatest similarity (Figs. 14c, 15c, 16c), with CLLB showing higher counts below the 0.5-MeV energy bin, and EJ-299-33A exhibiting higher counts above this energy bin.
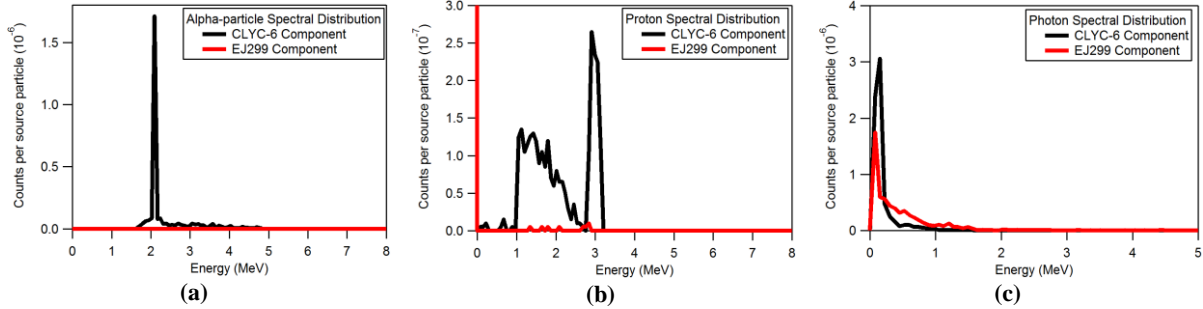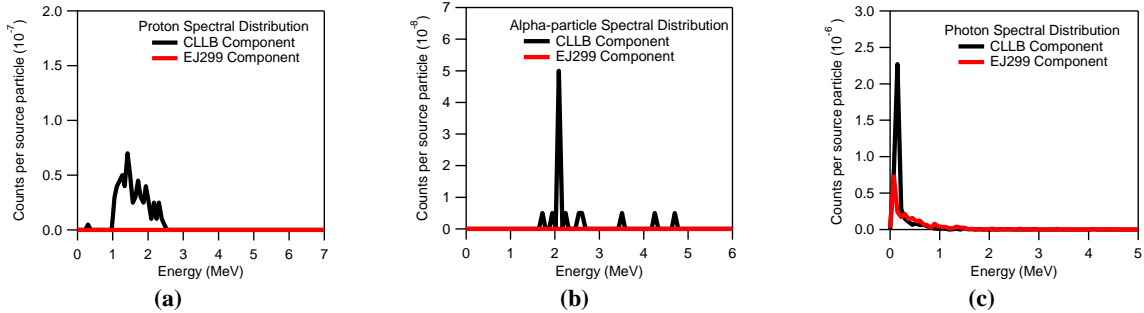

Fig. 14. (a) Alpha, (b) proton, and (c) photon responses of EJ-299-33A & CLLB to 2.5 MeV source.
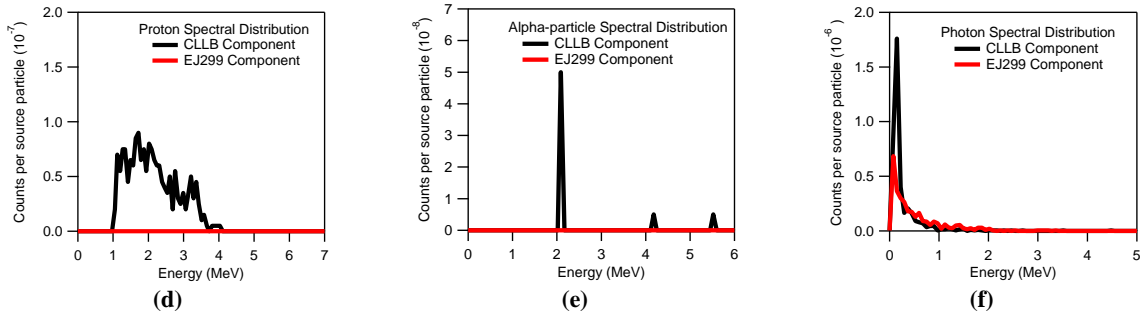
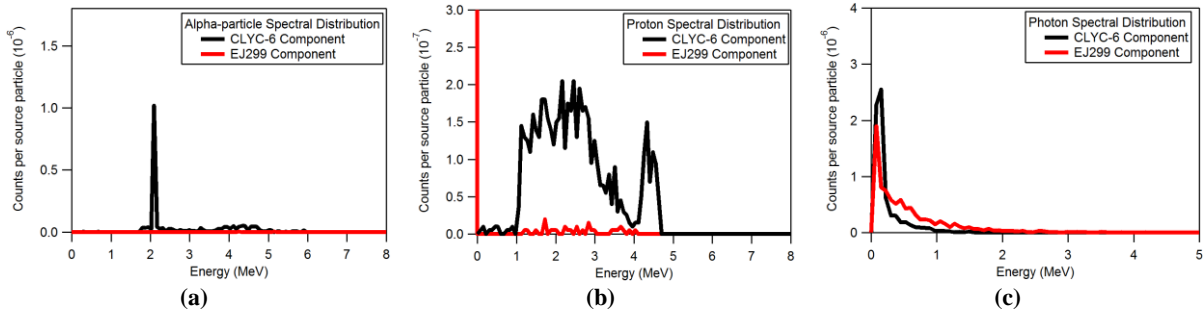**Fig. 15. (a) Alpha, (b) proton, and (c) photon responses of EJ-299-33A & CLLB to 4 MeV source.**
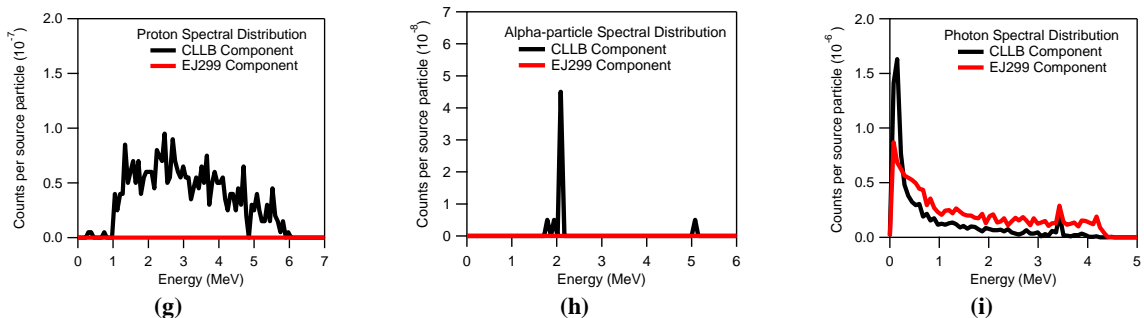
Fig. 16. (a) Alpha, (b) proton, and (c) photon responses of EJ-299-33A & CLLB to 6 MeV source.

The effect of the packing (volume) fraction on scintillator efficiency was studied for several variations of the EJ-299-33A/CLLB model. The CLLB material was defined with a ^{6}Li enrichment of 95%, and

27

models were developed for 5 layers of spherical CLLB crystals placed inside of an EJ-299-33A cylinder. Each layer was placed at a specific depth within the plastic matrix (Table 5).

Table 5 – CLLB Layer to Depth Correlation

Layer	Depth of Layer
1	0.55 cm
2	1.55 cm
3	2.55 cm
4	3.55 cm
5	4.55 cm

The depth was defined as the distance between the circular face of the plastic scintillator matrix and the central axis of the spheres. Figs. 17a and 17b show an example of how the depth of these layers remained constant while the diameter of the CLLB crystals was varied.

(a)   **(b)**
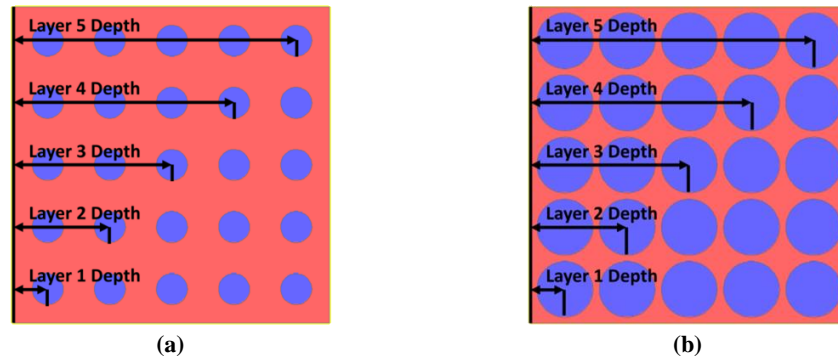
Fig. 17. CLLB layer placement in EJ-299-33A matrix for crystal diameters of (a) 5-mm, (b) 9-mm

The position of the spheres within a given layer was also fixed in relation to the central coordinate of each sphere. Figs. 18a and 18b show two views of the heterogeneous scintillator, looking perpendicularly at the circular face. A cross pattern was used to preserve the geometry through several iterations of the sphere diameter. Each sphere in a given layer was separated from its neighbors by a constant distance (X) as measured from the center of one sphere to the center of a neighboring cell's center. Using this layout, it was possible to vary the sphere diameters from 1 mm to 10 mm in 1 mm increments without making additional changes to the geometry of the heterogeneous scintillator model or being required to reduce the total number of crystal spheres in each layer.
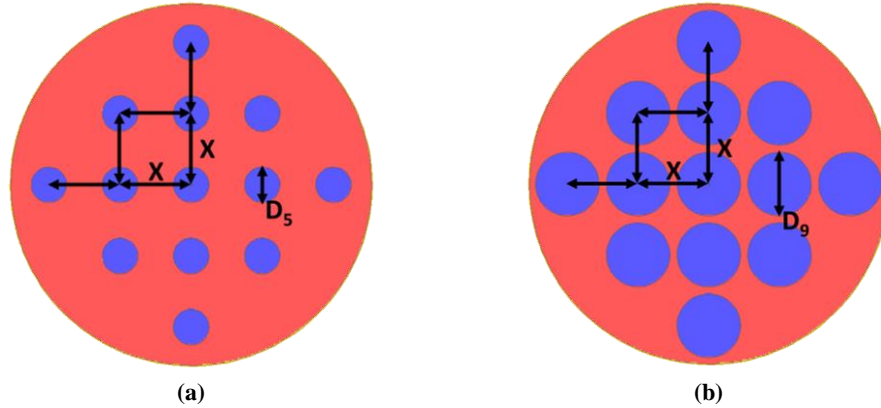
(a) **(b)**
Fig. 18. Geometry for individual CLLB crystal layers with diameters of (a) 5-mm, (b) 9-mm

Knowing that the model possessed 5 layers of crystals, with 13 crystals per layer, it was possible to determine the total volume of CLLB material in the heterogeneous scintillator. This value was subsequently used to identify the Packing Fraction of the CLLB which was defined as the ratio of the CLLB volume to the total volume encompassed by the 5.08 cm by 5.08 cm cylinder of EJ-299-33A (103 cm^3). Table 6 reports the different volumes and packing fractions with respect to the CLLB crystal diameters modeled. Increasing the crystal diameter by a factor of 10 would increase the packing fraction of the CLLB by a factor of 1000.

Table 6 – CLLB Model Packing Fractions

Diameter (mm)	CLLB Volume (cm^3)	Packing Fraction (CLLB/Total)
1	0.034	3.3E-4
2	0.272	2.6E-3
3	0.919	8.9E-3
4	2.178	2.1E-2
5	4.254	4.1E-2
6	7.351	7.1E-2
7	11.674	0.1134
8	17.425	0.1692
9	24.811	0.2410
10	34.034	0.3305

Scintillator efficiency was based on the reaction rate for ^{6}Li(n,α) and was directly influenced by the value of the CLLB packing fraction (Fig. 19).
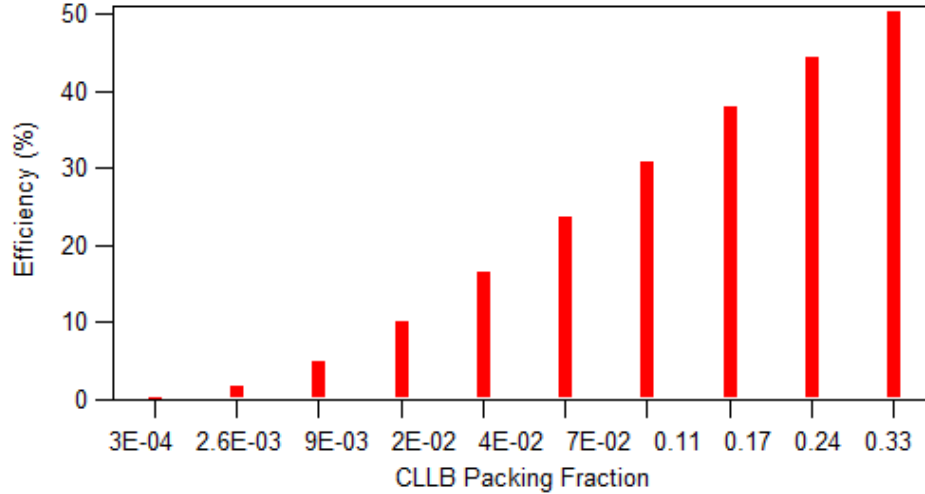
Fig. 19. Efficiency of CLLB component based on ^{6}Li(n,α) reaction rate for different packing fractions.

Isolating the reaction rate data by layer made it possible to determine the contribution of each layer to the overall efficiency. Fig. 20 shows a comparison of this data. The crystal layer closest to the source consistently produces the greatest contribution, with larger diameters having higher contributions.
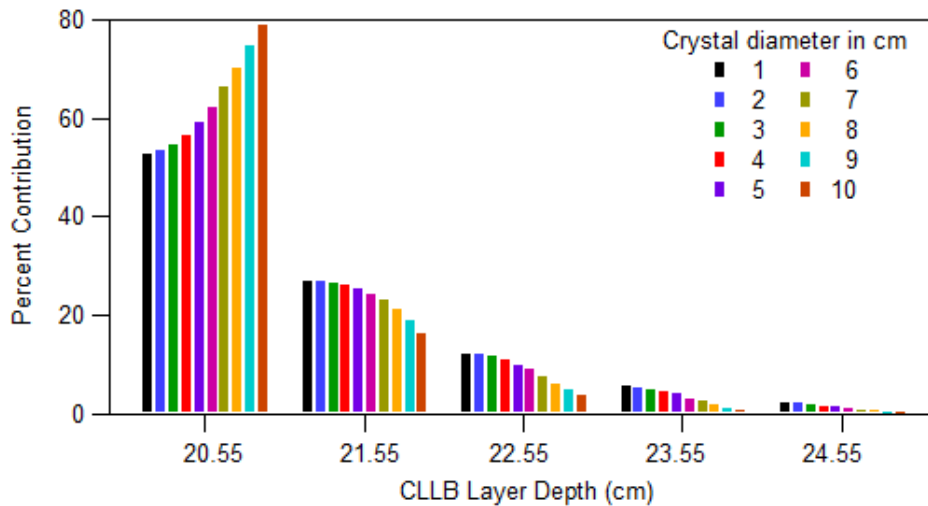
Fig. 20. Effect of diameter and layer depth on contribution of CLLB crystals to detector efficiency.

Feasibility of various scintillators was examined for fast neutron detection. Simulations were broken into two parts. The first step was the study of EJ-299-33A plastic scintillator to determine its efficiency and suitability for fast neutron detection. Models were developed for 2.5-MeV and 14-MeV neutron beams incident upon a scintillator cell. These energies were selected to simulate Deuterium-Deuterium (DD) and

30

Deuterium-Tritium (DT) accelerator sources which are commercially available. For each beam, the depth of the scintillator and the area of the scintillator surface which faced the beam were varied to study the effect of these dimensions on the neutron induced reaction rates occurring within the scintillator cell. These reaction rates were used as an indication of the efficiency of the scintillator cell. The overall trend in data indicated that larger cell volumes had the potential for higher reaction rates.

The efficiency of heterogeneous scintillators for fast neutron detection was also considered. For this work, heterogeneous scintillators were defined as a single, cylindrical cell of plastic scintillator material with several layers of crystal scintillator spheres arranged inside of it. Isotropic neutron point sources were defined with energies of 2.5-MeV, 4-MeV, and 6-MeV. Simulations were performed for the crystal scintillators CLYC-7, CLYC-6, and CLLB. Although the plastic scintillator component remained a constant size, the diameter of the crystal spheres was varied to determine if there was an ideal size at which the plastic/crystal combination would work best. Quantitative results were reported using the pulse height tally available in MCNP6. Separate tallies were added to each simulation to track the spectral distribution of photons, protons, and alpha-particles as seen by the plastic and crystal components. Additional simulations were carried out to identify the impact that the packing fraction of a crystal scintillator had on the overall efficiency of the heterogeneous scintillator cell using the reported reaction rates for ^{6}Li(n,α). In addition, the heterogeneous scintillators enable photon spectroscopy.

CHAPTER 4 – NEUTRON DETECTOR ARRAY MODELING

Cross-Talk Simulations

After determining the viability of detector materials for fast neutron detection, the next step was computational modeling of detector arrays. The detector array was defined as a set of detectors, each a single block of scintillation material acting as a pixel. The greatest challenge in developing these detector arrays was the occurrence of cross-talk between detector cells. Fig. 21 illustrates this multi-step phenomenon. First an incident particle (or radiation) enters a detector cell, interacting with the material there. Assuming a collision with one or more atoms of the material, the particle will lose a portion of its energy causing a scintillation event before leaving the cell. The flash of light from this event is translated into a waveform by the detector instrumentation. Upon exiting the first cell, the particle may enter a neighboring detector cell, depositing some or all of its remaining energy through interactions and causing a new scintillation event. In this case both detector cells will register the same incident particle as different particles, each generating a unique response based on the energy deposited.
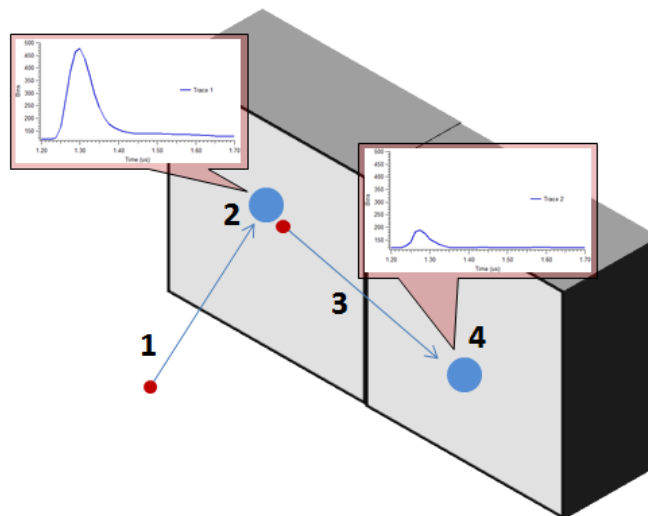
Fig. 21. Cross-talk example

This made it necessary to consider the effects of cross-talk on the measurements collected from a given detector array. The F4 tally available in MCNP6 was used to report the average flux for each detector cell in particles/cm^2 and normalized per starting particle. The addition of cell flagging (CF) cards to each tally made it possible to track particles as they entered and exited the different "pixels" in the detector array by creating an additional bin to store flagged contributions. Figs. 22a and b show examples of the tallies used for these input files. Fig. 22a shows the cards for tally 10004 which was designed to track neutron contributions to each of the 25 detector cells and report a single average-flux value per cell. The addition of the cell flagging card (CF10004) told MCNP6 to generate an additional data set for each reported flux value for tally 10004, recording the average-flux value considering only those neutrons which were flagged as having passed through at least one of the cells listed on the CF10004 card first. Fig. 22b shows the card for tally 10014 which was designed to track neutron contributions to each of the 25 detector cells and report a single average-flux value per cell. In this case, the cell flagging card CF10014 told MCNP6 to generate an additional data set for each reported flux value for tally 10014, recording the average-flux value considering only those neutrons which were flagged as having passed through detector cell 20001 first. These tally and cell flagging cards were repeated in the input file to identify the contribution to each average flux value caused by particles passing through other cells first. Additional tally and cell flagging cards were included in the input deck for the purpose of tracking and tallying the photon contributions to each of the detector cell responses.

```
F10004:N 20001 20002 20003 20004 20005 20006 20007 20008 20009
         20010 20011 20012 20013 20014 20015 20016 20017 20018
         20019 20020 20021 20022 20023 20024 20025
CF10004  20001 20002 20003 20004 20005 20006 20007 20008 20009
         20010 20011 20012 20013 20014 20015 20016 20017 20018
         20019 20020 20021 20022 20023 20024 20025
```
(a)
```
F10014:N 20001 20002 20003 20004 20005 20006 20007 20008 20009
         20010 20011 20012 20013 20014 20015 20016 20017 20018
         20019 20020 20021 20022 20023 20024 20025
CF10014  20001
```
(b)
Fig. 22. Cell flagging of neutrons (a) leaving any cell in the array, (b) leaving a specific cell in the array

Cross-talk simulations were performed for "staggered" and "packed" detector array systems assuming a neutron beam with a user-defined position and energy (*pos* and *erg* values in Fig. 23). These simulations were tested for several combinations of neutron beam position and energy, with the outputs being exported to excel for processing and comparison.

```
c ================ SOURCE TERM =================
c
sdef pos=2.5 2.5 0.0 axs=0 0 1 ext=0  par=n erg=6.0 vec=0 0 1 dir=1
```
Fig. 23. SDEF card for 6-MeV Neutron Beam

Packed Detector Simulations

A standard set-up for detector arrays makes use of a "packed" arrangement, where individual detectors are grouped together either in close contact or with a thin layer of material or shielding placed between each scintillator cell to reduce the potential occurrence of cross-talk. The simulation geometry for the packed detector simulations is shown in Fig. 24. Each simulation used a single neutron beam, which was defined to be mono-energetic with a designated energy and direction. The detector array consisted of a 25 scintillator detectors arranged in a 5 × 5 grid, where each detector was in direct contact with neighboring scintillator cells. Initial simulations assumed the dimensions of each scintillator cell to be 1 cm × 1 cm × 1.5 cm. This size was selected due to commercial availability of crystal scintillators at this size. It is possible to grow larger crystals, but the process is still a lengthy one, and the presence of defects in larger crystals is more likely than those of a smaller size.
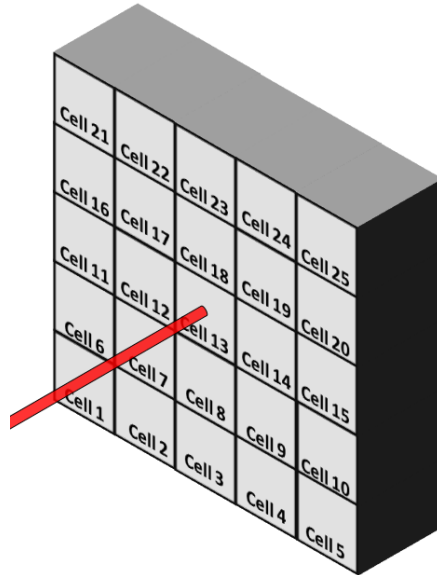
Fig. 24. Simulation model for packed detector array.

In addition to varying the scintillator material and the dimensions of the scintillator cells used in each simulation, several versions of the packed detector model were completed with different position cards used to define the origin of the beam source. Each beam remained oriented perpendicularly to the detector array as shown in Fig. 24, but changes to the beam origin changed the point on the detector array where the incident particles from the beam were focused (Fig. 25).
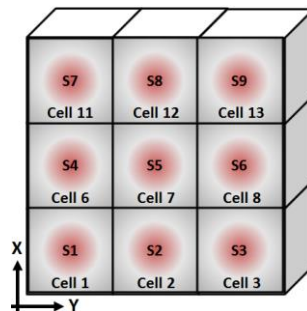
Fig. 25. Neutron beam focus relative to cells

Nine beam impact locations were tested, each positioned to line up with the center of a different detector cell. Beam 1 was centered on Cell 1, Beam 4 centered on Cell 6, Beam 7 was centered on Cell 11, etc., as demonstrated by the red circles in Fig. 25. This variation allowed for comparison of cross-talk effects based on beam position. Figs. 26a and b show examples of the simulation results for the CLYC-6

scintillator material using a 6-MeV neutron beam source with incident neutron particles focused on Cell 13. Cell 13 reported the largest average flux without considering cross-talk (Fig. 26a), this outcome was expected since incident particles were specifically aimed at this cell. Fig. 26b represents the average flux for each detector cell assuming the tracked particles had previously left at least one other detector cell in the array. Since most incident particles would enter the detector array at Cell 13, this cell showed the smallest potential for cross-talk. It did exhibit a non-zero value, indicating that some particles may have exited Cell 13, entered another cell, and been reflected back into Cell 13. This contribution was minimal compared to the data for neighboring Cells 8, 12, 14, and 18.

The data in Figs. 26a and b used vertical units of neutrons/cm^2 and horizontal units of pixels. These units were used consistently for all cross-talk data plots, but to preserve the clarity of the figures units were not printed on the axis for each figure.
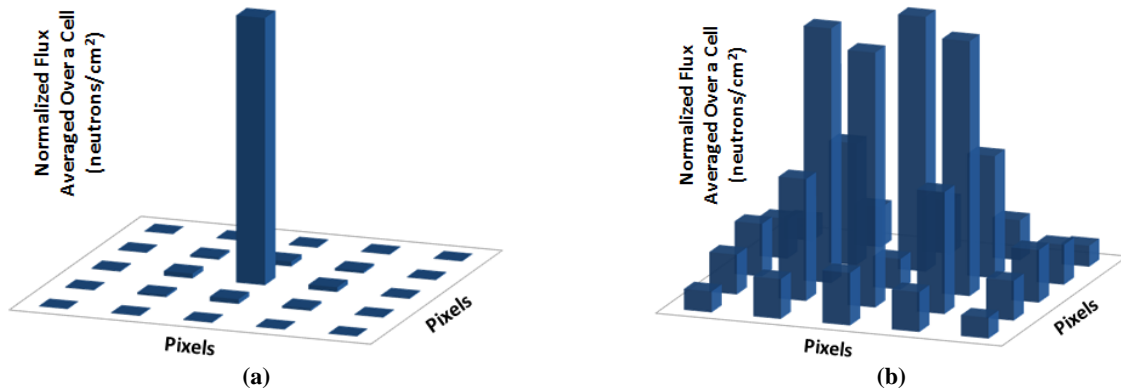
Fig. 26. (a) Average flux and (b) flagged cross-talk contributions for EJ-299-33A using a 6-MeV neutron beam

Combining the F4 tally with a CF card for a single cell made it possible to track the contribution to the average flux per cell caused by the cross-talk generated from a specific cell. Figs. 27a-y show the breakdown of these results for each designated cell shown in Fig. 26b. Each plot shows the average flux in the detector array due only to particles that are flagged as they leave a specific cell. As an example, Fig. 27a shows the flagged contributions tallied in each detector cell, assuming the tallied particle exited Cell 21 before being tallied. Fig. 27b shows similar flagged contributions, assuming the tallied particle exited Cell 22 before being tallied.
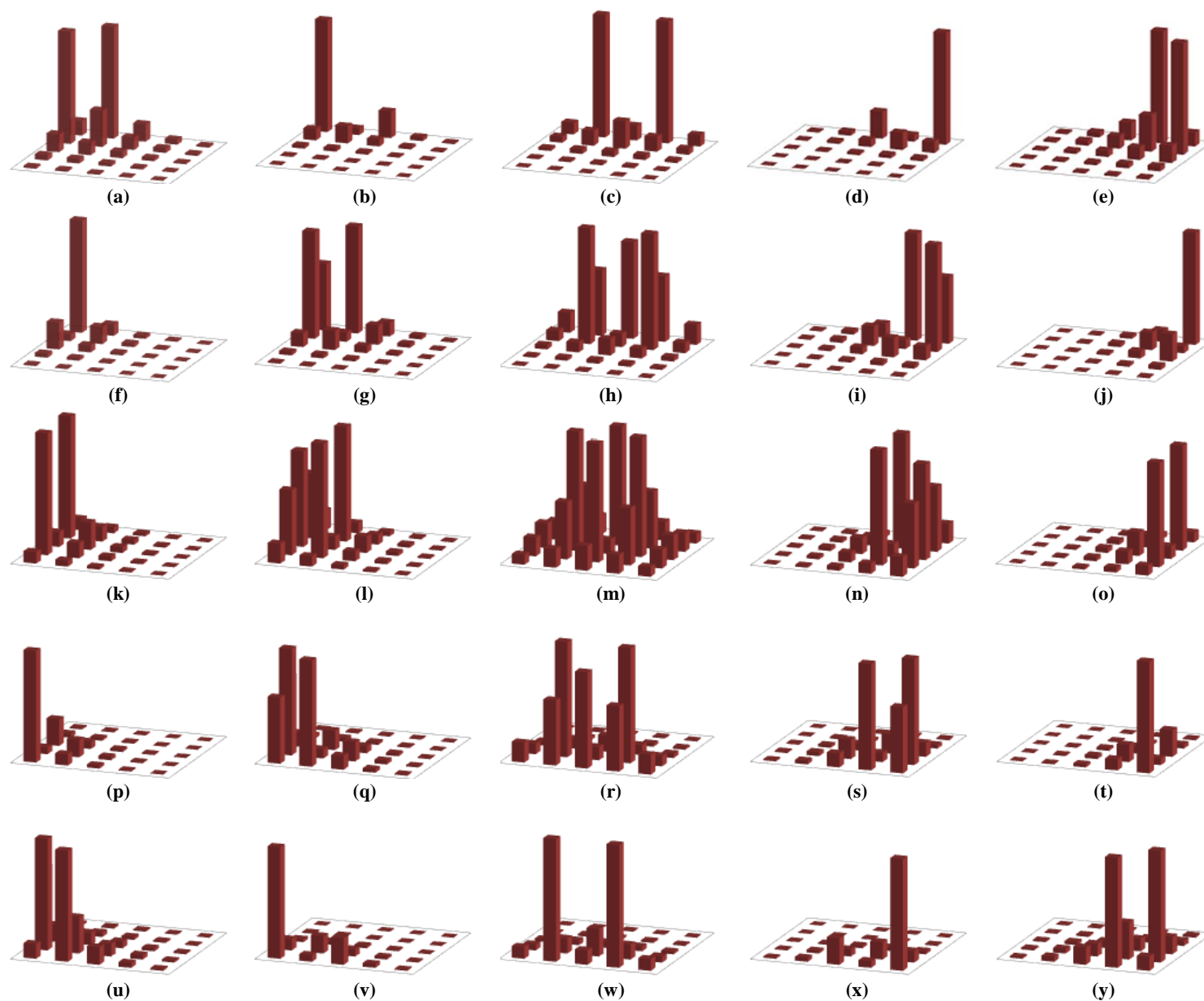
Fig. 27. Average flux from flagged particles for EJ-299-33A scintillator using a 6-MeV neutron beam

The cross-talk contributions for several plastic scintillator simulations are summarized below in Figs. 28-30. Fig. 28a displays the cross-talk contributions due to particles leaving Cell 1, compared with Fig. 28b which shows the cross-talk contributions due to particles leaving any of the cells within the detector array prior to depositing energy in a different cell. Fig. 29a displays the cross-talk contributions due to particles leaving Cell 5, compared with Fig. 29b which shows the cross-talk contributions due to particles leaving any of the cells within the detector array prior to depositing energy in a different cell. Fig. 30a displays the cross-talk contributions due to particles leaving Cell 9, compared with Fig. 30b which shows the cross-talk contributions due to particles leaving any of the cells within the detector array prior to depositing energy in a different cell.

(a)   **(b)**

Fig. 28. (a) Cross-talk and (b) cross-talk summation contributions for beam position 1

(a)   **(b)**

Fig. 29. (a) Cross-talk and (b) cross-talk summation contributions for beam position 5

(a)   **(b)**

Fig. 30. (a) Cross-talk and (b) cross-talk summation contributions for beam position 9

The reduction of cross-talk effects was also studied by adding lead shielding between the scintillator elements of the model. The selection of lead was considered to reduce photon cross-talk component. Fig. 31 shows the modified detector array used for these simulations. The same 25 pixel grid was used, but an additional 1 mm layer of lead was placed between each of the scintillator cells. Since only a very thin layer of lead was used, the impact on neutron measurements was expected to be negligible, while reduction of interference due to photons would be maximized. Assuming the use of 1 mm thick lead plates to surround the sides of each cubic cell (1 cm dimensions) while leaving each front (facing the source) and back (surface coupled to a PMT) face, this would add an additional weight of 0.76 lbs to the array, with each millimeter of thickness added to the lead shielding increasing the weight of the array by an additional 0.76 lbs. By increasing the size of the scintillator cells to 5.08 cm × 5.08 cm with a 1 cm depth and maintaining a lead thickness of 1 mm the weight of the array would be increased by 3.8 lbs. Each subsequent millimeter of lead would add an extra 3.8 lbs. If the depth of the scintillator cells was increased to 5.08 cm, the weight of the lead would increase to 19.4 lbs, with each additional millimeter of lead shielding adding another 19.4 lbs.
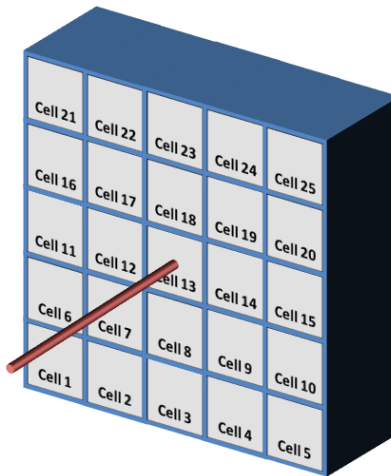
Fig. 31. Simulation model for packed detector array with lead shielding.

Simulations were performed for 1-MeV, 2.5-MeV, 6-MeV, and 14-MeV neutron beams incident upon a detector array with 1 mm sheets of lead placed between the individual scintillator cells. Results from

these simulations are reported in Figs. 32 and 33, where color coding of data sets is used to indicate the cross-talk data produced by a given neutron beam energy. In these plots, 1-MeV neutron beam data is denoted by dark blue, 2.5-Mev neutron beam data is identified by light blue, 6-MeV neutron beam data uses green, and 14-MeV neutron beam data is colored yellow. It is interesting to note that the lower energy neutron beams exhibit larger cross-talk contributions than higher energies, but this can be explained by the difference in material interactions caused by the energy difference. Comparing the cross-talk contribution depicted in Fig. 32 for Cell 18 (Tally 10184), the largest contribution to cross-talk was due to radiation from the 1-MeV neutron beam, while the lowest contribution was caused by the 14-MeV neutron beam.

Each figure shows a comparison of the cross-talk contribution caused by each cell within the detector array. Fig 32 displays the cross-talk data for each shielded cell, with each plot assigning a maximum value to the vertical axis based on the highest count per source particle reported for that tally. This demonstrated the occurrence of cross-talk despite the focus of the neutron beam being several cells away. Magnitudes of the reported counts per source particle for a given tally varied by factors as large as 100. Fig. 33 provides a visual comparison of the overall impact of the cross-talk occurring between the detector array cells. For this case, each subplot's vertical axis was normalized using the maximum value of counts/source particle reported by the simulations being compared. Although it gives the appearance that no cross-talk occurs in cells farther from the focus of the neutron beam, this is due only to the scale of the vertical axis.

Tally10214-N,CF   Tally10224-N,CF   Tally10234-N,CF   Tally10244-N,CF   Tally10254-N,CF

Tally10164-N,CF   Tally10174-N,CF   Tally10184-N,CF   Tally10194-N,CF   Tally10204-N,CF

Tally10114-N,CF   Tally10124-N,CF   Tally10134-N,CF   Tally10144-N,CF   Tally10154-N,CF

Tally10064-N,CF   Tally10074-N,CF   Tally10084-N,CF   Tally10094-N,CF   Tally10104-N,CF

Tally10014-N,CF   Tally10024-N,CF   Tally10034-N,CF   Tally10044-N,CF   Tally10054-N,CF

Fig. 32. Cross-talk contributions for neutron beams focused on Cell 9 of shielded model

Tally10214-N,CF   Tally10224-N,CF   Tally10234-N,CF   Tally10244-N,CF   Tally10254-N,CF

Tally10164-N,CF   Tally10174-N,CF   Tally10184-N,CF   Tally10194-N,CF   Tally10204-N,CF

Tally10114-N,CF   Tally10124-N,CF   Tally10134-N,CF   Tally10144-N,CF   Tally10154-N,CF

Tally10064-N,CF   Tally10074-N,CF   Tally10084-N,CF   Tally10094-N,CF   Tally10104-N,CF

Tally10014-N,CF   Tally10024-N,CF   Tally10034-N,CF   Tally10044-N,CF   Tally10054-N,CF

Fig. 33. Normalized cross-talk contributions for neutron beams focused on Cell 9 of shielded model

Staggered Detector Simulations

A novel option that recently received attention is the use of a detector array comprised of independent detectors, placed so that they cover a solid angle of emission despite being spaced out [129]. Due to the limited range of most radiations in air, the distance between the detectors should reduce the potential of cross-talk between the different detectors. Although it can significantly reduce the potential occurrence of cross-talk, the gaps between the detectors can lead to the presence of artifacts when data is subjected to reconstruction processes and treatments [129]. This trade-off can be exploited by reducing and optimizing the gap distance between detectors so as to minimize the occurrence of both cross-talk and artifacts.

Fig. 34 shows the geometry used to model a staggered detector arrangement for this purpose. Cubic scintillator cells were modeled in two rows using a staggered checkerboard pattern to effectively eliminate gaps between the detectors without causing artifacts due to empty array volumes.
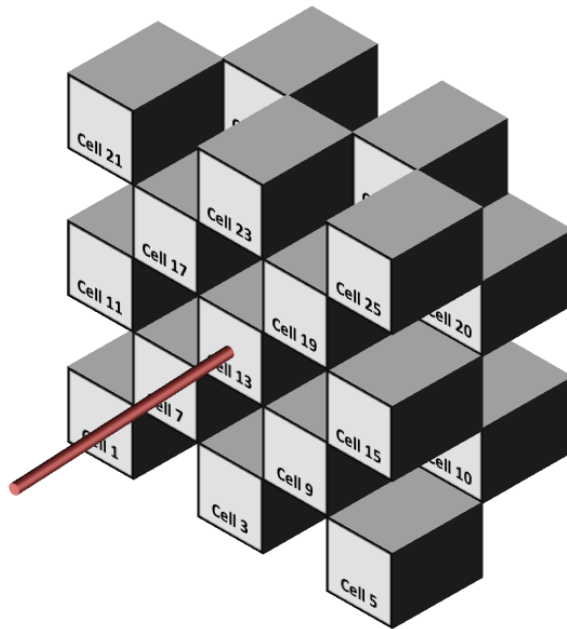
Fig. 34. 3D view of staggered array used in simulations

Simulations were performed for 2.5-MeV and 14-MeV neutron beams incident upon a detector array with a staggered checkerboard pattern of scintillator cells. Results from these simulations are reported in Figs.

35 and 36, where color coding of data sets is used to indicate the cross-talk data produced by a given neutron beam energy. In these plots, 2.5-MeV neutron beam data is denoted by dark blue and 14-MeV neutron beam data is colored yellow. As in the previous simulations with shielded scintillator cells, the lower energy neutron beam appeared to cause larger cross-talk contributions than the 14-MeV neutron beam.

Each figure shows a comparison of the cross-talk contribution caused by each cell within the detector array. Fig 35 displays the cross-talk data for each shielded cell, with each plot assigning a maximum value to the vertical axis based on the highest count per source particle reported for that tally. This demonstrated the occurrence of cross-talk despite the focus of the neutron beam being several cells away. Magnitudes of the reported counts per source particle for a given tally varied by factors as large as 100. Fig. 36 provides a visual comparison of the overall impact of the cross-talk occurring between the detector array cells. For this case, the upper limit of each subplot's vertical axis was defined using the maximum value of counts per source particle reported by the simulations being compared. Although it gives the appearance that no cross-talk occurs in cells farther from the focus of the neutron beam, this is due only to the scale of the vertical axis.
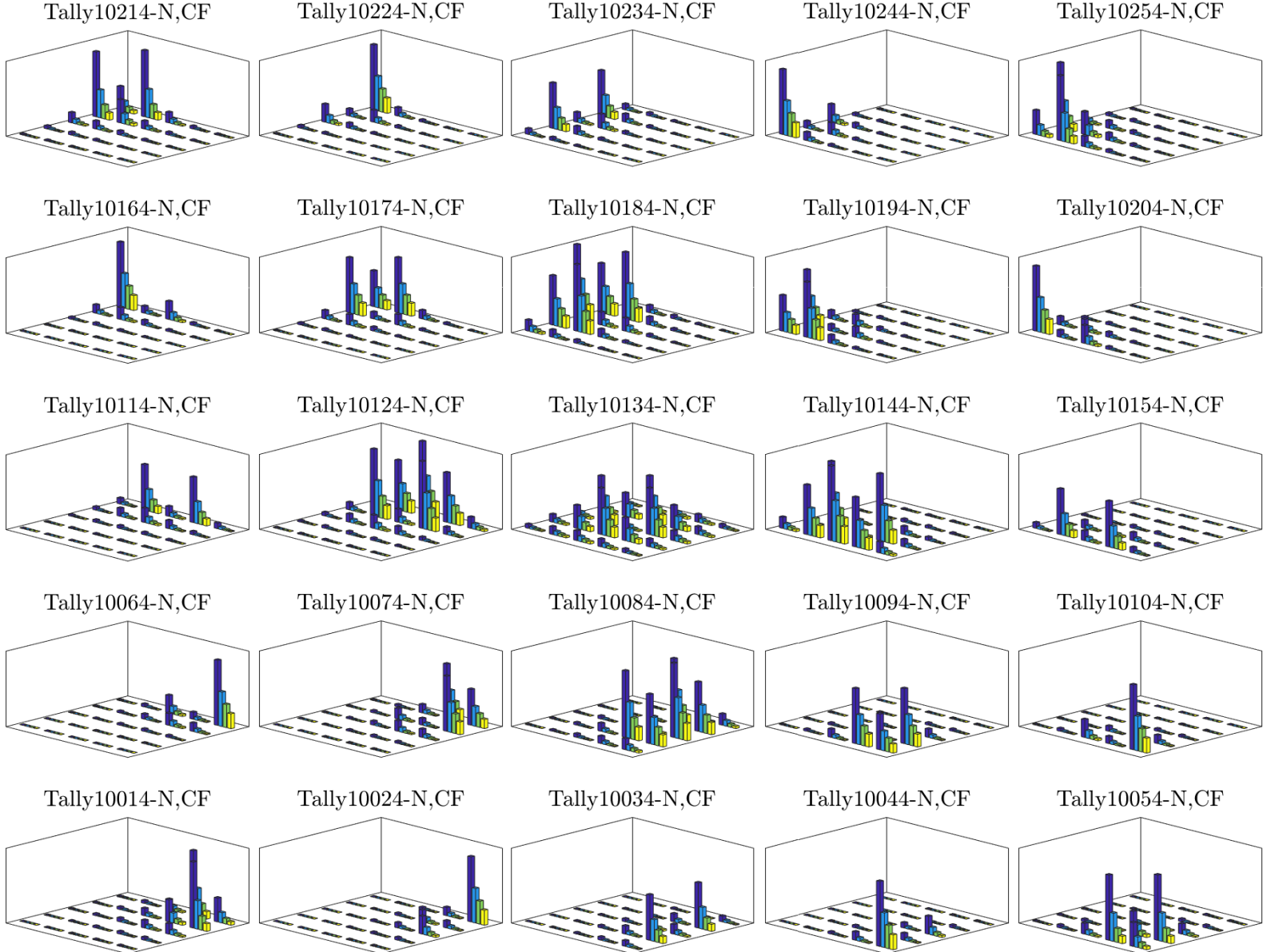
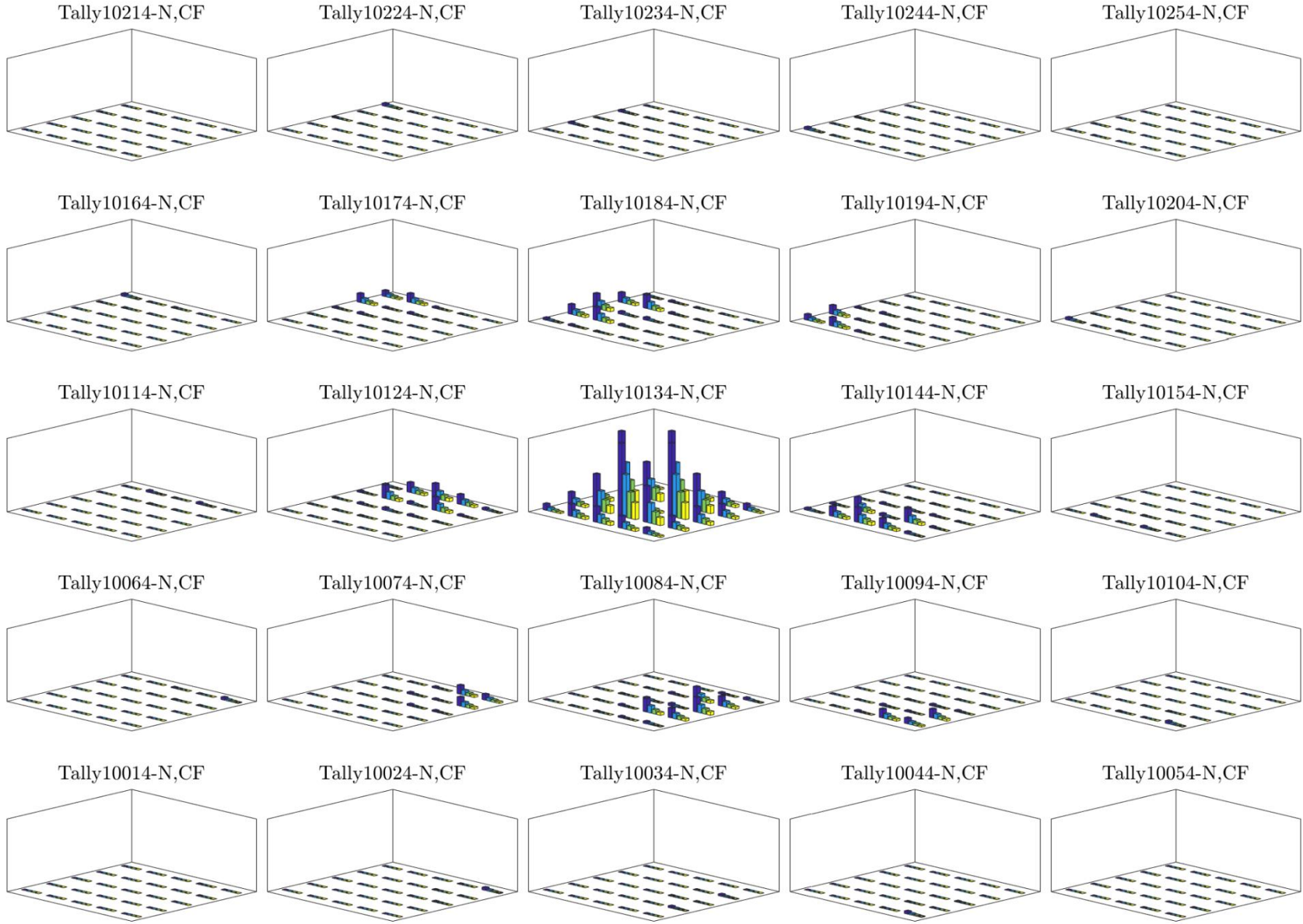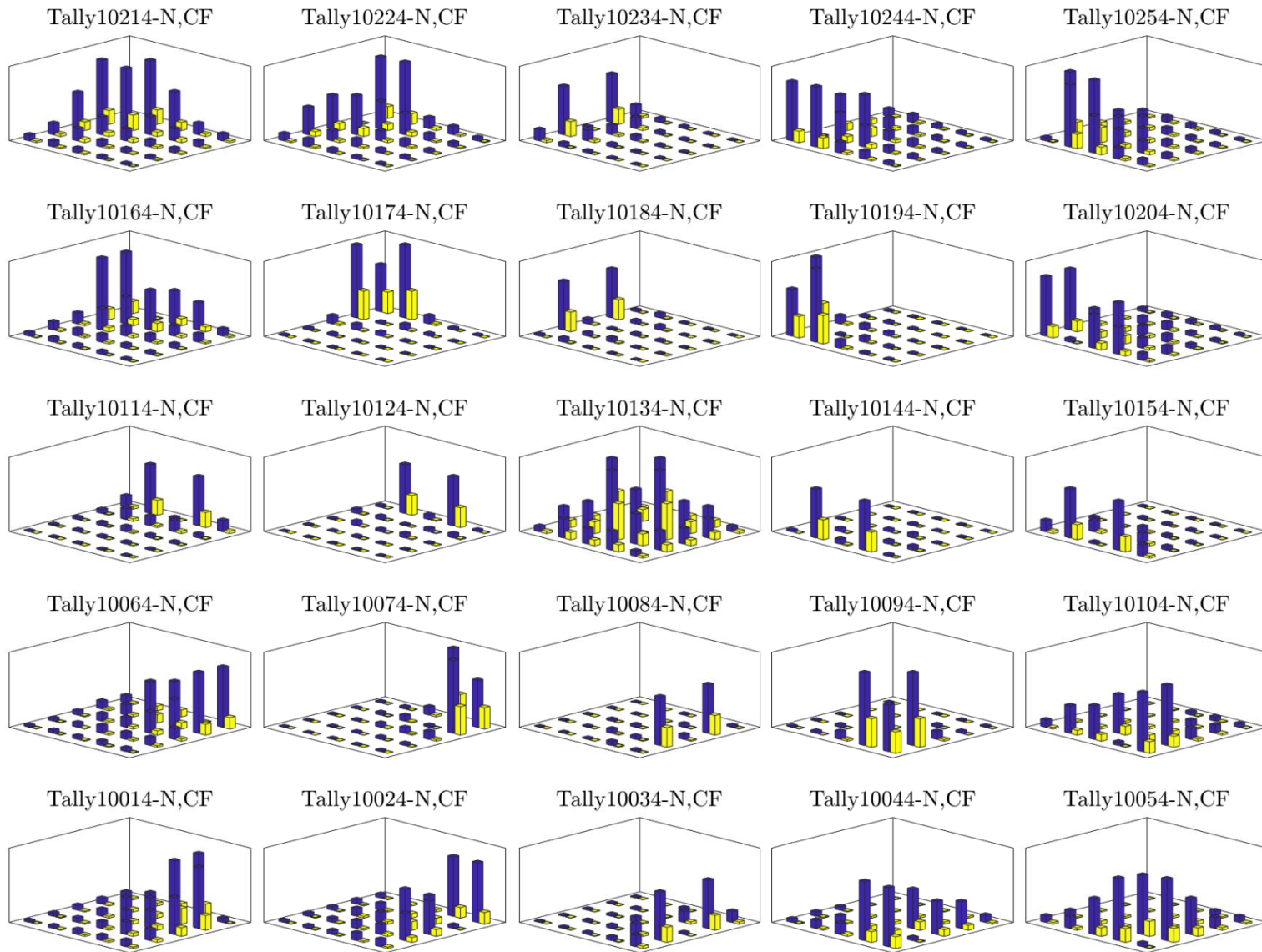**Fig. 35. Cross-talk contributions for neutron beams focused on Cell 9 of staggered model**
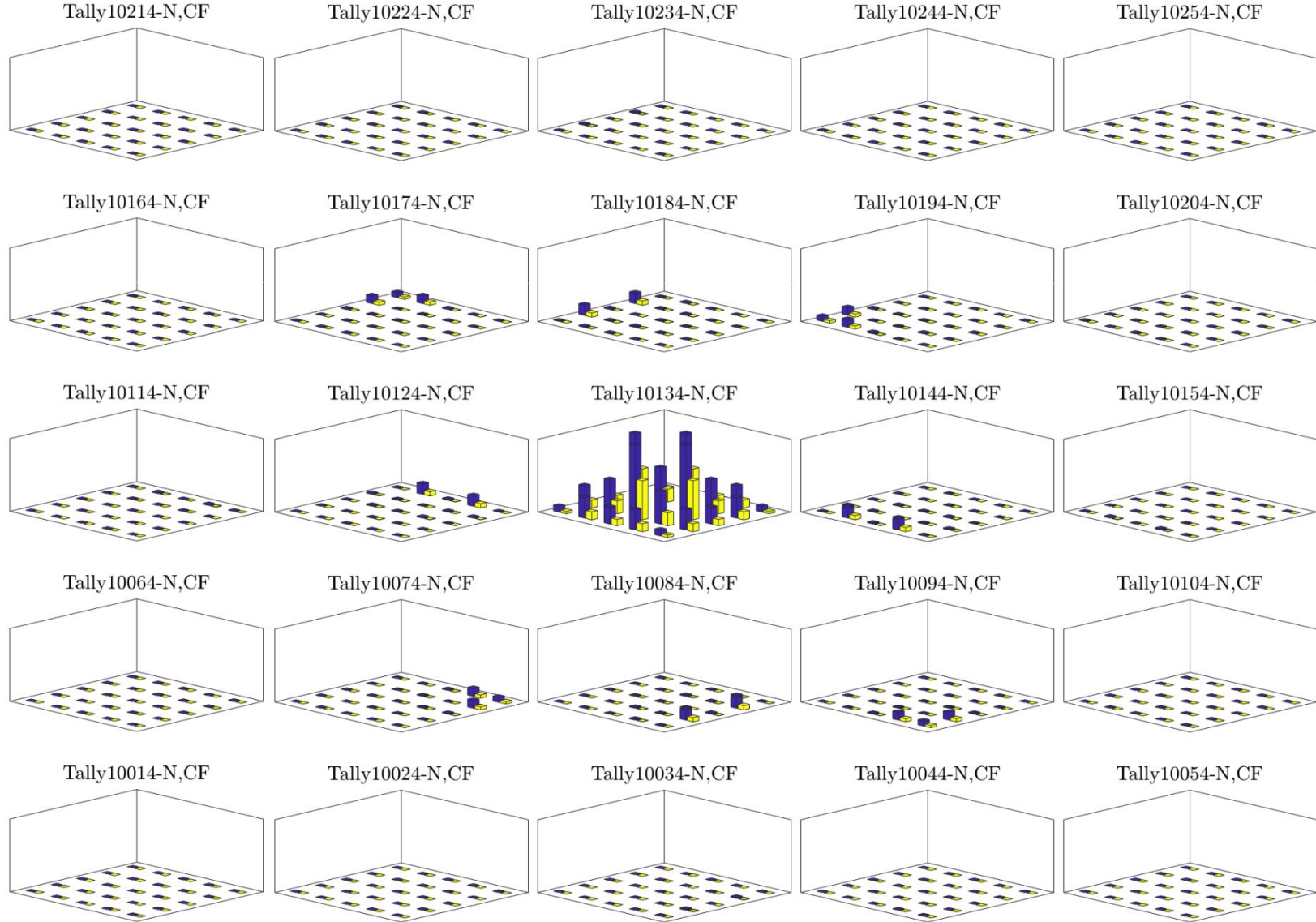
Fig. 36. Normalized cross-talk contributions for neutron beams focused on Cell 9 of staggered model

Figs. 37-40 are comparisons of the cross-talk responses reported for the unshielded packed array, the lead shielded scintillator array, and the staggered array. Figs. 37 and 38 show the effect of these three system models on cross-talk for a 2.5-MeV neutron beam. Figs. 39 and 40 show the effect of the system models on cross-talk for a 14-MeV neutron beam. Each figure uses the same color scheme to identify data from a specific system model. Cross-talk data from the unshielded scintillator model appears in dark blue. The dark blue identifies data from the array model which used 1mm lead to wrap the scintillator cells. Yellow is used for cross-talk data from the staggered array model.

Although the shielding method showed a reduction in cross-talk for both the 2.5-MeV and 14-MeV neutron beams, the effect was not large enough to justify the additional difficulty and weight of machining and adding lead sheets to the detector array. Similarly, the reduced cross-talk occurrence shown by the staggered array was not sufficient enough to make it worth increasing the dimensions of the detector array and potentially limiting the ease of transporting the detector array.

Tally10214-N,CF   Tally10224-N,CF   Tally10234-N,CF   Tally10244-N,CF   Tally10254-N,CF

Tally10164-N,CF   Tally10174-N,CF   Tally10184-N,CF   Tally10194-N,CF   Tally10204-N,CF

Tally10114-N,CF   Tally10124-N,CF   Tally10134-N,CF   Tally10144-N,CF   Tally10154-N,CF

Tally10064-N,CF   Tally10074-N,CF   Tally10084-N,CF   Tally10094-N,CF   Tally10104-N,CF

Tally10014-N,CF   Tally10024-N,CF   Tally10034-N,CF   Tally10044-N,CF   Tally10054-N,CF

Fig. 37. Comparison of cross-talk contributions to average flux for packed, shielded, and staggered arrays for 2.5-MeV neutron beam focused on Cell 9
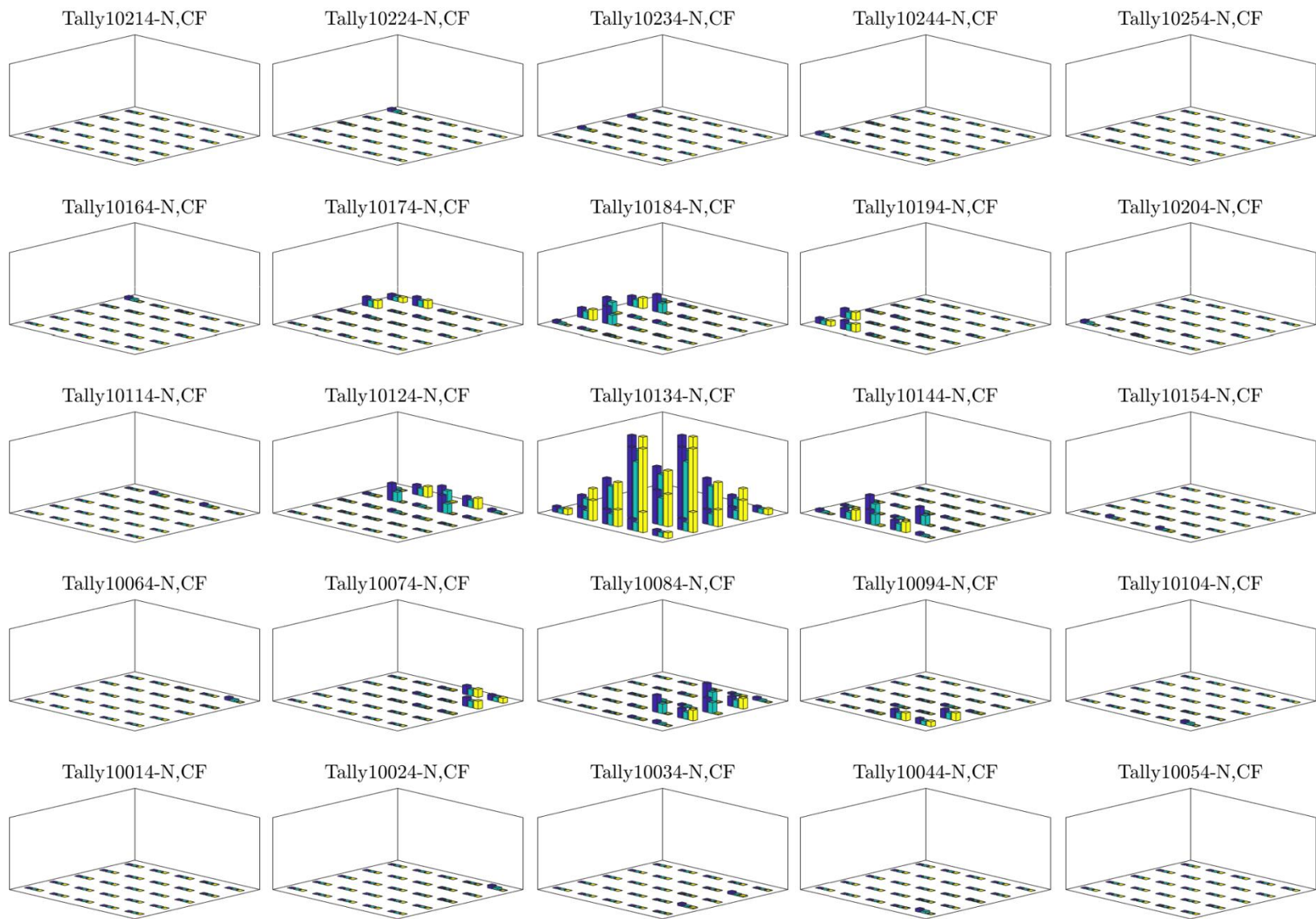
Fig. 38. Comparison of cross-talk contributions to average flux for packed, shielded, and staggered arrays for 2.5-MeV neutron beam focused on Cell 9
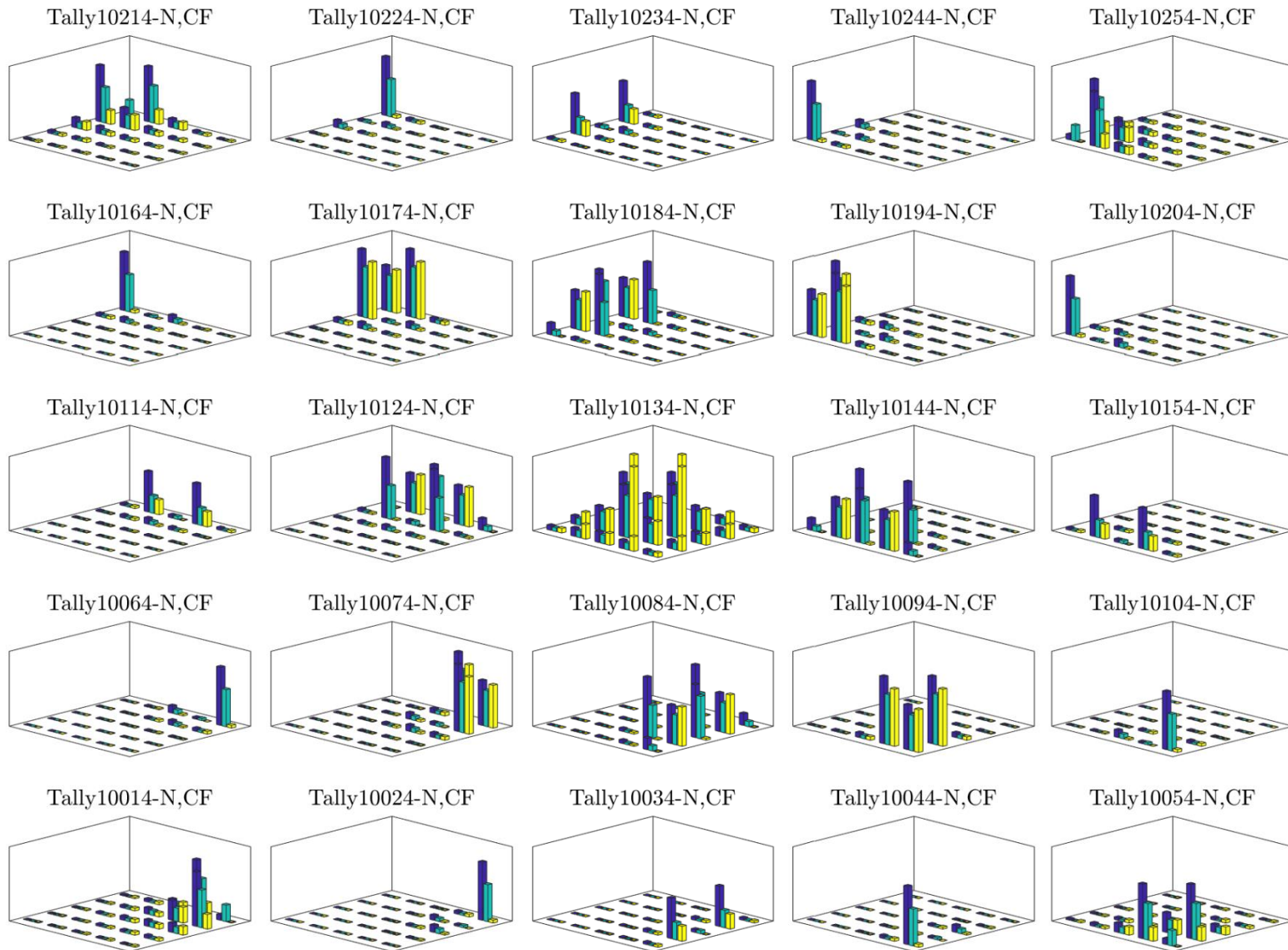
Fig. 39. Comparison of cross-talk contributions to average flux for packed, shielded, and staggered arrays for 14-MeV neutron beam focused on Cell 9
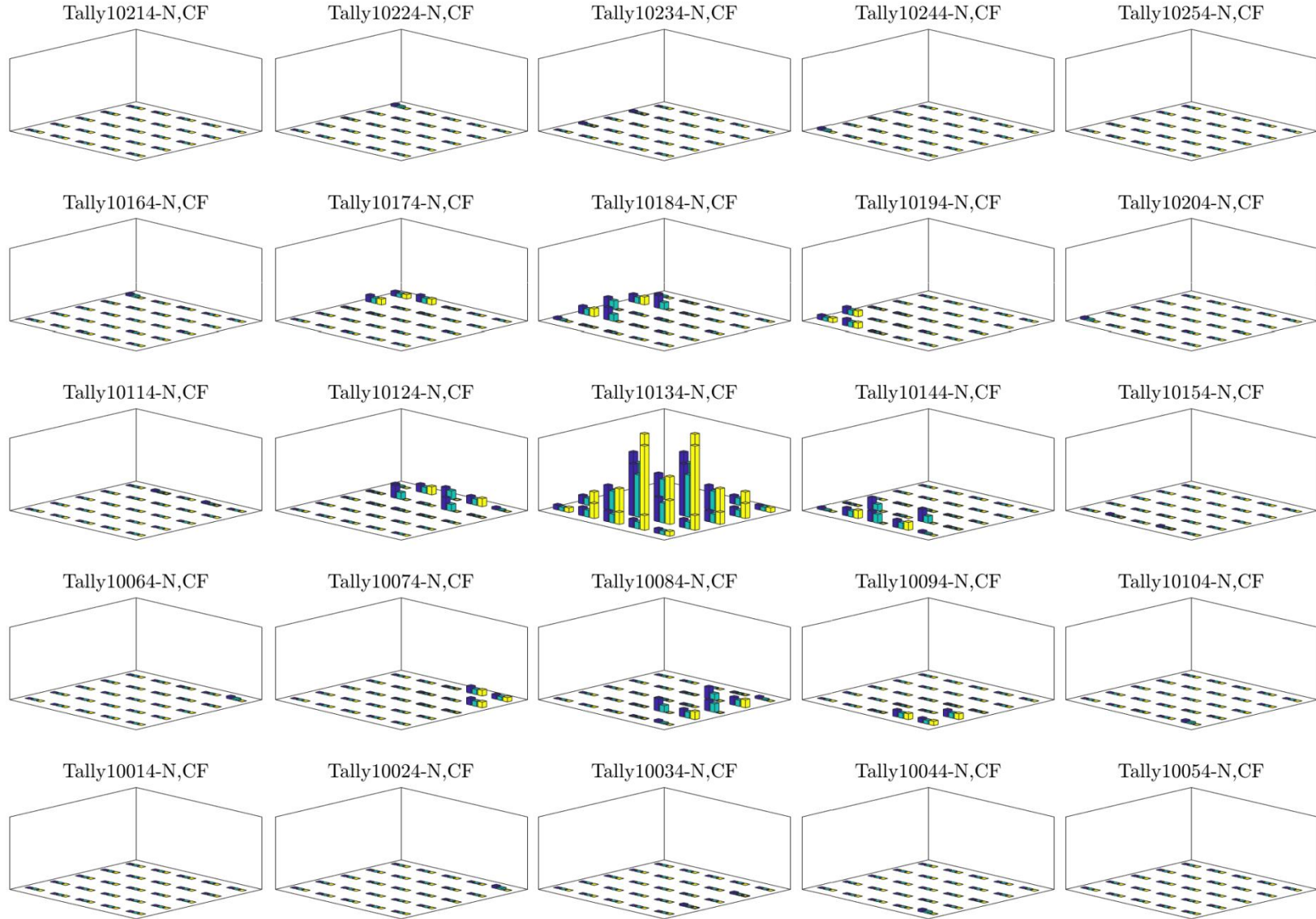
Fig. 40. Comparison of cross-talk contributions to average flux for packed, shielded, and staggered arrays for 14-MeV neutron beam focused on Cell 9

Imaging Applications

While current imaging technologies encompass fast neutron and dual photon techniques, the goal of this research was to study detector arrays capable of fast neutron detection. If the chosen scintillator is inherently capable of PSD, photon signatures can be discarded on-the-fly or d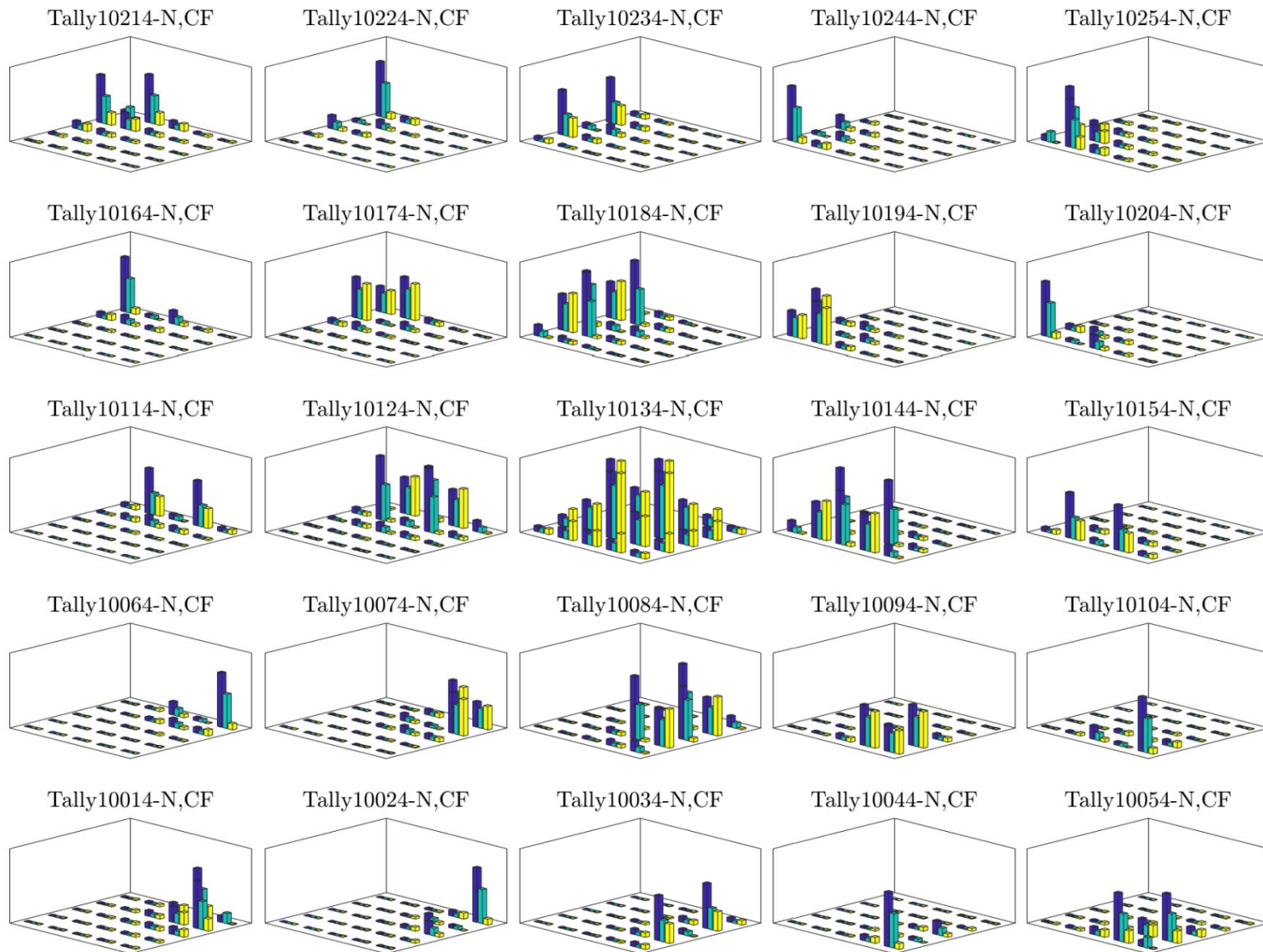uring post-processing, allowing just the fast neutron signatures to be used for imaging applications. To this end, additional computational studies were carried out to explore detector array applications in imaging technologies.

This was explored using the additional tallying options offered by the MCNP suite. While F4 tallies are preferred for determining the average flux per cell, MCNP5 offers the FIR, RMESH, and F5 tallies for the purpose of generating data sets representative of the responses a physical detector array would produce during experimental testing. The FIR tally was found to be ideal for this task, and was applied for use with the models considered here. Several computational studies have been carried out simulating the effectiveness of using detector arrays.

Computational Study 1 – Box Model with fan beam source [130]

The model for this study made use of a single, mono-energetic, isotropic point source to produce neutrons and photons with designated energies. 2D and 3D views of the simulation geometry are shown in Figs. 41a and 41b. An aluminum container filled with objects was placed between the point source and detector array. The point source was collimated to produce a 3cm wide fan beam of neutrons with energies of 2.5-MeV and 14-MeV. Using the FIR tally, the detector array for this model was defined with horizontal and vertical dimensions of 6 cm × 92 cm. This area was further divided into a 3 × 100 pixel grid, where each pixel had a surface area of 2 cm × 0.92 cm. To produce complete radiographic images of the container it was subjected to translational movement across the XY plane with transmission data being collected in twelve different "slices". A complete image of the container and its contents was then produced by combining together a set of slices. Additional data was generated for potential 3D reconstruction

applications by performing simulations where the container was rotated about the vertical z-axis between 0° and 180° using 5° increments.

(a)
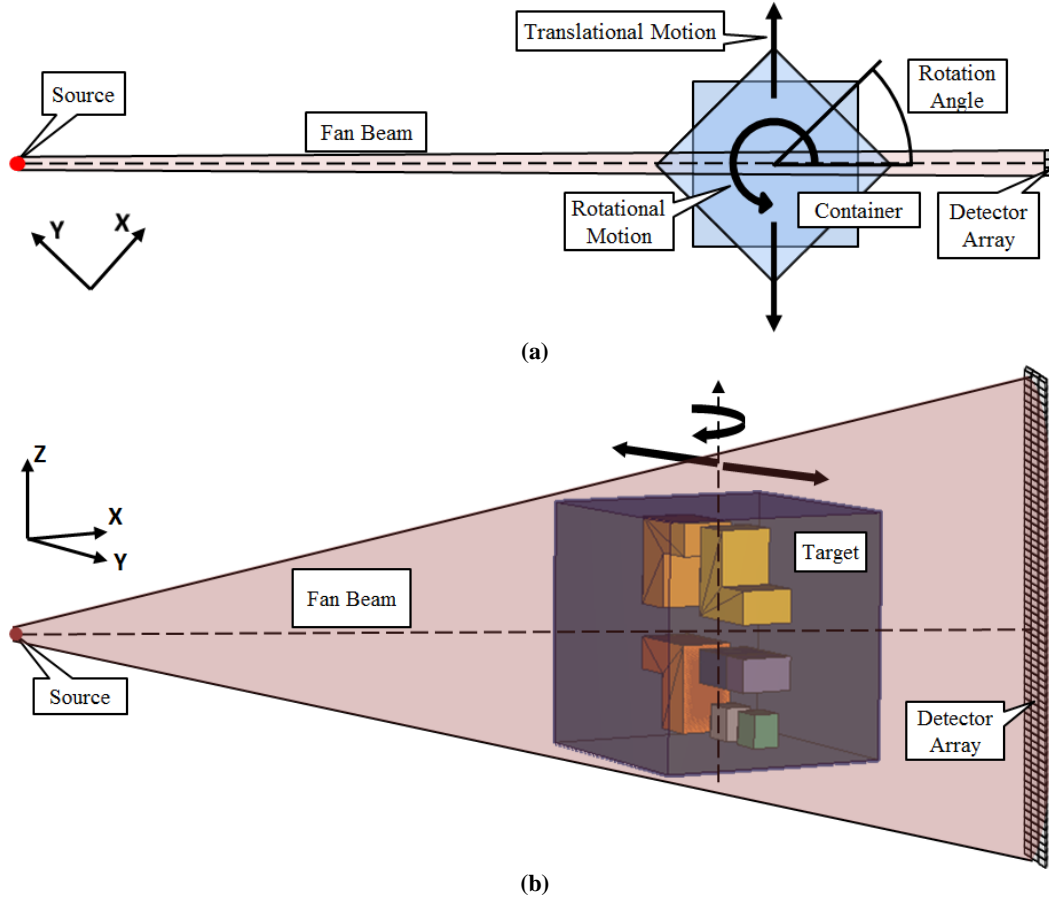
(b)
Fig. 41. (a) 2D and (b) 3D views of the fan beam system modeled in MCNP

The aluminum container was designed as a cube, with external dimensions of 50 cm × 50 cm × 50 cm and 3 cm thick walls. To demonstrate the effectiveness of the fan beam and detector array system, the container was filled with an assortment of parallelepipeds and L-shapes, as depicted in Fig. 41b. These objects were given the geometric arrangement shown in Fig. 42, where each body was assigned a unique set of properties summarized in Table 7. Three materials, iron, polyethylene, and lead were selected due to the variation in their Z-values. This difference made it possible to compare the radiographic transmission images produced by neutron sources to determine their effectiveness in imaging applications.
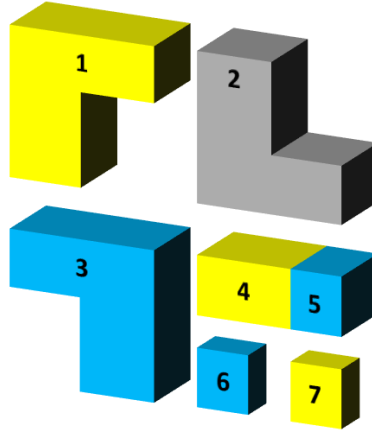
Fig. 42. Interior object dimensions for fan beam imaging

Table 7 – Dimensions of Items Included in Fan Beam Model

Interior Objects			
Number (Fig. 42)	**Object**	**Material**	**Dimensions (cm)**
1	L-shape	Polyethylene	$5(T) \times 8(W_2) \times 10(H_2) \times 16(W_1) \times 16(H_1)$
2	L-shape	Iron	$5(T) \times 8(W_2) \times 10(H_2) \times 16(W_1) \times 16(H_1)$
3	L-shape	Lead	$5(T) \times 8(W_2) \times 10(H_2) \times 16(W_1) \times 16(H_1)$
4	Parallelepiped	Polyethylene	$10(T) \times 6(W) \times 10(L)$
5	Parallelepiped	Lead	$10(T) \times 6(W) \times 6(L)$
6	Parallelepiped	Lead	$5(T) \times 6(W) \times 6(W)$
7	Parallelepiped	Polyethylene	$5(T) \times 6(W) \times 6(W)$

Several of the radiographic transmission images produced from these 2.5-MeV and 14-MeV neutron simulations are shown in Figs. 43a-c and 44a-c respectively. Transmission values for each pixel were reported per source particle as particles/cm^2. In both the 2.5-MeV and 14-MeV simulations the data showed that the detector array was capable of easily discriminating between the container and interior objects. Data from the 14-MeV set of simulations showed improved material discrimination when compared with the data from the 2.5-MeV simulations, even when rotating the model 150° about the vertical axis. Lower energy neutrons exhibited reduced transmission rates (only about 25% of incident neutrons reached the detector) when passing through the aluminum walls of the container compared with the neutron transmission rates for the 14-MeV neutrons (~50%). Similar trends were exhibited for each of the orientations when comparing neutron transmission through the hidden cells of polyethylene, iron, and lead. Although data from the 2.5-MeV neutron source could differentiate between individual cells and the

surrounding container, it was not sufficient by itself to indicate that the material of cells was different (Figs. 43a-c). Simulation data for 14-MeV neutrons demonstrated an improved stand-alone capability for potential object discrimination, producing visibly unique transmission values for different materials and thicknesses (Figs. 44a-c).
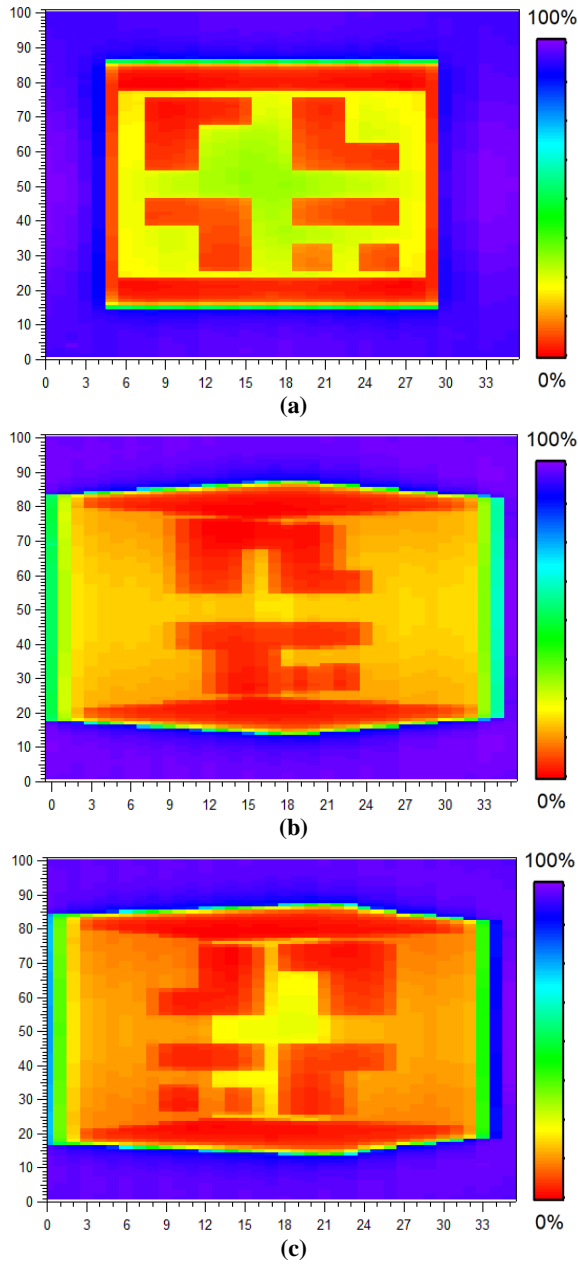
Fig. 43. Radiograph images from DD source for (a) 0°, (b) 50°, and (c) 150° orientations
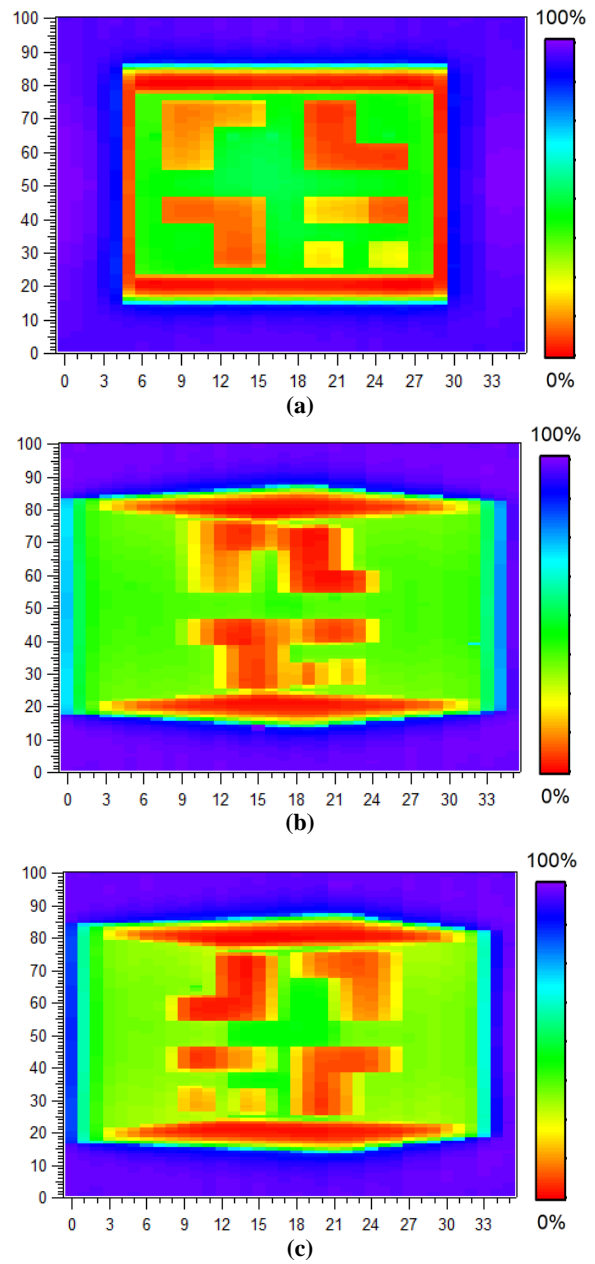
Fig. 44. Radiograph images from DT source for (a) 0°, (b) 50°, and (c) 150° orientations

Computational Study 2 – Box Model with cone beam [131]

Additional box model studies were done using a revised system set-up similar to that used in the fan-beam simulations. The collimator on the isotropic point source was modified so that the source would produce a cone beam of neutron radiation. The detector array was also expanded to include 10,000 unique points placed in a 100 pixel × 100 pixel grid, with each detector having a surface area of 0.92 cm × 0.92 cm. Since the detector array was widened to cover the full transmission area created by the source and container, the need for translational motion was negated. Instead, only rotational motion of the container was implemented in simulations studies. As indicated in Figs. 45 and 46, the container model was still rotated about its central vertical (z-axis). The container model was placed in the system such that the center of the container was 274cm away from the source, and 55cm from the detector array. 5° increments were used in rotating the container between 0° and 180° to produce a total of 36 unique radiographic transmission images.
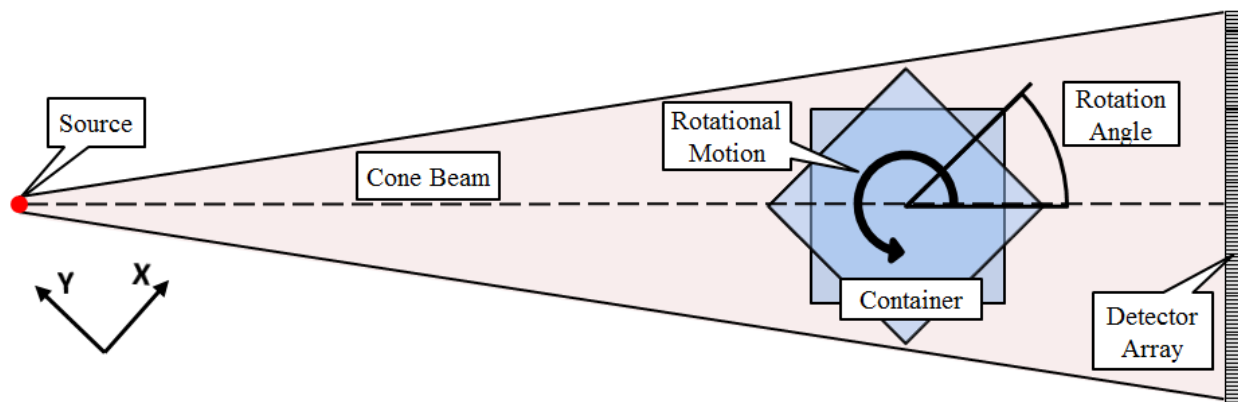
Fig. 45. Top view of imaging system using an isotropic, mono-energetic point source

As previously stated, the internal configuration of the container was modified to include more cells of varying materials and dimensions. The container properties remained consistent with the previous model, it was a cubic box made of aluminum with an external side length of 50 cm, and a wall thickness of 3 cm.
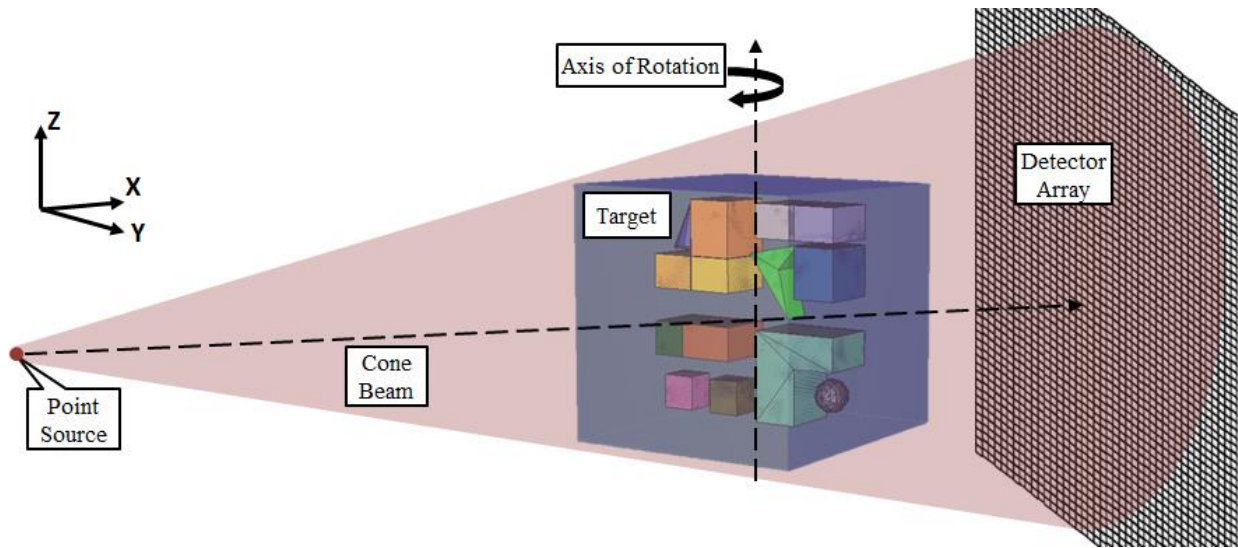
Fig. 46. Model set-up for imaging using an isotropic, mono-energetic point source

New materials including tungsten, copper, calcium, and salt were added to the model to provide a wider array of low-Z and high-Z options. A new geometric configuration was introduced as a conical and spherical bodies were added and two of the L-shapes were broken into smaller cells to produce the layout shown in Fig. 47. An additional irregular body was also included to test the resolution of the detector pixels when examining off-angle bodies with surfaces that cross multiple detector pixels. The material properties and dimensions of each included cell are summarized and recorded in Table 8.
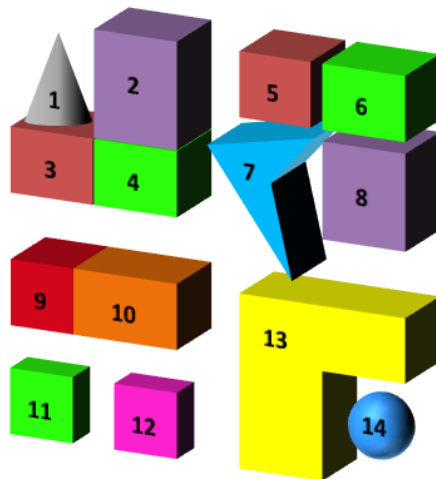
Fig. 47. Model set-up for imaging using an isotropic, mono-energetic point source

Table 8 – Dimensions of Items Included in Cone Beam Model

Aluminum Box			
Exterior Dimensions (cm)		**Wall Thickness (cm)**	
$50 \times 50 \times 50$		3	
Interior Objects			
Number (Fig. 47)	**Object**	**Material**	**Dimensions (cm)**
1	Cone	Iron	$8(H) \times 6(Dia)$
2	Parallelepiped	Tungsten	$10(T) \times 9.9(W) \times 8(L)$
3	Parallelepiped	Copper	$10(T) \times 6(W) \times 7.9(L)$
4	Parallelepiped	Calcium	$10(T) \times 6(W) \times 8(L)$
5	Parallelepiped	Copper	$10(T) \times 6(W) \times 7(L)$
6	Parallelepiped	Calcium	$10(T) \times 6(W) \times 8(L)$
7	Irregular Body	Lead	$10.1 \times 13.6 \times 8.7 \times 6$
8	Parallelepiped	Tungsten	$10(T) \times 9(W) \times 8(H)$
9	Parallelepiped	Graphite	$10(T) \times 6(W) \times 6(H)$
10	Parallelepiped	Boron	$10(T) \times 6(W) \times 10(H)$
11	Parallelepiped	Calcium	$5(T) \times 6(W) \times 6(H)$
12	Parallelepiped	Salt (NaCl)	$5(T) \times 6(W) \times 6(H)$
13	L-shape	Polyethylene	$10(T) \times 8(W_2) \times 10(H_2) \times 16(W_1) \times 16(H_1)$
14	Sphere	Water (H_2O)	$6 (Dia)$

The radiographic transmission images (Figs. 48a-c) produced from these simulations indicated that a 2.5-MeV neutron source may not be a high enough energy to penetrate through both the walls of the aluminum container and the increased number of hidden objects. Although there were still several spots which showed almost 100% transmission of incident source particles, these identified the external environment surrounding the box itself. The interior of the box, including the specific locations of the hidden cells showed less than 30% transmission. The exception to this was radiographic data for the 0° orientation (Fig. 48a) which exhibited general shapes and showed increased transmission in the very center of the box, where the center of the radiation cone would have been focused. Additionally it is possible to make out some slight definition of cells, although the transmission values are too similar to clearly define different materials for these cells. Figs. 48b and c were able to differentiate between the external environment, the walls of the container, and the interior but not much else. There were spots visible where the transmission values were near zero, but there was no clear definition or outline of the shapes which were responsible for the reduced transmission in this location.
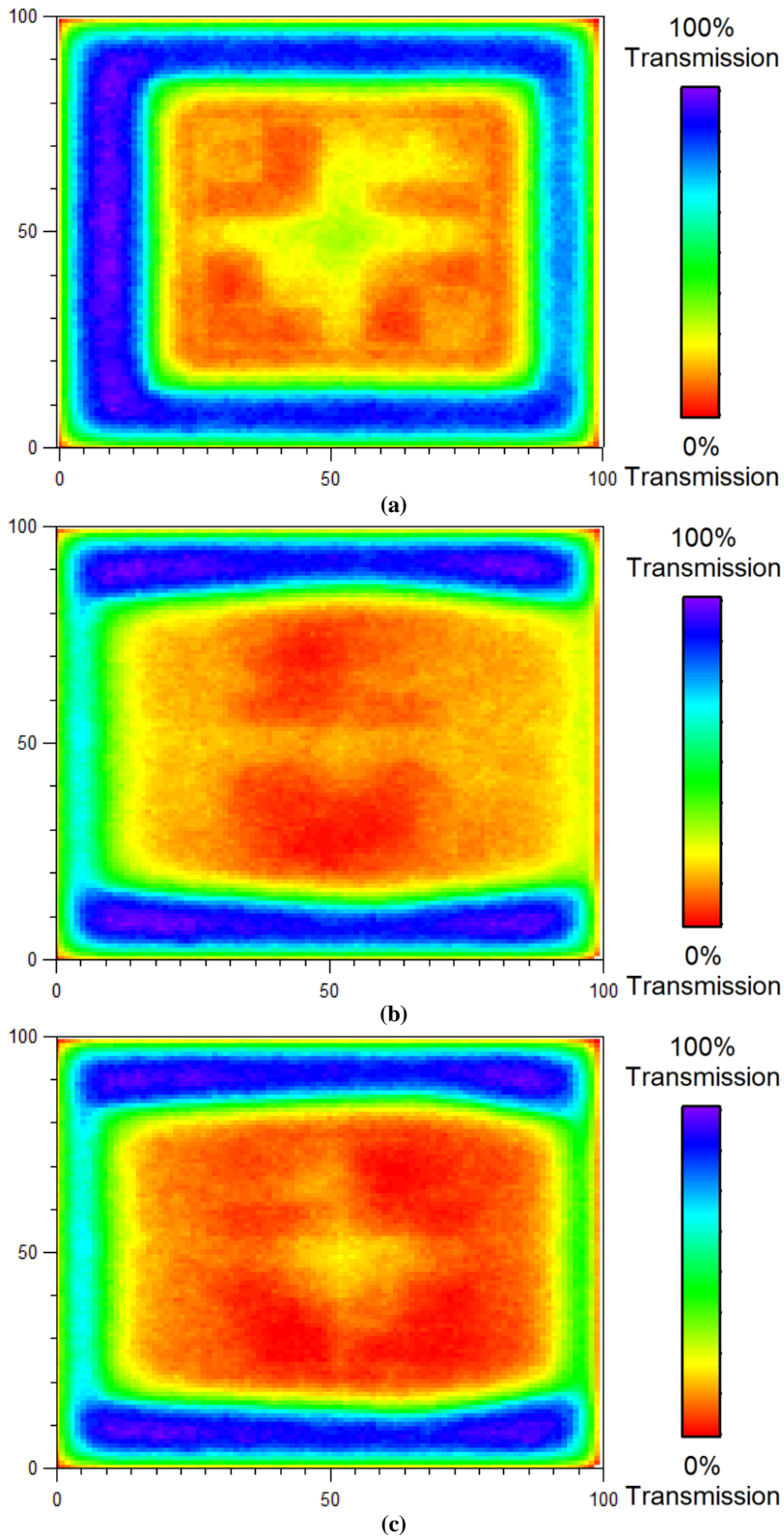
Fig. 48. Radiograph images from DD source at (a) 0°, (b) 50°, and (c) 150° orientations

Computational Study 3 – Engine Model [132]

With consideration for potential industrial applications, fast neutron imaging was studied for a simplified V6 engine. Fig. 49 depicts the 3D model used, with the source, target, and detector array. The source point was aligned with the center of the detector array, at a distance which allowed for radiographic image of the engine to be fully captured by the array. Simulations used an isotropic point source to generate neutrons with energies of 0.1-MeV, 0.5-MeV, and 2.5-MeV. The FIR tally was used to add a 100 cm × 100 cm array of point detectors and to subdivide the array into a 200 pixel × 200 pixel grid. This effectively gave each point detector (pixel) a surface area of 0.5 cm × 0.5 cm.
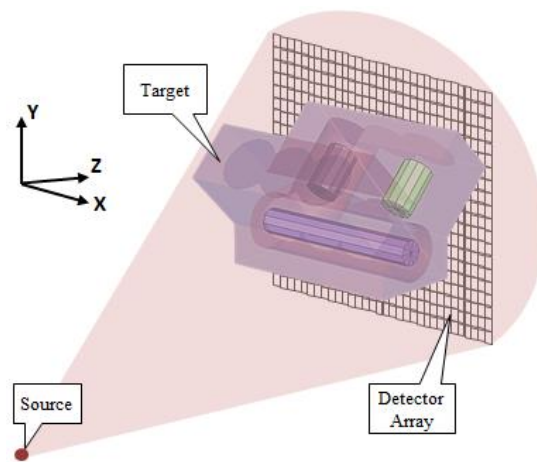
Fig. 49. 3D MCNP model of the imaging scenario

Figs. 50a and b show enlarged views of the engine, including hidden cells. Three aluminum blocks were assembled in a Y-shape to create the engine. One block served as the base, the other two were used to add the "arms" of the engine. A cylindrical void was added to the base with a diameter of 17.8 cm (D_B) and a length of 58 cm (L_B), and each arm was given 3 cylindrical voids with diameters and lengths of 18 cm and 29.9 cm respectively. The external height (H), width (W), and length (L) of the engine were 46 cm, 66 cm, and 60 cm respectively. Engine height was defined from the bottom of the base to the uppermost point of the arms, and the width was defined between the farthest corners of the arms (Fig. 50b).

60
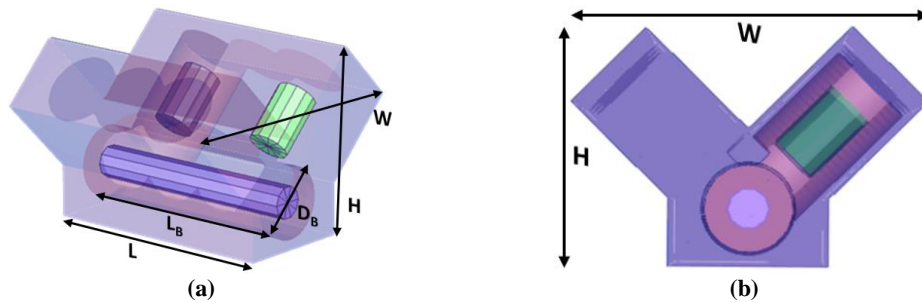
Fig. 50. Enlarged (a) 3D and (b) 2D view of engine body with dimensions

The engine was positioned within the model so that its central y-axis was 55 cm from the detector array and 274 cm from the source (Fig. 51). To generate different sets of radiographic transmission data, the engine block was rotated about the x-axis of the model (Figs. 52a and b). The point of rotation was defined as the center of the engine block, to allow for clear comparison of the data for the base and arms. To test the effectiveness of the detector array in discriminating between materials, the engine body was defined as aluminum, with additional cylinders of gasoline, polyethylene, and water were placed inside the voids as labeled in Fig. 53.
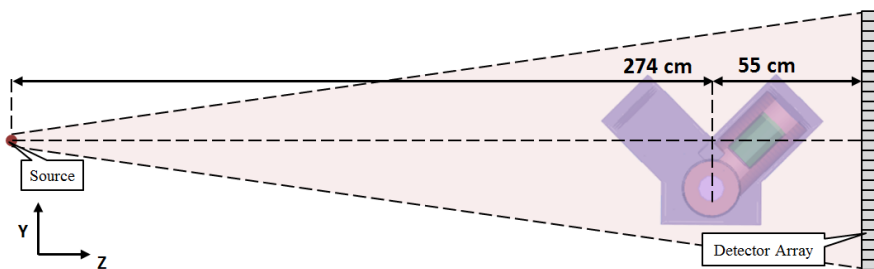
Fig. 51. 2D MCNP model of the imaging scenario

61

(a)

(b)
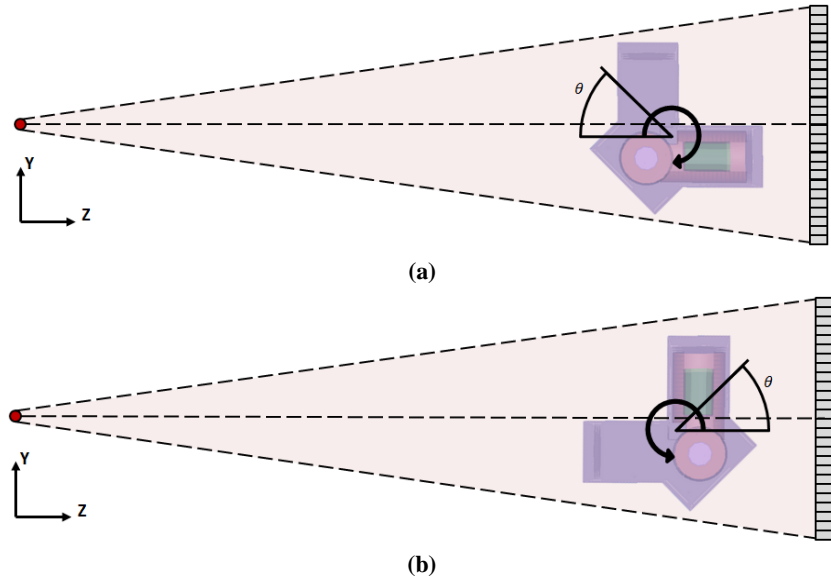
Fig. 52. Additional orientations used for imaging of (a) empty and (b) filled sections of the engine

(a)
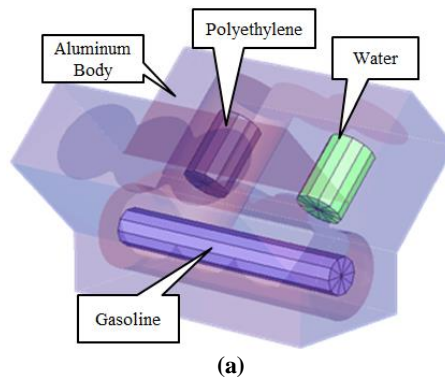
Fig. 53. Enlarged 3D view of engine body with materials

Several of the resulting radiographic images for this series of simulations are shown in Fig. 54. Generated for a 2.5-MeV neutron source, the color schemes in the figures are based on the transmission of source particles through the engine body to the detector array. The 2.5-MeV source energy was selected due to the popularity and availability of DD neutron generators. The values reported by the FIR tally used units of particles/cm^2 with respect to source, with 100% transmission indicating no material present between the source and the detector. Similarly, 0% transmission indicated that the material between the source and the detector array was thick enough to stop and absorb all or at least the majority of incident source particles.

Using the transmission values for each simulation, it was possible to generate the different views shown in Figs. 54a-c. There are obvious differences visible in the transmission between the different rotations of the model. Looking at the side-view of the engine (Fig. 54a), the aluminum body of the engine proves too thick for quick or easy identification of any hidden materials. Despite this, it is still possible to identify the thinnest portions of the engine walls, as seen at this angle, by locating the green and yellow portions. These portions identify where the voids of the base and arms overlap, leaving less material between the source and detector array. It is possible to identify the central void the engine arm which was not filled with an additional material cell. There are also vague outlines in the right and left voids of the arm, where the polyethylene and water cells do not fully fill their respective voids.

Figs. 54b and c offer clearer images of the interior of the engine due to the rotation of the model. Fig. 54b shows a clear view of the empty arm of the engine. For this data set, the model was oriented with the empty arm of the engine parallel to the detector array, and the filled arm perpendicular to the detector array as was depicted in Fig. 52a. The results here showed good distinction between the voids of the arm, with nearly 100% transmission of source particles through the center of the arm voids. The increased TRs correctly indicated that the aluminum walls were thinnest at these points. Focusing on the overlap of the base and filled arm in this result, it was also possible to make out the outline of the gasoline cylinder, as well as the location of the water and polyethylene cells. The gasoline shows up as a darker orange bar which crosses all three of the voids in the arm facing the source, while the polyethylene and water cells appear as darker red circles within their respective voids.

Fig. 54c shows a clear view of the filled arm of the engine. For this data set, the model was oriented with the filled arm of the engine parallel to the detector array, and the empty arm perpendicular to the detector array as was depicted in Fig. 52b. The results here showed improved distinction between the voids of the arm, with nearly 100% transmission of source particles through the empty central void of the parallel arm. The transmission values in the neighboring voids were visibly reduced where the extra cells were located. The polyethylene exhibited lower transmission values (orange) compared with the greater transmission values of the water (yellow). Focusing on the overlap of the base and perpendicular arm in this result, it

was also easier to note the outline of the gasoline cylinder against the aluminum body of the engine and the voids in the arm facing the source.
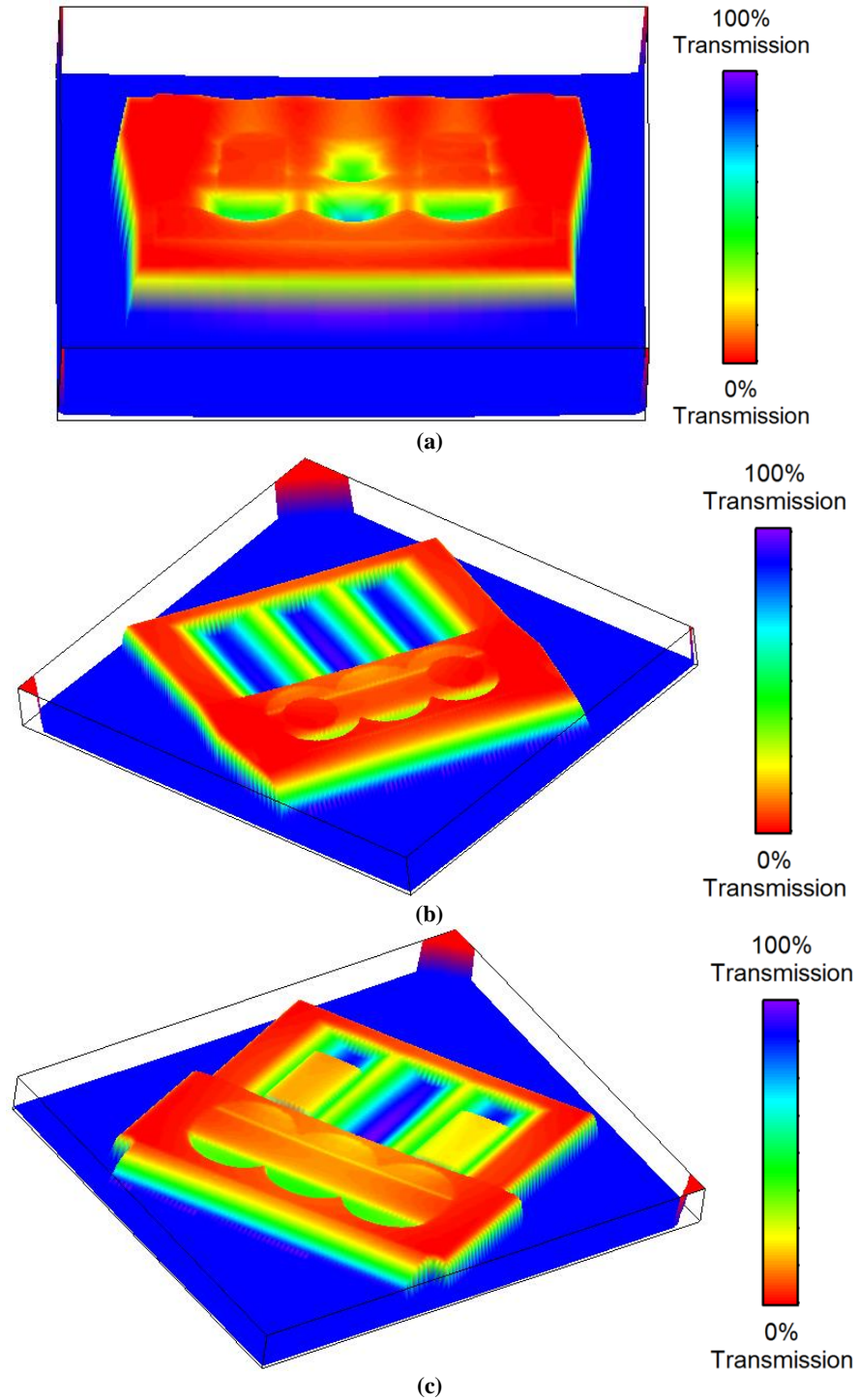
Fig. 54. 2.5-MeV neutron images of engine (a) side-view, (b) empty arm, and (c) filled arm

One of the key challenges facing detector array applications is the occurrence of cross-talk between pixels. Incident particles and electromagnetic waves rarely deposit all of their energy during the first interaction, which can lead to a single incident particle or wave generating multiple scintillation events across several cells. To study this effect and potential solutions for it packed, shielded, and staggered array designs were modeled using MCNP6. The results of these simulations indicated that it was possible to reduce gamma-ray cross-talk between cells by adding shielding material between the individual scintillation cells, or by modifying the layout so neighboring cells were not in direct contact with one another. In both cases the reduction in cross-talk was not sufficient enough to justify the solution. For the shielded array, not only did the extra material increase the weight of the detector array, it added dead space between each pixel where incident particles were undetectable. The staggered array model eliminated this dead space and the additional weight due to shielding, but doubled detector array depth. This increase was negligible for shallow scintillator cells, but arrays quickly become cumbersome and difficult to transport as cell depth is increased. Due to the unavoidable occurrence of cross-talk, and the impractical nature of shielding or staggering detector cells, it would be preferable to exploit cross-talk information to reconstruct an incident particle's trajectory through several pixels and identify the point of entry into the detector array.

By employing fast neutron detectors arrays using PSD capable scintillators, it is possible to use a single array for dual-radiation imaging tasks. Whether present as background radiation, or created as secondary charged particles from neutron interactions, photon signatures are always present. When employing PSD enabled materials for fast neutron detector arrays, it is possible to isolate the photon components of a measurement or image. Once isolated, this response component can either be preserved and analyzed for additional information or discarded. Simulations were developed for fan and cone beam based imaging systems using a standard unit load device and a simplified V6 engine block. In each simulation several objects were hidden within the target object, each with different material properties and dimensions. Source radiations and energies were defined using standard combinations that could be replicated with DD and DT generators.

CHAPTER 5 – EXPERIMENTAL STUDY

EJ-299-33A Experiments

The final objective of this research focused on experimental study of the plastic scintillator, EJ-299-33A

for fast neutron detector array. The available sample was a square cube of transparent plastic, shown in

(Fig. 55). Manufactured with inherent PSD capabilities, five of the cube's surfaces were wrapped in white

Teflon tape, leaving only one face exposed for detection applications. Prior to testing, black electrical tape

was wrapped around the covered surfaces to reduce light leakage.
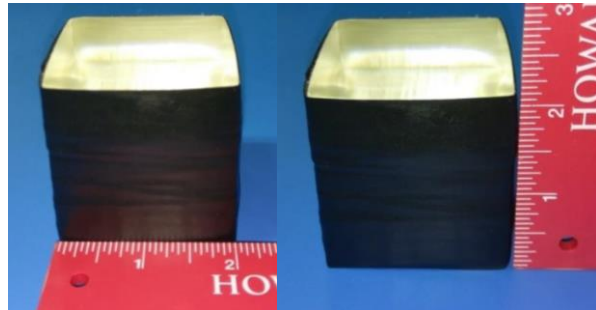
Fig. 55. Plastic scintillator used for experimental verification

The scintillator was coupled to a Hamamatsu R6231 PMT (Figs. 56) using optical grease. This PMT

possessed a 2 in diameter, but the effective area of the exposed face had a 1.8 in diameter. The PMT was

wrapped in black electrical tape prior to testing as a precaution against light leakage.
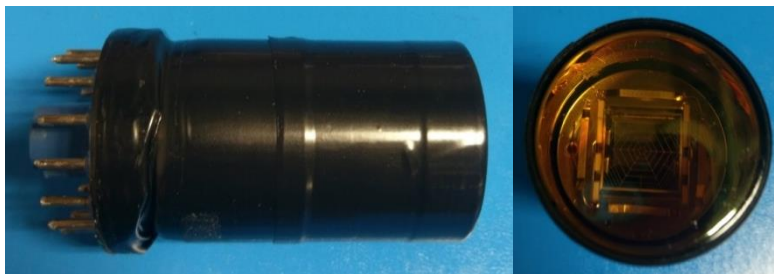
Fig. 56. Hamamatsu PMT used for PSD testing

The plastic scintillator and PMT were wrapped with more electrical tape both to secure the pieces together and to provide an additional barrier against light leakage during measurements. A high voltage base was added to connect the PMT to an eMorpho unit from Bridgeport Instruments (Fig. 57). This unit was used to collect and transmit data to a user terminal where measurements were reported and analyzed.

Fig. 57. Detector assembly for PSD testing of EJ-299-33A

After verifying the electronics and scintillator in photon fluxes, the PSD capabilities of the EJ-299-33A plastic scintillator were tested using the mixed neutron/photon fluxes produced by a 2 Ci PuBe source. The experimental arrangement for these measurements is shown in Fig. 58. The source is kept in a 55-gallon, steel drum filled with paraffin wax. A horizontal beam port was designed into the unit which extends from the center of the drum to the external environment. In order to perform the measurements, the PuBe source was raised so that it sat in line with the beam port, and the detector face was placed at the same level as the beam port. Measurement data was collected for 250 buffers, recording a total of 85,000 scintillation events (340 events per buffer).

Fig. 58. Detector set-up for PuBe measurements

Results for PSD analysis of a PuBe measurement are shown in Fig. 59, with energy values which were calibrated using known Co^{60} and Cs^{137} sources. For this data, the scintillation events have already been assigned PID values by the software, using Eqn. 3 (Chapter 2, pg. 17). Each data point in the figure identifies a single scintillation event observed by the attached PMT. A quick visual inspection allowed for discrimination between the neutron (red) and photon (black) arms. Using the point on the vertical axis where the arms appear to separate (PID = 1.05), neutron waveforms were defined as having PID values greater than this, while those below the limit were identified as photons.
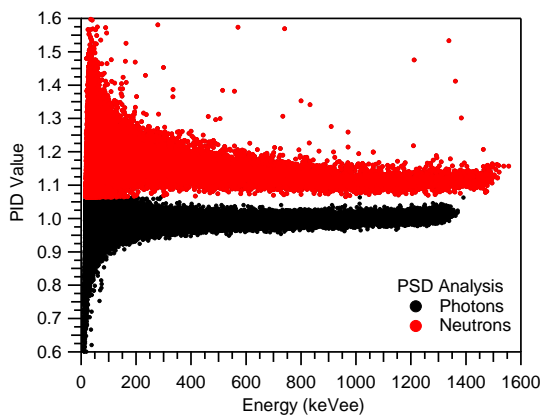
Fig. 59. PSD data from PuBe response measurement

Quantitative analysis of the detector's PSD capability was done by calculating the Figure of Merit (FOM) using a PID graph, where counts are plotted against PID values. Depending on the radiation source, these plots will show one or more peaks as Figs. 60a and b show. Fig. 60a is a plot of the measured Counts vs. PID data for photon source. In this case there is only a single finger present because only photons were produced by the source and seen by the scintillator and PMT. In contrast, Fig. 60b shows a similar data set, this time measured in the mixed neutron/photon flux of the PuBe source. Since the detector was subjected to neutrons and photons, both radiations were detected, creating two unique fingers on the plot. The taller, narrower peak with the lower PID range (0.05-0.2) is caused by the detected photons, while the shorter, wider peak with the higher PID range (0.2-0.4) is due to the neutrons detected.
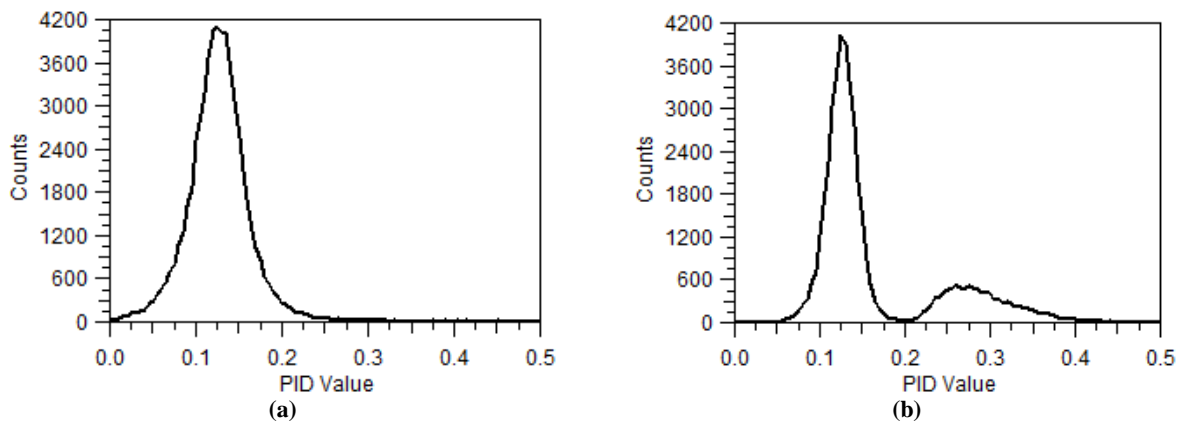
Fig. 60. PID plots for (a) photon flux and (b) mixed neutron/photon flux

The goal of calculating the FOM is to determine a detector's suitability for PSD analysis, it is generally applied only to measurements where more than one radiation type is detected. In this instance, the plot in Fig. 60b was used to determine the FOM for the scintillator detector. An FOM calculation is simply the ratio of the peak separation to summation of the peak widths using the formula and variables identified in Fig. 61. The first variable, the peak separation (T), was calculated as the horizontal difference between the peak values of each finger. The remaining values were the widths of the photon (W_P) and neutron (W_N) peaks. These values were defined at the point of the Full Width Half Maximum (FWHM) for their respective peaks. Applying these values to the formula an FOM value of 2.08 was calculated.
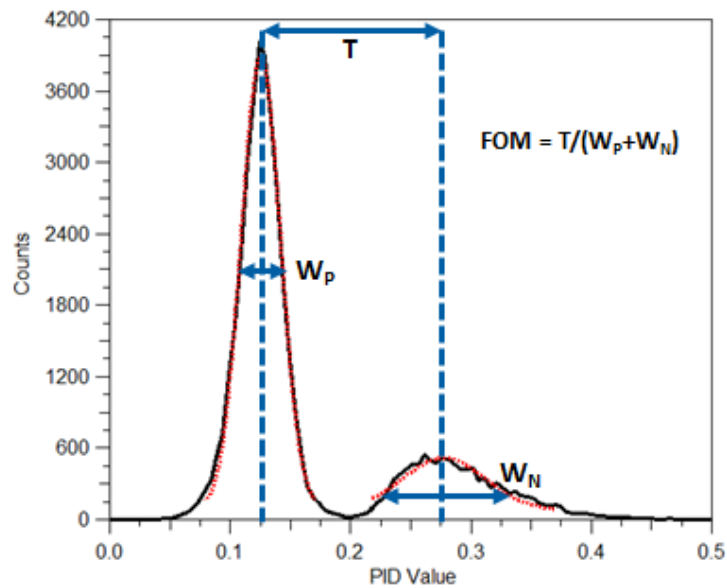
Fig. 61. PSD data from PuBe response measurement

Extensive experimental work was also performed for the EJ-299-33A plastic scintillator [54]. Using the Van de Graaff accelerator at the University of Kentucky Accelerator Laboratory, response functions for this particular scintillator were measured for incident neutrons with tuned energies from 0.1-MeV to 8.2-MeV and from 12.2-MeV to 20.2-MeV. Part of this work focused on the development of a PSD post-processing code designed specifically to divide recorded response functions into their respective photon and neutron components, and carrying out spectral unfolding techniques.

CHAPTER 6 – CONCLUSIONS & FUTURE WORK

Conclusions

The main objective of this research was achieved. A variety of scintillator materials and compositions were compared to determine their efficiency and potential application as fast neutron detection components. In particular, the feasibility of the plastic scintillator EJ-299-33A, and the crystal scintillators CLLB and CLYC were the subject of numerous studies. Simulations were developed and tested for both homogeneous and heterogeneous cells of these materials. Although CLLB and CLYC showed reasonable resolution and efficiency when applied for neutron detection, their fragile crystalline state made them less than desirable, the additional financial and time costs related to growing large crystals was another prohibitive factor against their use in neutron detector arrays. Moreover, characteristic scintillation time of the neutron component for crystal scintillators is much slower than that of plastic scintillators. The EJ-299-33A scintillator was demonstrated to have reasonable PSD capabilities making it a good candidate for fast neutron detector arrays. Additionally the durable plastic nature of this scintillator makes it possible to mass produce a variety of shapes and sizes without incurring the extreme costs of crystalline scintillators.

Additional simulations were done to study detector arrays using a 5 pixel × 5 pixel design and an incident neutron beam. In particular, these simulations focused on the occurrence and impact of cross-talk between the unique scintillator cells in a single array. Models were developed and tested for packed, shielded, and staggered detector arrays, with the cross-talk in each of these models being compared. While the shielded and staggered models did show a slight reduction of gamma-ray cross-talk between cells, it was not significant enough to justify the extra weight and bulkier dimensions caused by these models. Additional imaging simulations were performed for cargo and an engine block using isotropic neutron point sources with energies of 2.5-MeV and 14-MeV. The goal of these simulations was to identify the potential of

employing neutron imaging systems composed of detector arrays and either DD or DT generators. Results indicated that it was possible to use either neutron source in imaging.

The final part of this research involved testing the PSD capabilities of an EJ-299-33A plastic scintillator cell. The scintillator detector was tested using photon sources, and its PSD capabilities were investigated using mixed neutron/photon fluxes from a PuBe source. Analysis of measurement data reported the FOM of a neutron/photon PSD as 2.08, making EJ-299-33A suitable for fast neutron measurements.

Future Work

The next phase for this research is the assembly of a multi-pixel fast neutron detector for testing in neutron or neutron/photon fluxes. This phase poses several challenges, the greatest of which is the need for development of the electronics and hardware necessary to process data from a detector array. SiPM boards are already commercially available, complete with Si avalanche photodiode arrays which make their use in directional and imaging related tasks possible. Fig. 62 shows one of these boards, produced by SensL, which possesses an 8×8 array of Si avalanche photodiode arrays for a total of 64 pixels. Each Si avalanche photodiode pixel measures 7 mm × 7 mm, with a reported active area of 6 mm × 6 mm, is capable of optical readout of scintillation emissions of the plastic EJ-299-33A.
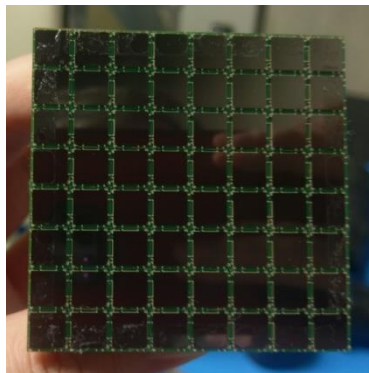
Fig. 62. Sensel SiPM board with 8×8 array

Testing of this arrangement could be done by optically coupling a scintillator cell to the SiPM board and ensuring the SiPM board and scintillator cell are properly wrapped to prevent light leakage from interfering with measurements. It is possible to use SiPM for signal processing of plastic scintillator emissions and neutron/photon PSD, but further development of microelectronics for multiplexing and data analysis is required before this could be exploited for measurements.

Testing of the fast neutron detector array would also require the acquisition and use of multiple scintillator cells. Although a solid scintillator cell can be used to fully cover the SiPM, and jumper cables used to read the output of a single pixel, a single cell should be optically coupled to each SiPM pixel. These cells should also be wrapped or coated with an opaque material to prevent light leakage and keep the scintillators optically separated from one another.

A final task for consideration would be the development of a reconstruction technique capable of utilizing cross-talk between pixels to locate the entry point of a given particle or electromagnetic wave. Since the elimination of cross-talk between pixels is impractical and available options to reduce it are unsuitable, being able to utilize this information to locate where radiation initially entered the array would make detector arrays more efficient.

NEUTRON/GAMMA PSD PLASTIC SCINTILATOR
EJ-299-33A, EJ-299-34

EJ-299-33A pulse-shape discriminating (PSD) plastic scintillator enables the separation of gamma and fast neutron signals on the basis of their timing characteristics using conventional PSD electronics systems. Cylinders up 127 mm diameter x 127 mm long can be supplied.

EJ-299-34 was developed as an alternative to EJ-299-33A. Although EJ-299-33A has the appearance and feel of a standard plastic scintillator, it is somewhat softer and therefore more difficult to machine and polish. While its PSD properties are slightly poorer than those of EJ-299-33A, EJ-299-34 is a harder plastic

that is more easily machined and polished to high tolerances. It can be cast in sheet form primarily for the manufacture of small precision rectangular bars in the making of imaging arrays. To date, sheets up to 15 mm x 250 mm x 250 mm have been cast in large numbers and with good product uniformity.

At this time, EJ-299-33A and EJ-299-34 are both still under development. These products are sold under license from Lawrence Livermore National Laboratory.

PROPERTIES	EJ-299-33A EJ-299-34
Light Output (% Anthracene)	56
Scintillation Efficiency (photons/1 MeV e⁻)	8,600
Wavelength of Maximum Emission (nm)	420
H Atoms per cm³ ($\times 10^{22}$)	4.36
C Atoms per cm³ ($\times 10^{22}$)	4.84
Electrons per cm³ ($\times 10^{23}$)	3.46
Density (g/cm³)	1.08
Approx. Mean Decay Times of First 3 Components (ns)	
Gamma Excitation	13, 35, 270
Neutron Excitation	13, 50, 460

CHEMICAL COMPATIBILITY

Attacked By: Aromatic solvents, Chlorinated solvents, Ketones, Solvent bonding cements, etc.
Stable In: Water, Dilute acids and alkalis, Lower alcohols, Silicone greases.
It is safe to use most epoxies with these scintillators.

MAXIMUM SIZES	
EJ-299-33A	127 mm dia. × 127 mm Rod
EJ-299-34	15 mm x 250mm x 250mm Plate

EJ-299-33A AND EJ-299-34 EMISSION SPECTRUM

PSD SCATTER CHART, AmBe
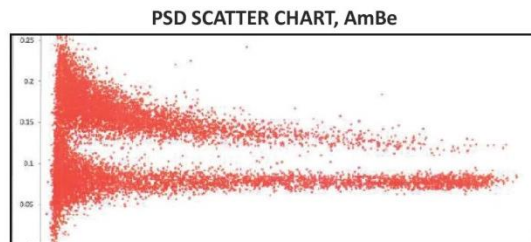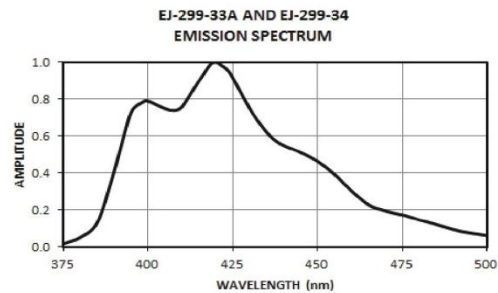
SCINTILLATOR SIZE: 127 mm DIA × 51 mm THICK

Revision Date: 9/8/2016

PSD PLASTIC SCINTILATOR
EJ-276 & EJ-276G

EJ-276 pulse-shape discriminating (PSD) plastic scintillator enables the separation of gamma and fast neutron signals on the basis of their timing characteristics. This scintillator replaces all versions of EJ-299-33 and EJ-299-34 PSD scintillators and embodies the following improvements:

- Excellent physical hardness, equal to or superior to that of standard plastic scintillators
- Long-term stability of scintillation and optical characteristics
- Basic PSD properties increased to being comparable to the best liquid scintillators

EJ-276G with green fluorescence is also available for use with solid state sensors.
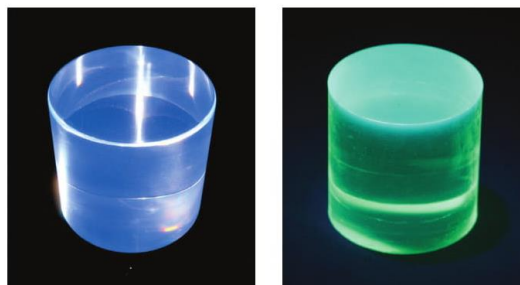
PROPERTIES		EJ-276	EJ-276G
Light Output (% Anthracene)		56	52
Scintillation Efficiency (photons/1 MeV e⁻)		8,600	8,000
Wavelength of Maximum Emission (nm)		425	490
H Atoms per cm³ ($\times 10^{22}$)		4.53	4.53
C Atoms per cm³ ($\times 10^{22}$)		4.89	4.89
Electrons per cm³ ($\times 10^{23}$)		3.52	3.52
Density (g/cm³)		1.096	1.096
Approx. Mean Decay Times of First 3 Components (ns)	**Gamma Excitation**	13, 35, 270	—
	Neutron Excitation	13, 59, 460	—

CHEMICAL COMPATIBILITY

Attacked By: Aromatic solvents, Chlorinated solvents, Ketones, Solvent bonding cements, etc.
Stable In: Water, Dilute acids and alkalis, Lower alcohols, Silicone greases.
It is safe to use most epoxies with this scintillator.

Available Sizes

Cylinders up to 127 mm diameter x 200 mm long and plates up to 25 mm thick x 250 mm x 250 mm can be supplied. Precision imaging arrays with square pixels with cross sections as small as 0.75 mm can also be supplied.

PSD SCATTER CHART, AmBe
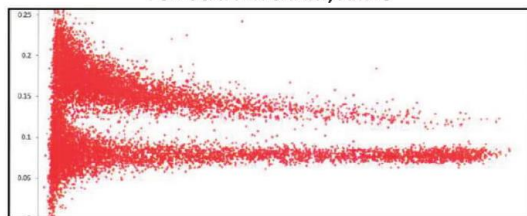
SCINTILLATOR SIZE: 127 mm DIA × 51 mm THICK

EJ-276 & EJ-276G EMISSION SPECTRUM
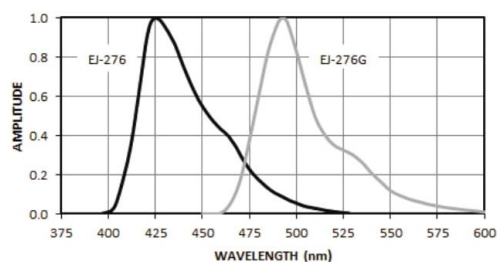
Revision Date: October 2017

NEUTRON/GAMMA PSD LIQUID SCINTILLATOR
EJ-301, EJ-309

EJ-301 exhibits excellent pulse shape discrimination (PSD) properties, particularly for fast neutron counting and spectrometry in the presence of gamma radiation. It is identical to the widely reported NE-213 and exhibits all of the properties of that scintillator.

EJ-309 has been developed as an alternate to the more commonly used low-flash point PSD liquid scintillators based on the solvent xylene. With a flash point of 144°C, it eliminates the fire hazard associated with low-flash point liquid scintillators. While EJ-309 provides slightly poorer PSD characteristics than that of EJ-301, EJ-309 possesses a number of chemical properties recommending it for use in environmentally difficult conditions. These properties include: high flash point, low vapor pressure, low chemical toxicity, and compatibility with cast acrylic plastics. EJ-309 is also available loaded with natural boron as EJ-309B.
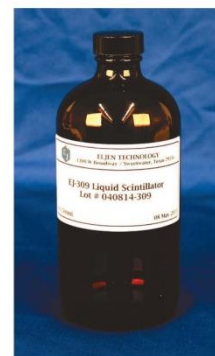
PROPERTIES	EJ-301	EJ-309
Light Output (% Anthracene)	78	80
Scintillation Efficiency (photons/1 MeV e-)	12,000	12,300
Wavelength of Maximum Emission (nm)	425	424
Decay Time, Short Component (ns)	3.2	3.5
Mean Decay Times of First 3 Components (ns)	3.16 32.3 270	-
Bulk Light Attenuation Length (m)	2.5 - 3	> 1
Specific Gravity	0.874	0.959
Refractive Index	1.505	1.57
Flash Point (°C)	26	144
Boiling Point (°C at 1 atm)	141	290 - 300
Vapor Pressure (mm Hg, at 20°C)	-	0.002
H Atoms per cm³ ($\times 10^{22}$)	4.82	5.43
C Atoms per cm³ ($\times 10^{22}$)	3.98	4.35
Electrons per cm³ ($\times 10^{23}$)	2.27	3.16
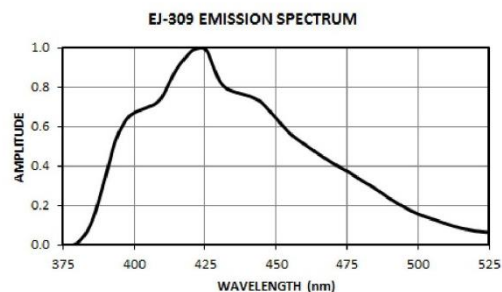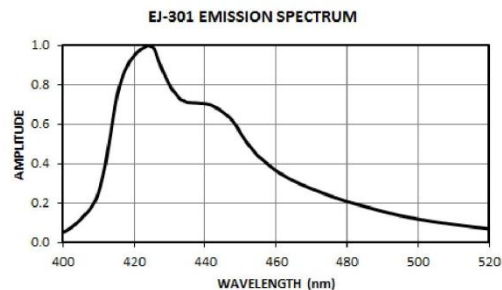
EJ-301 EMISSION SPECTRUM

EJ-309 EMISSION SPECTRUM

Revision Date: 02/11/2016

BORON LOADED LIQUID SCINTILLATOR
EJ-309B

EJ-309B is a variant of EJ-309 loaded with natural boron. Loadings up to 5% by weight of natural boron are available. EJ-309B has most of the same general properties as EJ-309. The atomic compositions of three different loading levels are given below.

EJ-309B EMISSION SPECTRUM
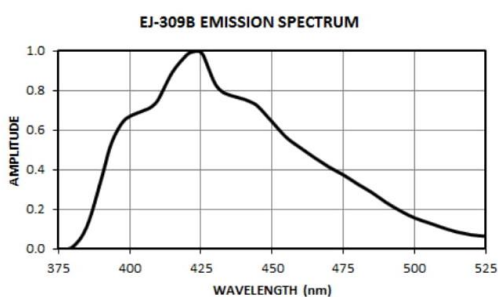
PROPERTIES	EJ-309B (% boron)		
	-5%	-2.5%	-1%
Natural Boron Content (% w/w)	5	2.5	1
Light Output (% Anthracene)	57	64	69
Scintillation Efficiency (photons/1 MeV e-)	8,800	9,800	10,600
Wavelength of Maximum Emission (nm)	424	424	424
Decay Time, Short Component (ns)	3.5	3.5	3.5
Bulk Light Attenuation Length (m)	> 1	> 1	> 1
Specific Gravity	0.963	0.964	0.965
Refractive Index	1.57	1.57	1.57
Flash Point (°C)	144	144	144
Boiling Point (°C at 1 atm)	290 - 300	290 - 300	290 - 300
Vapor Pressure (mm Hg, at 20°C)	0.002	0.002	0.002
H Atoms per cm³ ($\times 10^{22}$)	5.40	5.43	5.44
C Atoms per cm³ ($\times 10^{22}$)	4.13	4.25	4.33
^{10}B Atoms per cm³ ($\times 10^{20}$)	5.34	2.68	1.07
Electrons per cm³ ($\times 10^{23}$)	3.16	3.17	3.17
^{10}B/H Ratio of Linear Attenuation Coefficient for Thermal Neutron Capture	125	62.4	25.1

REFERENCES

[1]   C. Meade and R. C. Molander, "Considering the Effects of a Catastrophic Terrorist Attack," 2006.

[2]   B. Rep. Thompson, *H.R.1 - Implementing Recommendations of the 9/11 Commission Act of 2007*. House of Representatives, 2007.

[3]   B. Kempinski and C. Murphy, "Scanning and Imaging Shipping Containers Overseas: Costs and Alternatives," 2016.

[4]   "Coping with tough air-cargo inspection requirements," *Homeland Security News Wire*, 14-Jan-2011.

[5]   SEARATES.com, "Parameters of Sea Containers." [Online]. Available: https://www.searates.com/reference/equipment/. [Accessed: 11-Oct-2017].

[6]   Port Performance Working Group, "Port Performance Freight Statistics Program: Annual Report to Congress 2016," Washington, DC, 2017.

[7]   SEARATES.com, "40' Standard Container." [Online]. Available: https://www.searates.com/reference/equipment/2. [Accessed: 11-Oct-2017].

[8]   "On a Typical Day in Fiscal Year 2016, CBP...," 13-Feb-2017. [Online]. Available: https://www.cbp.gov/newsroom/stats/typical-day-fy2016. [Accessed: 11-Oct-2017].

[9]   B. Sutherland, "My Blackberry As A Bomb Sniffer?: Expensive radiation detectors may not be as effective as widely distributed chips in cell phones. - ProQuest," *Newsweek*, Oct-2008.

[10]   "Model 52 Personnel Beta/Gamma Portal Monitor." Ludlum Measurements, Inc., 2016.

[11]   "LMI Price List," 2017. [Online]. Available: http://metals.ludlums.com/store/price-lists. [Accessed: 12-Oct-2017].

[12]   "Model 53 Personnel Gamma Portal Monitor." Ludlum Measurements, Inc., 2015.

[13]   G. R. Hopkinson, T. M. Goodman, and S. R. Prince, "Detector Arrays," in *A Guide to the Use and Calibration of Detector Array Equipment*, Bellingham, Washington: SPIE—The International Society for Optical Engineering, 2004, pp. 1–51.

[14]   J. Chadwick, "Possible Existence of a Neutron," *Nature*, vol. 129, pp. 312–312, Feb. 1932.

[15]   F. D. Brooks, "Development of organic scintillators," *Nucl. Instruments Methods*, vol. 162, no. 1–3, pp. 477–505, Jun. 1979.

[16]   J. Iwanowska, L. Swiderski, and M. Moszynski, "Liquid scintillators and composites in fast neutron detection," *J. Instrum.*, vol. 7, no. 4, pp. C04004–C04004, Apr. 2012.

[17]   W. G. Moulton and C. W. Sherwin, "Fast Neutron Detector," *Rev. Sci. Instrum.*, vol. 20, no. 11, pp. 766–767, Nov. 1949.

[18]   W. F. Hornyak, "A Fast Neutron Detector," *Rev. Sci. Instrum.*, vol. 23, no. 6, pp. 264–267, Jun. 1952.

[19]   A. Buffler and J. Tickner, "Detecting contraband using neutrons: Challenges and future directions," *Radiat. Meas.*, vol. 45, no. 10, pp. 1186–1192, Dec. 2010.

[20]   T. Gozani, "Novel applications of fast neutron interrogation methods," *Nucl. Instruments Methods Phys. Res. Sect. A Accel. Spectrometers, Detect. Assoc. Equip.*, vol. 353, no. 1–3, pp. 635–640, Dec. 1994.

[21]   T. Gozani, "The role of neutron based inspection techniques in the post 9/11/01 era," *Nucl. Instruments Methods Phys. Res. Sect. B Beam Interact. with Mater. Atoms*, vol. 213, pp. 460–463, Jan. 2004.

[22]   T. Gozani and D. Strellis, "Advances in neutron based bulk explosive detection," *Nucl. Instruments Methods Phys. Res. Sect. B Beam Interact. with Mater. Atoms*, vol. 261, no. 1–2, pp. 311–315, Aug. 2007.

[23]   D. Allan Bromley, "Evolution and use of nuclear detectors and systems," *Nucl. Instruments Methods*, vol. 162, no. 1–3, pp. 1–8, Jun. 1979.

[24]   J. Iwanowska *et al.*, "Neutron/gamma discrimination properties of composite scintillation detectors," *J. Instrum.*, vol. 6, no. 7, pp. P07007–P07007, Jul. 2011.

[25]   T. Gozani, "Inspection techniques based on neutron interrogation," in *Physics-Based Technologies for the Detection of Contraband*, 1997, vol. 2936, pp. 9–20.

[26]   T. Gozani, "Neutron-based nonintrusive inspection techniques," in *International Conference Neutrons in Research and Industry*, 1997, vol. 2867, p. 174.

[27]   E. M. A. Hussein and E. J. Waller, "Review of one-side approaches to radiographic imaging for detection of explosives and narcotics," *Radiat. Meas.*, vol. 29, no. 6, pp. 581–591, Dec. 1998.

[28]   A. Buffler, "Contraband detection with fast neutrons," *Radiat. Phys. Chem.*, vol. 71, no. 3–4, pp. 853–861, Oct. 2004.

[29]   T. Gozani, "Detection of Explosives and Other Threats Using Accelerator-Based Neutron Techniques," in *Electrostatic Accelerators*, Ragnar Hellborg, Ed. Berlin, Heidelberg: Springer, 2005, pp. 445–460.

[30]   Z. D. Whetstone and K. J. Kearfott, "A review of conventional explosives detection using active neutron interrogation," *J. Radioanal. Nucl. Chem.*, vol. 301, no. 3, pp. 629–639, Sep. 2014.

[31]   L. Grodzins, "Nuclear techniques for finding chemical explosives in airport luggage," *Nucl. Instruments Methods Phys. Res. Sect. B Beam Interact. with Mater. Atoms*, vol. 56–57, pp. 829–833, May 1991.

[32]   D. Siwal, B. . Wiggins, and R. . DeSouza, "Using pulse shape analysis to improve the position resolution of a resistive anode microchannel plate detector," *Nucl. Instruments Methods Phys. Res. Sect. A Accel. Spectrometers, Detect. Assoc. Equip.*, vol. 804, pp. 144–148, Dec. 2015.

[33]   M. Lampton, "The Microchannel Image Intensifier," *Sci. Am.*, vol. 245, no. 5, pp. 62–71, 1981.

[34]   W. C. Wiley and C. F. Hendee, "Electron Multipliers Utilizing Continuous Strip Surfaces," *IRE Trans. Nucl. Sci.*, vol. 9, no. 3, pp. 103–106, Jun. 1962.

[35]   J. Ladislas Wiza, "Microchannel plate detectors," *Nucl. Instruments Methods*, vol. 162, no. 1–3, pp. 587–601, Jun. 1979.

[36]   O. H. W. Siegmund, A. S. Tremsin, J. V. Vallerga, R. Abiad, and J. Hull, "High resolution cross strip anodes for photon counting detectors," *Nucl. Instruments Methods Phys. Res. Sect. A Accel. Spectrometers, Detect. Assoc. Equip.*, vol. 504, no. 1–3, pp. 177–181, May 2003.

[37]   J. Vallerga, J. McPhate, A. Tremsin, and O. Siegmund, "High-resolution UV, alpha and neutron imaging with the Timepix CMOS readout," *Nucl. Instruments Methods Phys. Res. Sect. A Accel. Spectrometers, Detect. Assoc. Equip.*, vol. 591, no. 1, pp. 151–154, Jun. 2008.

[38]   D. R. Beaulieu *et al.*, "Novel fast neutron counting technology for efficient detection of special nuclear materials," in *2009 IEEE Conference on Technologies for Homeland Security*, 2009, pp. 295–301.

[39]   W. B. Feller, P. L. White, P. B. White, O. H. W. Siegmund, A. P. Martin, and J. V. Vallerga, "Microchannel plate special nuclear materials sensor," *Nucl. Instruments Methods Phys. Res. Sect. A Accel. Spectrometers, Detect. Assoc. Equip.*, vol. 652, no. 1, pp. 25–28, Oct. 2011.

[40]   X. Llopart, R. Ballabriga, M. Campbell, L. Tlustos, and W. Wong, "Timepix, a 65k programmable pixel readout chip for arrival time, energy and/or photon counting measurements," *Nucl. Instruments Methods Phys. Res. Sect. A Accel. Spectrometers, Detect. Assoc. Equip.*, vol. 581, no. 1–2, pp. 485–494, Oct. 2007.

[41]   X. Llopart Cudie, "Design and Characterization of 64K Pixels Chips Working in Single Photon Processing Mode," Mid Sweden U., Sundsvall, 2007.

[42]   O. H. W. Siegmund *et al.*, "Application of atomic layer deposited microchannel plates to imaging photodetectors with high time resolution," *Nucl. Instruments Methods Phys. Res. Sect. A Accel. Spectrometers, Detect. Assoc. Equip.*, vol. 787, pp. 110–113, Jul. 2015.

[43]   J. Vallerga, A. Tremsin, R. Raffanti, and O. Siegmund, "Centroiding algorithms for high speed crossed-strip readout of microchannel plate detectors," *Nucl. Instruments Methods Phys. Res. Sect. A Accel. Spectrometers, Detect. Assoc. Equip.*, vol. 633, pp. S255–S258, May 2011.

[44] Y. Wang, Y. Yang, X. Wang, and Y. Li, "Readout for a large area neutron sensitive microchannel plate detector," *Nucl. Instruments Methods Phys. Res. Sect. A Accel. Spectrometers, Detect. Assoc. Equip.*, vol. 784, pp. 226–231, Jun. 2015.

[45] A. S. Tremsin, J. V. Vallerga, J. B. McPhate, and O. H. W. Siegmund, "Optimization of high count rate event counting detector with Microchannel Plates and quad Timepix readout," *Nucl. Instruments Methods Phys. Res. Sect. A Accel. Spectrometers, Detect. Assoc. Equip.*, vol. 787, pp. 20–25, Jul. 2015.

[46] K. Watanabe, T. Minniti, W. Kockelmann, R. Dalgliesh, G. Burca, and A. S. Tremsin, "Characterization of a neutron sensitive MCP/Timepix detector for quantitative image analysis at a pulsed neutron source," *Nucl. Instruments Methods Phys. Res. Sect. A Accel. Spectrometers, Detect. Assoc. Equip.*, vol. 861, pp. 55–63, Jul. 2017.

[47] G. Vitucci *et al.*, "Energy-resolved neutron tomography of an unconventional cultured pearl at a pulsed spallation source using a microchannel plate camera," *Microchem. J.*, vol. 137, pp. 473–479, Mar. 2018.

[48] G. F. Knoll, *Radiation Detection and Measurement*, 4th ed. Hoboken, N.J: John Wiley & Sons, Inc., 2010.

[49] J. Chariton and C. A. Lea, "Some Experiments concerning the Counting of Scintillations Produced by Alpha Particles. Part I," *Proc. R. Soc. A Math. Phys. Eng. Sci.*, vol. 122, no. 789, pp. 304–319, Jan. 1929.

[50] J. Chariton and C. A. Lea, "Some Experiments concerning the Counting of Scintillations Produced by Alpha Particles. Part II. The Determination of the Efficiency of Transformation of the Kinetic Energy of Formula-Particles into Radiant Energy," *Proc. R. Soc. A Math. Phys. Eng. Sci.*, vol. 122, no. 789, pp. 320–334, Jan. 1929.

[51] J. Chariton and C. A. Lea, "Some Experiments concerning the Counting of Scintillations Produced by Alpha Particles. Part III. Practical Applications," *Proc. R. Soc. A Math. Phys. Eng. Sci.*, vol. 122, no. 789, pp. 335–352, Jan. 1929.

[52] W. R. Leo, *Techniques for nuclear and particle physics experiments : a how-to approach*, 2nd ed. Berlin, Germany: Springer, 1994.

[53] S. V. Budakovsky *et al.*, "New Effective Organic Scintillators for Fast Neutron and Short-Range Radiation Detection," *IEEE Trans. Nucl. Sci.*, vol. 54, no. 6, pp. 2734–2740, Dec. 2007.

[54] J. Hartman, A. Barzilov, E. E. Peters, and S. W. Yates, "Measurements of response functions of EJ-299-33A plastic scintillator for fast neutrons," *Nucl. Instruments Methods Phys. Res. Sect. A Accel. Spectrometers, Detect. Assoc. Equip.*, vol. 804, pp. 137–143, Dec. 2015.

[55] J. Hartman, "Neutron Spectroscopy with Scintillation Detectors using Wavelets," University of Nevada, Las Vegas, 2014.

[56] P. P. Guss, T. G. Stampahar, S. Mukhopadhyay, A. Barzilov, and A. Guckes, "Scintillation properties of a Cs2LiLa(Br6)90%(Cl6)10%:Ce (CLLBC) crystal," in *Radiation Detectors: Systems and Applications XV*, 2014, vol. 9215, p. 921505.

[57] A. L. Guckes, "Novel Deployment of Elpasolites as a Dual Neutron / Gamma-ray Directional Detector," University of Nevada, Las Vegas, 2014.

[58] E. V. van Loef, J. Glodo, U. Shirwadkar, N. Zaitseva, and K. S. Shah, "Solution growth and scintillation properties of novel organic neutron detectors," *Nucl. Instruments Methods Phys. Res. Sect. A Accel. Spectrometers, Detect. Assoc. Equip.*, vol. 652, no. 1, pp. 424–426, Oct. 2011.

[59] P. A. Rodnyi, *Physical processes in inorganic scintillators*. CRC Press, 1997.

[60] S. E. Derenzo, W. W. Moses, J. L. Cahoon, T. A. DeVol, and L. Boatner, "X-ray fluorescence measurements of 412 inorganic compounds," in *Conference Record of the 1991 IEEE Nuclear Science Symposium and Medical Imaging Conference*, 1992, pp. 143–147.

[61] F. P. Doty, X. Zhou, P. Yang, and M. A. Rodriguez, "Elpasolite Scintillators," Livermore, CA, 2012.

[62] K. E. Mesick, D. D. S. Coupland, and L. C. Stonehill, "Pulse-shape discrimination and energy quenching of alpha particles in Cs2LiLaBr6:Ce3+," *Nucl. Instruments Methods Phys. Res. Sect. A Accel. Spectrometers, Detect. Assoc. Equip.*, vol. 841, pp. 139–143, Jan. 2017.

[63] C. M. Whitney *et al.*, "Gamma–neutron imaging system utilizing pulse shape discrimination with CLYC," *Nucl. Instruments Methods Phys. Res. Sect. A Accel. Spectrometers, Detect. Assoc. Equip.*, vol. 784, pp. 346–351, Jun. 2015.

[64] O. Tarasenko, N. Galunov, N. Karavaeva, I. Lazarev, and V. Panikarskaya, "Stilbene composite scintillators as detectors of fast neutrons emitted by a 252Cf source," *Radiat. Meas.*, vol. 58, pp. 61–65, Nov. 2013.

[65] N. P. Zaitseva *et al.*, "Recent developments in plastic scintillators with pulse shape discrimination," *Nucl. Instruments Methods Phys. Res. Sect. A Accel. Spectrometers, Detect. Assoc. Equip.*, vol. 889, pp. 97–104, May 2018.

[66] L. Carman *et al.*, "The effect of material purity on the optical and scintillation properties of solution-grown trans-stilbene crystals," *J. Cryst. Growth*, vol. 368, pp. 56–61, Apr. 2013.

[67] Y. S. Sulyaev *et al.*, "Multi-purpose fast neutron spectrum analyzer with real-time signal processing," *Nucl. Instruments Methods Phys. Res. Sect. A Accel. Spectrometers, Detect. Assoc. Equip.*, vol. 720, pp. 23–25, Aug. 2013.

[68] Ö. Skeppstedt *et al.*, "The EUROBALL neutron wall – design and performance tests of neutron detectors," *Nucl. Instruments Methods Phys. Res. Sect. A Accel. Spectrometers, Detect. Assoc. Equip.*, vol. 421, no. 3, pp. 531–541, Feb. 1999.

[69] J. Ljungvall, M. Palacz, and J. Nyberg, "Monte Carlo simulations of the Neutron Wall detector system," *Nucl. Instruments Methods Phys. Res. Sect. A Accel. Spectrometers, Detect. Assoc. Equip.*, vol. 528, no. 3, pp. 741–762, Aug. 2004.

[70] D. C. Stromswold *et al.*, "Comparison of plastic and NaI(Tl) scintillators for vehicle portal monitor applications," in *2003 IEEE Nuclear Science Symposium. Conference Record (IEEE Cat. No.03CH37515)*, 2003, p. 1065–1069 Vol.2.

[71] G. H. V. Bertrand, M. Hamel, S. Normand, and F. Sguerra, "Pulse shape discrimination between (fast or thermal) neutrons and gamma rays with plastic scintillators: State of the art," *Nucl. Instruments Methods Phys. Res. Sect. A Accel. Spectrometers, Detect. Assoc. Equip.*, vol. 776, pp. 114–128, Mar. 2015.

[72] G. H. V. Bertrand, M. Hamel, and F. Sguerra, "Current Status on Plastic Scintillators Modifications," *Chem. - A Eur. J.*, vol. 20, no. 48, pp. 15660–15685, Nov. 2014.

[73] N. Zaitseva *et al.*, "Plastic scintillators with efficient neutron/gamma pulse shape discrimination," *Nucl. Instruments Methods Phys. Res. Sect. A Accel. Spectrometers, Detect. Assoc. Equip.*, vol. 668, pp. 88–93, Mar. 2012.

[74] S. Nyibule *et al.*, "Radioluminescent characteristics of the EJ 299-33 plastic scintillator," *Nucl. Instruments Methods Phys. Res. Sect. A Accel. Spectrometers, Detect. Assoc. Equip.*, vol. 728, pp. 36–39, Nov. 2013.

[75] V. Nagarkar, I. Sheshtakova, and L. Ovechkina, "Neutron detectors and related methods," US7372041B1, 17-Jan-2007.

[76] I. Shestakova, E. Ovechkina, V. Gaysinskiy, J. J. Antal, L. Bobek, and V. Nagarkar, "A High Spatial Resolution Sensor For Thermal Neutron Imaging," *IEEE Trans. Nucl. Sci.*, vol. 54, no. 5, pp. 1797–1800, Oct. 2007.

[77] K. J. Riley, L. Ovechkina, S. Palamakumbura, Z. Bell, S. Miller, and V. V Nagarkar, "A structured organic scintillator for neutron imaging," in *IEEE Nuclear Science Symposuim & Medical Imaging Conference*, 2010, pp. 1777–1780.

[78] N. Z. Galunov, "New generation of high effective organic scintillators and their process technology," in *Transactions of International Technology Transfer Conference*, 1998, p. 124.

[79] S. V. Budakovsky *et al.*, "Stilbene crystalline powder in polymer base as a new fast neutron detector," *Radiat. Meas.*, vol. 42, no. 4–5, pp. 565–568, Apr. 2007.

[80] A. V. Krech and N. Z. Galunov, "Composite Scintillators and Some Features of Their Radiation Resistance," *Ukr. J. Phys.*, vol. 62, no. 7, pp. 569–582, Aug. 2017.

[81] N. Z. Galunov *et al.*, "Development of New Composite Scintillation Materials Based on Organic Crystalline Grains," *IEEE Trans. Nucl. Sci.*, vol. 56, no. 3, pp. 904–910, Jun. 2009.

[82] N. L. Karavaeva and O. A. Tarasenko, "Large Size Composite Scintillators," *Funct. Mater.*, vol. 17, no. 3, pp. 379–385, 2010.

[83] N. L. Karavaeva, N. Z. Galunov, E. V. Martynenko, and A. V. Kosinova, "Combined Composite Scintillation Detector for Separate Measurements of Fast and Thermal Neutrons," *Funct. Mater.*, vol. 17, no. 4, pp. 549–553, 2010.

[84] S. K. Lee *et al.*, "Development of large-area composite stilbene scintillator for fast neutron detection," *J. Nucl. Sci. Technol.*, vol. 51, no. 1, pp. 37–47, Jan. 2014.

[85] N. Z. Galunov *et al.*, "Peculiarities of radiation resistance of organic scintillators," in *Abstracts of the 13th Conference on High Energy Physics, Nuclear Physics and Accelerators*, 2015, p. 99.

[86] S. V. Budakovsky, N. Z. Galunov, B. V. Grinyov, J. K. Kim, Y. K. Kim, and O. A. Tarasenko, "New generation of Organic Scintillation Materials," *Funct. Mater.*, vol. 16, no. 1, pp. 86–91, 2009.

[87] N. Z. Galunov, B. V. Grinyov, N. L. Karavaeva, Y. V. Gerasymov, O. T. Sidletskiy, and O. A. Tarasenko, "Gd-Bearing Composite Scintillators as the New Thermal Neutron Detectors," *IEEE Trans. Nucl. Sci.*, vol. 58, no. 1, pp. 339–346, Feb. 2011.

[88] D. H. Wilkinson, "The Phoswich—A Multiple Phosphor," *Rev. Sci. Instrum.*, vol. 23, no. 8, pp. 414–417, Aug. 1952.

[89] S. R. Moghadam, S. A. H. Feghhi, and M. J. Safari, "A phoswich detector for simultaneous alpha–gamma spectroscopy," *Nucl. Instruments Methods Phys. Res. Sect. A Accel. Spectrometers, Detect. Assoc. Equip.*, vol. 799, pp. 59–63, Nov. 2015.

[90] Y. H. Chung, Y. Choi, G. Cho, Y. S. Choe, K.-H. Lee, and B.-T. Kim, "Characterization of dual layer phoswich detector performance for small animal PET using Monte Carlo simulation," *Phys. Med. Biol.*, vol. 49, no. 13, pp. 2881–2890, Jul. 2004.

[91] R. de la Fuente *et al.*, "Low level radioactivity measurements with phoswich detectors using coincident techniques and digital pulse processing analysis," *J. Environ. Radioact.*, vol. 99, no. 10, pp. 1553–1557, Oct. 2008.

[92] L. Eriksson, C. L. Melcher, M. Eriksson, H. Rothfuss, R. Grazioso, and M. Aykac, "Design Considerations of Phoswich Detectors for High Resolution Positron Emission Tomography," *IEEE Trans. Nucl. Sci.*, vol. 56, no. 1, pp. 182–188, Feb. 2009.

[93] F. Amorini *et al.*, "On-Beam Digital Pulse Shape Acquisition From NE102A-BaF2 Phoswich Detector," *IEEE Trans. Nucl. Sci.*, vol. 56, no. 4, pp. 2519–2523, Aug. 2009.

[94] T. L. White and W. H. Miller, "A triple-crystal phoswich detector with digital pulse shape discrimination for alpha/beta/gamma spectroscopy," *Nucl. Instruments Methods Phys. Res. Sect. A Accel. Spectrometers, Detect. Assoc. Equip.*, vol. 422, no. 1–3, pp. 144–147, Feb. 1999.

[95] J. Seidel, J. J. Vaquero, S. Siegel, W. R. Gandler, and M. V. Green, "Depth identification accuracy of a three layer phoswich PET detector module," *IEEE Trans. Nucl. Sci.*, vol. 46, no. 3, pp. 485–490, Jun. 1999.

[96] N. L. Childress and W. H. Miller, "MCNP analysis and optimization of a triple crystal phoswich detector," *Nucl. Instruments Methods Phys. Res. Sect. A Accel. Spectrometers, Detect. Assoc. Equip.*, vol. 490, no. 1–2, pp. 263–270, Sep. 2002.

[97] W. H. Miller and M. Diaz de Leon, "Utilization of phoswich detectors for simultaneous, multiple radiation detection," *J. Radioanal. Nucl. Chem.*, vol. 264, no. 1, pp. 163–167, Mar. 2005.

[98] A. T. Farsoni and D. M. Hamby, "MCNP analysis of a multilayer phoswich detector for β-particle dosimetry and spectroscopy," *Nucl. Instruments Methods Phys. Res. Sect. A Accel. Spectrometers, Detect. Assoc. Equip.*, vol. 555, no. 1–2, pp. 225–230, Dec. 2005.

[99] A. T. Farsoni and D. M. Hamby, "Study Of A Triple-Layer Phoswich Detector For Beta And Gamma Spectroscopy With Minimal Crosstalk," in *28th Seismic Research Review: Ground-Based Nuclear Explosion Monitoring Technologies*, 2006, pp. 784–792.

[100] S. Yamamoto and H. Ishibashi, "Development of a three-layer phoswich alpha–beta–gamma imaging detector," *Nucl. Instruments Methods Phys. Res. Sect. A Accel. Spectrometers, Detect. Assoc. Equip.*, vol. 785, pp. 129–134, Jun. 2015.

[101] W. Hennig, H. Tan, W. K. Warburton, and J. I. McIntyre, "Digital Pulse Shape Analysis With Phoswich Detectors To Simplify Coincidence Measurements Of Radioactive Xenon," in *27th Seismic Research Review: Ground-Based Nuclear Explosion Monitoring Technologies*, 2005, pp. 787–794.

[102] W. Hennig, H. Tan, A. Fallu-Labruyere, W. K. Warburton, J. I. McIntyre, and A. Gleyzer, "Design Of A Phoswich Well Detector For Radioxenon Monitoring," in *28th Seismic Research Review: Ground-Based Nuclear Explosion Monitoring Technologies*, 2006, pp. 801–810.

[103] W. Hennig *et al.*, "Evaluation of phoswich well detectors for radioxenon monitoring," in *2007 IEEE Nuclear Science Symposium Conference Record*, 2007, pp. 756–760.

[104] W. Hennig *et al.*, "Development Of A Cots Radioxenon Detector System Using Phoswich Detectors And Pulse Shape Analysis," in *30th Monitoring Research Review: Ground-Based Nuclear Explosion Monitoring*, 2008, pp. 758–767.

[105] W. Hennig *et al.*, "Development of a phoswich detector system for radioxenon monitoring," *J. Radioanal. Nucl. Chem.*, vol. 282, no. 3, pp. 681–685, Dec. 2009.

[106] A. T. Farsoni, B. Alemayehu, A. Alhawsawi, and E. M. Becker, "A Phoswich Detector With Compton Suppression Capability for Radioxenon Measurements," *IEEE Trans. Nucl. Sci.*, vol. 60, no. 1, pp. 456–464, Feb. 2013.

[107] W. Hennig, S. J. Asztalos, W. K. Warburton, A. Fallu-Labruyere, A. Samie, and P. Mekarski, "Development of a Phoswich Detector for Radioxenon Field Measurements," *IEEE Trans. Nucl. Sci.*, vol. 61, no. 5, pp. 2778–2785, Oct. 2014.

[108] B. Alemayehu, A. T. Farsoni, L. Ranjbar, and E. M. Becker, "A well-type phoswich detector for nuclear explosion monitoring," *J. Radioanal. Nucl. Chem.*, vol. 301, no. 2, pp. 323–332, Aug. 2014.

[109] M. Takada *et al.*, "Characteristics of a phoswich detector to measure the neutron spectrum in a mixed field of neutrons and charged particles," *Nucl. Instruments Methods Phys. Res. Sect. A Accel. Spectrometers, Detect. Assoc. Equip.*, vol. 476, no. 1–2, pp. 332–336, Jan. 2002.

[110] M. Takada and T. Nakamura, "A phoswich detector for high-energy neutrons," *Radiat. Prot. Dosimetry*, vol. 126, no. 1–4, pp. 178–184, May 2007.

[111] M. Takada, K. Yajima, H. Yasuda, T. Sato, and T. Nakamura, "Neutron, photon and proton energy spectra at high altitude measured using a phoswich-type neutron detector," *Radiat. Meas.*, vol. 45, no. 10, pp. 1297–1300, Dec. 2010.

[112] M. TAKADA *et al.*, "Response Functions of Phoswich-Type Neutron Detector for High-Energy Cosmic Ray Neutron Measurement," *J. Nucl. Sci. Technol.*, vol. 47, no. 10, pp. 917–931, Oct. 2010.

[113] T. Watanabe *et al.*, "Performance of a phoswich detector composed of an inner NaI(Tl) crystal and surrounding NE102A plastic scintillator for neutron spectrometry," *Nucl. Instruments Methods Phys. Res. Sect. A Accel. Spectrometers, Detect. Assoc. Equip.*, vol. 587, no. 1, pp. 20–28, Mar. 2008.

[114] J. Hartman and A. Barzilov, "Study of pulse shape discrimination for a neutron phoswich detector," *EPJ Web Conf.*, vol. 153, p. 7012, Sep. 2017.

[115] G. D. Badhwar *et al.*, "A study of the radiation environment on board the Space Shuttle flight STS-57," *Radiat. Meas.*, vol. 24, no. 3, pp. 283–289, Jul. 1995.

[116] G. D. Badhwar *et al.*, "In-flight radiation measurements on STS-60," *Radiat. Meas.*, vol. 26, no. 1, pp. 17–34, Jan. 1996.

[117] H. Matsumoto *et al.*, "Real-time measurement of low-energy-range neutron spectra on board the space shuttle STS-89 (S/MM-8)," *Radiat. Meas.*, vol. 33, no. 3, pp. 321–333, Jun. 2001.

[118] A. R. Green *et al.*, "Bubble detector characterization for space radiation," *Acta Astronaut.*, vol. 56, no. 9–12, pp. 949–960, May 2005.

[119] M. B. Smith *et al.*, "Canadian High-Energy Neutron Spectrometry System (CHENSS)," in *Proceedings of International Workshop on Fast Neutron Detectors and Applications*, 2007, vol. 25, p. 6.

[120] H. Klein and F. D. Brooks, "SCINTILLATION DETECTORS FOR FAST NEUTRONS," in *Proceedings of International Workshop on Fast Neutron Detectors and Applications — PoS(FNDA2006)*, 2007, vol. 25.

[121] F. Vanhavere and F. d'Errico, "Standardisation of Superheated Drop and Bubble Detectors," *Radiat. Prot. Dosimetry*, vol. 101, no. 1, pp. 283–287, Aug. 2002.

[122] G. Jonkmans *et al.*, "A Canadian high-energy neutron spectrometry system for measurements in space," *Acta Astronaut.*, vol. 56, no. 9–12, pp. 975–979, May 2005.

[123] G. T. Wright, "Scintillation Decay Times of Organic Crystals," *Proc. Phys. Soc. Sect. B*, vol. 69, no. 3, pp. 358–372, Mar. 1956.

[124] F. D. Brooks, "Scintillation counters with pulse shape selection to distinguish neutrons from gamma-rays," in *Liquid Scintillation Counting Proceedings*, 1958, pp. 268–269.

[125] F. D. Brooks, "A scintillation counter with neutron and gamma-ray discriminators," *Nucl. Instruments Methods*, vol. 4, no. 3, pp. 151–163, Apr. 1959.

[126] P. Lecoq, A. Gektin, and M. Korzhik, "Scintillation Mechanisms in Inorganic Scintillators," in *Inorganic Scintillators for Detector Systems*, 2nd ed., Springer International Publishing, 2017, pp. 125–174.

[127] T. Goorley *et al.*, "Initial MCNP6 Release Overview," *Nucl. Technol.*, vol. 180, no. 3, pp. 298–315, Dec. 2012.

[128] T. Goorley, "MCNP6.1.1-Beta Release Notes," LA-UR-14-24680, 2014.

[129] M. Licata and M. J. Joyce, "Concealed nuclear material identification via combined fast-neutron/γ-ray computed tomography (FNGCT): a Monte Carlo study," *J. Instrum.*, vol. 13, no. 2, pp. P02013–P02013, Feb. 2018.

[130] J. Hartman, A. P. Yazdanpanah, A. Barzilov, and E. Regentova, "3D imaging using combined neutron-photon fan-beam tomography: A Monte Carlo study," *Appl. Radiat. Isot.*, vol. 111, 2016.

[131] A. Pour Yazdanpanah, J. Hartman, E. Regentova, and A. Barzilov, "Sparse-view neutron-photon computed tomography: Object reconstruction and material discrimination," *Appl. Radiat. Isot.*, vol. 132, pp. 122–128, Nov. 2018.

[132] J. Hartman and A. Barzilov, "Combined photon − neutron radiography for nondestructive analysis of materials," *J. Radioanal. Nucl. Chem.*, vol. 307, no. 3, pp. 2307–2312, 2016.

[133] J. Wang *et al.*, "Neutron cross-talk in a multi-detector system," *Nucl. Instruments Methods Phys. Res. Sect. A Accel. Spectrometers, Detect. Assoc. Equip.*, vol. 397, no. 2–3, pp. 380–390, Oct. 1997.

CURRICULUM VITAE

Jessica Hartman
Jessica.Hartman@unlv.edu
https://www.linkedin.com/in/jessica-hartman-35a2273a/

Education
Ph.D. Mechanical Engineering, 2018
University of Nevada, Las Vegas
    Dissertation Title: Detector Arrays for Nuclear Security and Safeguards Applications

Master of Science, Materials and Nuclear Engineering, 2014
University of Nevada, Las Vegas
    Thesis Title: Neutron Spectroscopy with Scintillation Detectors Using Wavelets

Bachelor of Science, Mechanical Engineering, 2012
University of Nevada, Las Vegas

Graduate Certificates at UNLV
- Nuclear Criticality Safety, 2014
- Graduate Certificate, Nuclear Safeguards and Security, 2014

Honors and Awards

NNSA Graduate Fellowship Recipient	June 2018 – June 2019
National Securities Technologies Scholarship	Spring 2017
Nuclear Regulatory Commission Fellowship	Spring 2016 – Current
2nd Place - UNLV Engineering Department Best Thesis Competition	Spring 2015
Helen & Roy Kelsall Engineering Scholarship	Fall 2015 – Spring 2016
STEM Fellowship	Fall 2013 – Spring 2015
American Nuclear Society Nevada Chapter Scholarship	Fall 2012
Provisional Patent #62/279214 – Phoswich Detector With Fast Neutron Spectroscopy Function	January 2015
Graduate Research Certification from UNLV's Graduate College	Spring 2016

Extracurricular Activities
Volunteer Coordinator for College of Engineering Career Fair
Student Program Co-Chair for 2016 ANS Winter Meeting and Nuclear Technology Expo
American Nuclear Society, University of Nevada, Las Vegas Student Chapter

President	April 2017 – April 2018
Vice President	April 2016 – April 2017
Secretary	April 2014 – April 2016

Professional Memberships and Societies
American Nuclear Society (2012-Present)
American Society of Nondestructive Testing (2014-2017)
Institute of Electrical and Electronics Engineers (2015-2017)

Peer-Reviewed Publications & Conference Proceedings

2018

A. Pour Yazdanpanah, **J. Hartman,** E. Regentova, A. Barzilov, "Sparse-view neutron-photon computed tomography: Object reconstruction and material discrimination," *Applied Radiation and Isotopes*, vol. 132, Feb., pp. 122-128, 2018. [DOI: 10.1016/j.apradiso.2017.11.029]

J. Hartman, A. Barzilov, "Fast Neutron Imaging Using A Scintillator Detector Array," Presented at 11th International Conference on Methods and Applications of Radioanalytical Chemistry, Kailua-Kona, Hawaii, 2018.

2017

J. Hartman, A. Barzilov, "Study of pulse shape discrimination for a neutron phoswich detector," In EPJ Web of Conferences, 2017, vol. 153. [DOI: 10.1051/epjconf/201715307012]

2016

J. Hartman, A. Pour Yazdanpanah, A. Barzilov, E. Regentova, "3D imaging using combined neutron-photon fan-beam tomography: A Monte Carlo Study," *Applied Radiation and Isotopes*, vol. 111, May, pp. 110-116, 2016. [DOI: 10.1016/j.apradiso.2016.02.018]

J. Hartman, A. Barzilov, "Evaluation of photon, thermal neutron, and fast neutron discrimination for a neutron phoswich detector," Presented at ANS 2016 Student Conference, Madison, Wisconsin, 2016.

J. Hartman, A. Barzilov, "Engineering Design of Neutron Detection System," In Proceedings of the Arizona-Nevada Academy of Science, 2016, vol. 51, pp. 24.

J. Hartman, A. Barzilov, "Development of a Phoswich Neutron Detector with Energy Spectroscopy Capability," In Transactions of the American Nuclear Society, 2016, vol. 114.

J. Lee, **J. Hartman**, Z. Cook, J. S. Lee, W. Yim, A. Barzilov, "Development of Plug-and-Play Interchangeable Components for Unmanned Aerial System with Mobile Manipulation Capability," In Transactions of the American Nuclear Society, 2016, vol. 115.

Z.Cook, J.Lee, **J.Hartman**, A.Barzilov, W. Yim, "Contour Mapping Based Radiation Source Localization by UAS Swarm," In Transactions of the American Nuclear Society, 2016, vol. 115.

2015

J. Hartman, A. Barzilov, E.E. Peters, S.W. Yates, "Measurements of response functions of EJ-299-33A plastic scintillator for fast neutrons," *Nuclear Instruments and Methods in Physics Research Section A: Accelerators, Spectrometers, Detectors and Associated Equipment*, vol. 804, Dec., pp. 137-143, 2015. [DOI: 10.1016/j.nima.2015.09.068]

J. Hartman, A. Barzilov, "Combined photon-neutron radiography for nondestructive analysis of materials," *Journal of Radioanalytical and Nuclear Chemistry*, vol. 307, no. 3, March, pp. 2307-2312, 2016. [DOI: 10.1007/s10967-015-4564-9]

J. Hartman, A. Barzilov, "Neutron Spectrum Measurements Using The EJ-299-33A Plastic Scintillation Detector," In 56th Annual Meeting of the Institute of Nuclear Materials Management, 2015, vol. 2, pp. 1543.

J. Hartman, A. Barzilov, "DD and DT Neutron Generator Yield Measurements Using EJ-299-33A Detector," In 2015 IEEE Nuclear Science Symposium & Medical Imaging Conference, 2015.

J. Hartman, A. Barzilov, I. Novikov, "Remote Sensing of Neutron and Gamma Radiation Using Aerial Unmanned Autonomous System," In 2015 IEEE Nuclear Science Symposium & Medical Imaging Conference, 2015.

J. Hartman, A. Pour Yazdanpanah, A. Barzilov, E. Regentova, "Neutron-Photon Computed Tomography of Cargo Containers in a Cone Beam Configuration," Presented at 12th International Topical Meeting on Nuclear Applications of Accelerators, Washington, D.C., 2015.

2014

J. Hartman, N. Richardson, A. Barzilov, "Dual Neutron Photon Radiography Using a Single Imaging Detector Array," In ASNT 23rd Research Symposium, 2014, pg. 43.

J. Hartman, A. Barzilov, "Evaluation of Performance of Neutron Spectrum Unfolding Technique Based on Wavelets," Presented at ANS 2014 Student Conference, University Park, Pennsylvania, 2014.

J. Hartman, A. Barzilov, "Application of Wavelet Unfolding Technique in Neutron Spectroscopic Analysis," In *Physics Procedia, 23rd International Conference on the Application of Accelerators in Research and Industry*, 2015, vol. 66, pp 410-415. [DOI: 10.1016/j.phpro.2015.05.051]

J. Hartman, A. Barzilov, "Computational Study of Integrated Neutron/Photon Imaging for Illicit Material Detection," In *Physics Procedia, 23rd International Conference on the Application of Accelerators in Research and Industry*, 2015, vol. 66, pp 85-94. [DOI: 10.1016/j.phpro.2015.05.013]

A. Barzilov, **J. Hartman**, N. Richardson, "Measurements of Fast Neutron Flux Using an Array of EJ-299-33A Scintillator Detectors," In Transactions of the American Nuclear Society, 2014, vol. 110.

Non-Peer-Reviewed Publications & Conference Proceedings

2017

J. Hartman, A. Barzilov, "Computational Study of Photon/Neutron Radiography," Presented at 7th Annual Graduate Celebration, Las Vegas, Nevada, 2017.

2016

J. Hartman, A. Barzilov, A. Novikov, "Remote Sensing of Neutron and Gamma Radiation Using Aerial Unmanned Autonomous System," Presented at 18th Annual Graduate & Professional Student Research Forum, Las Vegas, Nevada, 2016.

J. Hartman, A. Barzilov, "Engineering Design of Neutron Detection System," Presented at 6th Annual Graduate Celebration, Las Vegas, Nevada, 2016.

2015

J. Hartman, A. Barzilov, "Neutron Spectroscopy with Scintillation Detectors Using Wavelets," Presented at 17th Annual Graduate & Professional Student Research Forum, Las Vegas, Nevada, 2015.

J. Hartman, A. Barzilov, "Computational Study of Dual Photon/Neutron Techniques for Imaging Applications," Presented at 5th Annual Graduate Celebration, Las Vegas, Nevada, 2015.

2014

J. Hartman, A. Barzilov, "Evaluation of Performance of Neutron Spectrum Unfolding Technique Based on Wavelets," Presented at 16th Annual Graduate & Professional Student Research Forum, Las Vegas, Nevada, 2014.

J. Hartman, A. Barzilov, "Computational Feasibility Study of Dual Photon/Neutron Imaging Technique," Presented at 4th Annual Graduate Celebration, Las Vegas, Nevada, 2014.